

Accurate structure of aluminum and molybdenum  
using synchrotron powder X-ray diffraction

Tomoaki Sasaki

February 2019

Accurate structure of aluminum and molybdenum  
using synchrotron powder X-ray diffraction

Tomoaki Sasaki

Doctoral Program in Physics

Submitted to the Graduate School of  
Pure and Applied Sciences  
in Partial Fulfillment of the Requirements  
for the Degree of Doctor of Philosophy in Science  
at University of Tsukuba

# Table of contents

Chapter 1	Introduction.....	1
Chapter 2	Difficulties in observation of electron distribution of metals.....	5
2.1	Purpose and contents of this chapter.....	5
2.2	Relationship between structure factors and electron density distribution.....	5
2.3	Small electron density value of chemical bonding in metals.....	7
2.4	Low Debye temperature .....	9
2.5	Strain and defect .....	12
2.6	Aluminum and molybdenum.....	13
Chapter 3	Measurement of synchrotron powder X-ray diffraction .....	16
3.1	Introduction.....	16
3.2	Experimental .....	17
3.2.1	Glovebox.....	18
3.2.2	Large Debye-Scherrer camera.....	18
3.2.3	Imaging Plate reader .....	19
3.3	Preparation of measurement sample.....	22
3.4	Synchrotron powder X-ray diffraction experiment of aluminum and molybdenum.....	22
3.4.1	Reduction of fluorescence X-ray from molybdenum .....	23
3.4.2	Experimental conditions of aluminum and molybdenum .....	26
3.5	Diffraction data .....	26
3.5.1	2-dimensional diffraction data of aluminum and molybdenum .....	26
3.5.2	Integration of 2-dimensional diffraction data to 1-dimensional diffraction data.....	29
3.5.3	1-dimensional diffraction data of aluminum and molybdenum .....	31
3.6	Summary .....	42
Chapter 4	Principles and Analysis .....	43
4.1	Introduction.....	43
4.2	Principle of Rietveld refinement.....	43
4.3	Principle of multipole refinement.....	45
4.5	Analysis of anharmonic thermal vibration.....	48
4.5	Analysis of thermal diffuse scattering.....	49
4.6	Density functional theory.....	56
4.7	Sets of structure factors .....	57
Chapter 5	Charge density and thermal motion of aluminum .....	59
5.1	Introduction.....	59
5.2	Flow of data analysis.....	59
5.3	Data analysis by Rietveld refinement .....	60
5.4	Theoretical calculation of charge density.....	61
5.5	Multipole modeling of theoretical structure factors.....	61

5.6	The estimation of first-order thermal diffuse scattering in diffraction data.....	65
5.7	The estimation of anharmonic thermal vibration.....	68
5.8	Extraction of experimental structure factors with multipole model.....	68
5.9	Comparison of structure factor sets: Experimental, theoretical, reported sets .....	72
5.10	Static deformation densities .....	74
5.11	Discussion.....	75
5.12	Summary .....	77
Chapter 6	Charge density of molybdenum .....	78
6.1	Introduction.....	78
6.2	Overview of Experiment.....	79
6.3	Data analysis by Rietveld refinement .....	80
6.4	Extraction of experimental structure factors with multipole model.....	80
6.5	Theoretical structure factors .....	80
6.6	Comparison of structure factor sets .....	81
6.7	Comparison of valence charge density .....	82
6.8	Comparison of static deformation densities .....	83
6.9	Results of $d$ -orbital population analysis.....	83
6.10	Bond characterization by topological analysis of charge density.....	84
6.11	Summary .....	84
Chapter 7	Conclusion .....	85
References.....		87
Acknowledgements .....		92

# Chapter 1 Introduction

Metal is one of the most important materials for human civilization. Here, ‘metal’ includes both pure metals from single elements and alloys comprising of multi-elements. Pure copper and iron have been used as materials for human tools for over 5000 years, pure copper is still used for electrical wiring. The Japanese 1-yen coin is made of pure aluminum. Aluminum alloys are widely used in window sashes, beverage cans, bicycles, cars, and airplane parts. Pure nickel is used as plating owing to its high corrosion resistance and conductivity. Pure molybdenum has a high melting point and good workability. Iron alloys containing molybdenum are used for vehicles frames and kitchen knives, among others, owing to their corrosion resistance, high strength, and hardness.

The enhancement of the function of metal is an important contribution to the change of human civilization. The difference in hardness between natural pure copper and bronze produced the Bronze Age. The lightness and strength of aluminum alloys have contributed to the increase in airplanes and improvement of the fuel efficiency of cars. The enhancement of the strength and corrosion resistance of iron has promoted its use in daily human life. This includes, for example, cooking using knives and pans, building using steel bars and reinforcing bars, and manufacturing of heat engines. The annual production of crude steel around the world has reached 1.6 billion tons.

The efficient enhancement of the functions of metals requires explanation and prediction of the properties of metals based on quantum mechanics. The explanation and prediction form the electron theory of metals. Historically important works were carried out by P. K. L. Drude and H. A. Lorentz in the 19th century [1]. An electron theory of metals has been established by N. F. Mott and H. Jones, etc. at around 1930 soon after an establishment of quantum mechanics. Pure metals and simple alloys were the central topics in the first stage of quantum condensed matter physics. The periodic table contains 113 elements, more than 70% of which are solid pure metal under normal temperature and pressure. These metals form binary, ternary, quaternary and other alloys. The properties of alloys and pure metals are different. Even alloys made of the same element have different properties owing to their compositions. Investigation of the properties of metals by the brute force method requires an enormous number of samples and measurements. This survey cannot be achieved in terms of time and money. Explaining and predicting of the properties of metals using the electron theory of metals provide the guidelines for the material design and experiment using theoretical calculation. This guidance considerably saves time and money.

The electron theory of metals explains and predicts a large part of the electrical, thermal and magnetic properties of metals from quantum mechanics but does not explain the mechanical properties of metals. For example, the high electrical and thermal conductivities in metals are explained by the long mean free path of conduction electrons. The long mean free path is explained by Lindhard's equation of dielectric constant within the nearly free electron model. The nearly free electron model and the tight binding model are two kinds of extremely simple approximation for solids in theoretical study. The nearly free electron model is appropriate for pure metal systems such as aluminum and copper. The tight binding model is appropriate for covalent bonding materials such as silicon. An extraordinary amount of research including the electrical properties and structure have been carried

out during the past 100 years based on quantum mechanics. However, the elastic constants of metals are explained by a classical mechanical model in which atoms are connected by springs.

Metallic properties are governed by the accurate structure of metals. Accurate structures are the spatial distribution of nuclei and electrons in metals and their changes due to thermal vibration of the nuclei. Accurate structures determine the nature of defect-free metals. At present, the mechanical properties of metals are studied by lattice defects. Lattice defects correct the properties of defect-free metals. The mechanical properties of the actual metal consist of: (1) the properties of the defect-free metal and (2) the modification of the properties of the metal by lattice defects. Understanding the actual properties of metal based on quantum mechanics requires elucidations of the accurate structure of metal.

Since 2002, the relationship between the mechanical properties of metals and the spatial distribution of electrons, that is, the electron density distribution in metals, has been reported. Ogata et al. [2] reported a relationship between the ideal shear strength and electron density distribution in aluminum and copper. Eberhart et al. [3] reported an agreement between the elastic constants from the electron density and experimental values of the Cauchy pressure in the body-centered cubic (bcc) monovalent metals molybdenum, niobium, tantalum, vanadium, and tungsten. A relationship between the brittleness and the electron density of the CrAl, MnAl, FeAl, CoAl, and NiAl alloys was also reported [4].

With the development of computers, theoretical uses of electron density distribution have developed remarkably. The relationship with the mechanical properties and the electron density distribution of metals researched by Eberhart is a representative example. The electron density distribution is also used in quantum crystallography. Quantum crystallography is a field which leads more accurate crystallographic experiments and calculation results by using mutual utilization of experimental observation and theoretical calculation. This includes improvements of approximated theoretical wave function with incomplete consideration of electronic correlation by a limitation from experimental results and improvements of experimental models by quantum mechanics. The former uses the density matrix representation of the electron density distribution. The latter realizes an accurate observation of electron density distribution by a more precise model based on quantum mechanics. Eberhart's method is applied only to the theoretical electron density distribution. Mutual complement of experiment and theory in quantum crystallography depends on the accuracy of experimental electron density distribution. The provision of accurate experimental electron density distribution is synonymous with the development of these fields.

Only one report has been reported so far for experimental observation of the accurate electron density distribution of metal. Since the electron redistribution in pure metal is smaller than ionic crystal and covalent crystal, experimental electron density distribution other than the report could not observe the electron redistribution. Here, the electron redistribution is a deviation of the electron density distribution from the superposition of spherical electron density distribution of isolated atoms. This occurs as a result of periodic arrangement of atoms. The redistribution is called chemical bonding. Generally, the electron density value of chemical bonding in metals is smaller than that of covalent crystals. The electron density at the midpoint of chemical bonding between the nearest atoms in

diamond is  $\sim 1.0 \text{ e}/\text{\AA}^3$  [5]. When the valence electrons of trivalent aluminum are uniformly distributed in the crystal, the electron density value is  $0.18 \text{ e}/\text{\AA}^3$ . Detection of this difference from the uniform distribution requires an accuracy of  $\sim 0.01 \text{ e}/\text{\AA}^3$  of the electron density. Metal is easily oxidized. Softness of metal leads to internal strain and defects. The low Debye temperature of metal makes it difficult to accurately observe structure factors. Owing to these difficulties, accurate electron density distributions of metals have not been observed until recently. In 2011, Nakashima et al. [6] successfully measured the lowest two accurate structure factors of aluminum by quantitative convergent-beam electron diffraction (QCBED). From the two structure factors, the electron density value  $0.05 \text{ e}/\text{\AA}^3$  of the chemical bonding in aluminum was reported. This value is two orders of magnitude smaller than that for diamond. The preparation of the QCBED measurement sample is difficult for metals because mechanical processes such as cutting and polishing are included. These processes lead to internal strain and defects to the measurement sample. Nakashima et al. described that the accuracy of observed structure factors using QCBED is sufficient for the detection of the electron redistribution [7].

The structures of metals have been observed by X-ray diffraction whereby an X-ray is scattered by an electron in a crystal. The X-ray elastically scattered by the electron forms a diffraction radiation due to the periodicity of the crystal. The intensity of X-ray diffraction peak is proportional to the square of the structure factor. The structure factor is the Fourier coefficient in the Fourier series expansion of the electron density distribution of a crystal. More details on this are given in Section 2.2. The measurement sample of X-ray diffraction is a single crystal or powder. In 1913, Henry and Lawrence Bragg [8] reported the first crystal structure analysis by X-ray diffraction. The structures of simple metals have been reported by Hull [9, 10] using powder X-ray diffraction. The advantage of conventional powder X-ray diffraction is the ease of sample preparation and measurement. For metals, high purity powder samples with submicron- to micron-order particle size suitable for measurements can easily be prepared without a mechanical process. The disadvantage is the low accuracy of observed structure factors.

Synchrotron radiation powder X-ray diffraction techniques have been developed by Japanese and Danish research groups to be compatible the ease of sample preparation and the accuracy of observed structure factors. Synchrotron radiation is an electromagnetic wave radiated when the traveling direction of charged particles changes close to the speed of light. Synchrotron radiation in the X-ray wavelength region is called synchrotron radiation X-ray. X-ray diffraction using synchrotron radiation X-ray is called synchrotron radiation X-ray diffraction. Observation of the accurate structure requires a large number of accurate structure factors. X-ray diffraction by high energy and coherent synchrotron radiation X-ray improves the number and accuracy of structure factors than characteristic X-ray sources. The accurate structures of diamond [5, 11, 12, 13], silicon [13, 14],  $\text{LaB}_6$  [15], and boron nitride [16] were observed by synchrotron radiation powder X-ray diffraction. The magnitude of the electron redistribution of metal is on the order of  $1/100$  of diamond. For this reason, there is no report on the electron distribution of pure metal by synchrotron powder X-ray diffraction. In 2016, Wahlberg et al. [17] successfully observed a potential of the anharmonic vibration of copper at temperatures of 100 and 300 K by synchrotron powder X-ray diffraction. The resolution of the measurement data was  $d > 0.23 \text{ \AA}$ . The report is an example of observation of the accurate structure of metals by state-of-

the-art synchrotron powder X-ray diffraction. The establishment of an accurate observation method for electron density distribution of metals by synchrotron powder X-ray diffraction will enable the accurate observation of the electron density distribution in a wide range of metals.

In this research, aluminum and molybdenum were used as the samples to observe accurate structures because they have properties suitable for the measurement in this research. More details for this are provided in Chapter 2. The former metal is one of the most free-electron-like metals with a Mohs hardness of 2.75. There are a large number of papers regarding electron density distribution and structure factors. The latter metal has *d*-electrons and an electronic state far from free electron approximation with a Mohs hardness of 5.5. Experimental electron distribution and structure factors of molybdenum have not been reported. There are only two reports of theoretical valence electron distribution [18] and structure factors [19] using the first principles calculation.

The purpose of this research is a demonstration of accurate observation of the electron density distribution of aluminum and molybdenum by synchrotron radiation powder X-ray diffraction. The goal is beyond the accuracy of the observed structure factors by QCBED. The lowest two order and the higher order observed structure factors of QCBED have error of less than 0.3% and over 1%, respectively. The improvement of the accuracy of observed electron density distribution is the key of the relationship with mechanical properties of metals and the quantum crystallography. The demonstrations of the observation of accurate electron density distribution by a simple experimental technique such as powder X-ray diffraction accelerate developments of these researches. To accurately observe the static electron density distribution, the synchrotron powder X-ray diffraction must be measured at low temperature. Estimation of the thermal vibration parameters at low temperature is necessary. To establish a method applicable to a wide range of metals and alloys, synchrotron powder X-ray diffraction measurement was employed. Synchrotron X-ray with a high energy and low emittance in the third-generation synchrotron radiation source SPring-8 was used owing to secure the resolution  $d > 0.22 \text{ \AA}$ . For comparison with experimental electron distributions, the static electron density distribution at the ground state was determined using WIEN2k [20]. The accuracy of observed chemical bonding by X-ray diffraction depends on the accuracy of the observed diffraction peaks at a low diffraction angle region. X-ray scattering due to chemical bonding in the low-angle region is stronger than those in the high-angle region. The number of diffraction peaks in aluminum and molybdenum in the low-angle region is low because the unit cells are small and have cubic symmetry. The experimental error of the lowest order two structure factors in aluminum, determined by Nakashima et al. [6], is 1/10 of the experimental error of past observation structure factors. In this research, more than 100 experimental structure factors were determined. The low order structure factors have the accuracy equal to or better than the two structure factors.

## Chapter 2 Difficulties in observation of electron distribution of metals

### 2.1 Purpose and contents of this chapter

This chapter explains the difficulties of observing the electron density distribution in metals and provides reasons for the selection of aluminum and molybdenum as measurement samples. Section 2.2 explains the relationship between the structure factors measured by powder X-ray diffraction and the electron density distribution of crystal. The difficulties of observation of the electron density distribution in metals derive from the small electron density values of the chemical bonding in metals, the low Debye temperatures of metals, and strains or defects in actual metal crystals. Sections 2.3, 2.4, and 2.5 explain the influence of the observation of the electron density distributions from these origins. Section 2.6 explains why aluminum and molybdenum were selected as measurement samples.

### 2.2 Relationship between structure factors and electron density distribution

The structure factor  $F$  is the Fourier coefficient in the Fourier series expansion of electron density distribution of a crystal  $\rho(\mathbf{r})$ .

$$F(\mathbf{H}) = \int \rho(\mathbf{r}) \exp(2\pi i \mathbf{H} \cdot \mathbf{r}) d\mathbf{r}$$

where,  $\mathbf{H}$  is the diffraction vector,  $\mathbf{H} = h\mathbf{b}_1 + k\mathbf{b}_2 + l\mathbf{b}_3$ ;  $h$ ,  $k$ , and  $l$  are the Miller indices of the crystal,  $\mathbf{b}_1$ ,  $\mathbf{b}_2$ , and  $\mathbf{b}_3$  are the reciprocal vectors.  $\mathbf{r}$  is the position vector in the crystal.  $\rho(\mathbf{r})$  is the dynamical electron density distribution containing thermal smearing from the time averaged thermal vibration.

The electron distribution can be determined by the observation of structure factors. Structure factors are the amplitude and phase of the X-ray diffracted by a  $(hkl)$  plane of a crystal. Scattered X-ray waves from one electron are spherical scattered waves. The atomic scattering factor is a superposition of the spherical scattering waves from one electron. The structure factor is a superposition of the associated waves from each atom of a unit cell. The phase difference of the scattered waves from each electron in the atom follows the position of the electron in the classical sense. When considering each electron as a spreading negative charge cloud, the position of the electron becomes the electron density distribution. For this reason, an infinite number of structure factors and electron distributions correspond one to one.

The number of structure factors observed in the diffraction experiment is finite. Each structure factor has an experimental error. The number of observed structure factors is directly related to the resolution of the reproduced electron density distribution. The error of the value of each structure factor affects the error of the value of the electron density. The square of the absolute value of the structure factor is proportional to the diffraction intensity. A finite number of diffraction intensities limit the number of structure factors. We can observe only the diffraction intensities within a diffraction angle of  $2\theta = 0\sim 180^\circ$ . The error of the value of structure factor is a statistical error of counts in the diffraction intensity.

The model of dynamic structure factors  $F_{\text{exp}}$  used in the analysis of experimental data is the superposition of the multiplication of the Fourier transformation of the electron density distribution of a static atom  $f(\mathbf{H})$  and the probability density function of electrons due to the thermal vibration  $T_i(\mathbf{H})$  within a unit cell. This is because the model of the dynamic electron density distribution  $\rho(\mathbf{r})$  is expressed by the superposition of atoms with thermal vibration. The electron density distribution of the dynamical atoms is a convolution of the electron density distribution of a static atom and the probability density distribution of electrons due to thermal vibration. The former is the atomic scattering factor:

$$f(\mathbf{H}) = \int \rho_{\text{at}}(\mathbf{r}) \exp(2\pi i \mathbf{H} \cdot \mathbf{r}) d\mathbf{r}$$

where  $\rho_{\text{at}}(\mathbf{r})$  is the static electron density distribution of atom.  $F_{\text{exp}}$  is expressed by:

$$F_{\text{exp}} = \sum_i^N f_i(\mathbf{H}) T_i(\mathbf{H})$$

where  $i$  shows the label of an atom within a unit cell. The total number of atoms in a unit cell is  $N$ .  $T_i(\mathbf{H})$  consists of harmonic thermal vibration and anharmonic thermal vibration. The isotropic and harmonic thermal vibration term  $T_0(\mathbf{H})$  is given by:

$$T_0(\mathbf{H}) = \exp(-8\pi^2 U_{\text{iso}} |\mathbf{H}|^2)$$

where  $U_{\text{iso}}$  is the isotropic thermal displacement. As  $U_{\text{iso}}$  increases with increasing thermal vibration,  $T_0(\mathbf{H})$  decreases with increasing measurement temperature. That is,  $F_{\text{exp}}$  decreases due to thermal vibration, and diffraction intensity also decreases. This reduces the resolution of the electron density distribution. The probability density distribution of the electrons due to anharmonic thermal vibration is explained in Chapter 4.

Figure 2.1 shows plots of  $T_0(\mathbf{H})$  values of aluminum at 80 and 300 K. The values of  $8\pi^2 U_{\text{iso}}$  were employed from McDonald [21]. The vertical axis represents  $T_0(\mathbf{H})$  and the horizontal axis the diffraction angle  $2\theta$ . The black and red lines are 80 and 300 K, respectively. The wavelength of the incident X-ray is set at 0.328 Å.  $T_0(\mathbf{H})$  rapidly decreases at 300 K. The value of  $T_0(\mathbf{H})$  at  $2\theta = 40^\circ$  is less than 0.2 for 300 K. The decreasing of intensity of diffraction peak of  $2\theta = 40^\circ$  at 300 K is over 80% due to the  $T_0(\mathbf{H})$ . For 80 K, the decreasing is less than 50%.

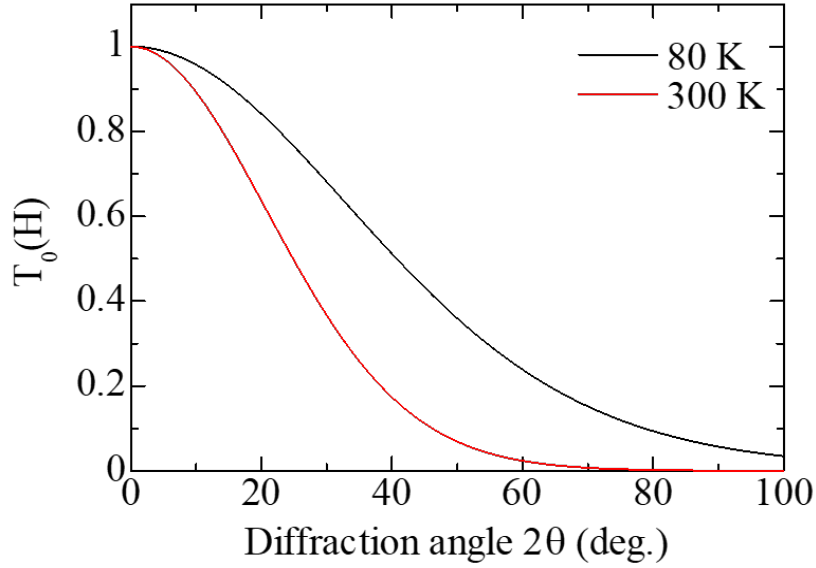


Figure 2.1 Plots of  $T_0(\mathbf{H})$  of aluminum at 80 and 300 K.

### 2.3 Small electron density value of chemical bonding in metals

The fundamental difficulty of observation of the chemical bonding in metals is the difference of  $\sim 10^5$  between the value of the electron density of the inner shell electrons and chemical bonding. As mentioned in Chapter 1, the electron density value of chemical bonding is  $\sim 1.0 \text{ e}/\text{\AA}^3$  for diamond and  $\sim 0.01 \text{ e}/\text{\AA}^3$  for aluminum. Furthermore, the electron density value due to the inner shell electrons around the nucleus is  $\sim 100 \text{ e}/\text{\AA}^3$  for diamond and  $\sim 1000 \text{ e}/\text{\AA}^3$  for aluminum. The ratio of the value of the electron density of the inner shell electron to that of the chemical bonding is 100:1 for diamond and 100,000:1 for aluminum. In any experiment, it is necessary to discriminate a difference between 1% for diamond and 0.001% for aluminum in measurement data. Diamond is an ideal crystal as a model case of observation of chemical bonding. There are a large number of papers based on observation of electron density distributions. The forbidden 222 reflection of diamond in X-ray diffraction was reported by W. H. Bragg in 1921. Chemical bonding of aluminum was first reported in 2011 by P. N. H. Nakashima et al. To select a model case of observation of chemical bonding in metals, it is necessary to select metals of which the ratio is small as possible.

The ratio of the value of the electron density of inner shell electrons to that of chemical bonding in metals can be evaluated by the valence electron density. The valence electron density is expressed by:

$$\rho_v = \frac{Z n_{uc}}{V_{uc}}$$

where,  $Z$  is the number of valence electrons in an isolated atom,  $n_{uc}$  is the number of atoms in a unit cell, and  $V_{uc}$  is the volume of a unit cell. The numbers of valence electrons are 1, 2, 3, and 4 for groups 1, 2, 13, and 14 in the periodic table, respectively. Transition metals, which are groups 3 to 12, have multiplex values. Assuming that the all valence electrons contribute to the formation of the valence electron density, the value  $\rho_v/X$ , the division of  $\rho_v$  by the number of inner-shell electrons  $X$ , shows

the difficulty of detection of chemical bonding in metals.

Table 2.1 shows  $Z$ , the number of electrons per cubic centimeter  $n$ , the valence electron density  $\rho_v$ ,  $X$ , and  $\rho_v/X$  for representative metals. The values  $Z$  of transition metals and  $n$  are employed from Ashcroft [1].

$$n = 6.022 \times 10^{23} \times \frac{Z\rho_m}{A}$$

$6.022 \times 10^{23}$  is the number of atoms per mole,  $\rho_m$  is the mass density in gram per cubic centimeter, and  $A$  is the mass of an atom. The largest value of  $\rho_v/X$  is beryllium, second to this is aluminum.

Table 2.1 The number of electron per cubic centimeter  $n$ , the valence electron density  $\rho_v$ , and  $\rho_v/X$  for representative metals.

Element	$Z$	$n$ ( $10^{22}$ /cm <sup>3</sup> )	$\rho_v$ (e/Å <sup>3</sup> )	$X$	$\rho_v/X$
Be	2	24.7	0.247	2	0.123
Mg	2	8.61	0.086	10	0.009
Ca	2	4.61	0.046	18	0.003
Al	3	18.1	0.181	10	0.018
Cu	1	8.47	0.085	28	0.003
Ag	1	5.86	0.059	46	0.001
Fe	2	17	0.170	24	0.007
Zn	2	13.2	0.131	28	0.005
Nb	1	5.56	0.056	40	0.001

The value of the electron redistribution from a superposition of isolated atoms in metals is  $\sim 0.01$  e/Å<sup>3</sup>. The approximation of the electron density distribution in a crystal by superposition of the spherical electron density distribution of isolated atoms is called the independent atom model (IAM). Figure 2.1 shows a schematic representation of the electron density distribution in an actual crystal and the IAM. The red circles represent the spherical electron density distribution of atoms, and the red bars between the nearest atoms show the electron redistribution due to a periodic arrangement of atoms. The redistribution in an actual crystal is not reproduced by the IAM. In metal, the difference between the structure factors from the electron density distribution of an actual crystal and from the IAM is small. This is because electron redistribution due to chemical bonding is small. Nakashima et al. reported that the value of the redistribution in aluminum was  $0.05$  e/Å<sup>3</sup>. This is owing to the detection of the difference in the value of about 1% at the two lowest order structure factors between the experiment and IAM. Here, the order of the structure factor  $F(\mathbf{H})$  is expressed by the  $hkl$  of  $\mathbf{H}$ . The order decreases with decreasing the value of  $h^2 + k^2 + l^2$ . Detection of metallic bonding requires (i) a high statistical accuracy of the structure factors for detecting a slight change of the structure factor from a neutral atom and (ii) large number of structure factors for asymptotic to a true electron distribution.

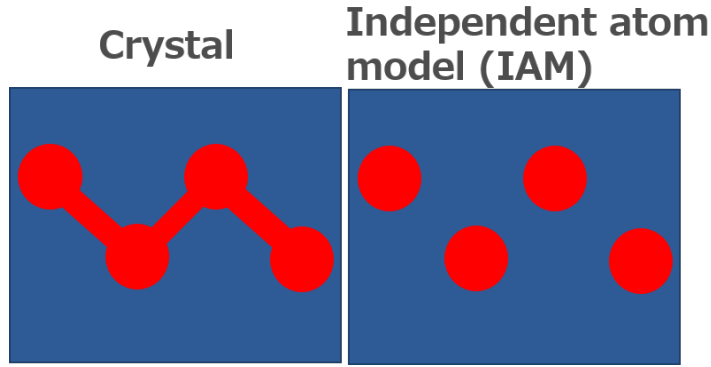


Figure 2.2 A schematic representation of electron density distribution in an actual crystal and IAM.

## 2.4 Low Debye temperature

The Debye temperature is the temperature at which all normal modes of thermal vibration are excited within the Debye model of specific heat. The Debye temperature of metals is generally lower than that of covalent crystals. The Debye temperature  $\theta_D$  is defined by  $k_B\theta_D = h\nu_{\max}$ , where  $k_B$  is the Boltzmann constant and  $h\nu_{\max}$  is the maximum frequency in the normal mode. Therefore,  $\theta_D$  is an index of the thermal vibration at a certain temperature. A higher Debye temperature means less susceptible of the thermal vibration to temperature. For example,  $U_{\text{iso}}$  is expressed by the following equation:

$$U_{\text{iso}} = \frac{3\hbar^2 T}{mk_b\theta_D^2} \left\{ \Phi\left(\frac{\theta_D}{T}\right) + \frac{1}{4} \frac{\theta_D}{T} \right\}$$

where,  $\hbar$  is Planck's constant over  $2\pi$ ,  $T$  is the measurement temperature,  $m$  is the atomic mass,  $\Phi$  is the Debye integral. As can be seen, the larger  $\theta_D$  derives a smaller  $U_{\text{iso}}$ .

Table 2.2 shows the Debye temperature of representative pure metals at 0 K. All Debye temperatures are less than 500 K except for beryllium, chromium, ruthenium, and osmium. In covalent crystals, for instance, silicon is 645 K and diamond is 2230 K.

Table 2.2 Debye temperature of representative pure metals at 0 K.

Element	$\theta_D$ (K)						
Li	344	Mn	410	Nb	275	Hf	252
Be	1440	Fe	470	Mo	450	Ta	240
Na	158	Co	445	Ru	600	W	400
Mg	400	Ni	450	Rh	480	Re	430
Al	428	Cu	343	Pd	274	Os	500
K	91	Zn	327	Ag	225	Ir	420
Ca	230	Ga	320	Cd	209	Pt	240
Sc	360	Rb	56	In	108	Au	165
Ti	420	Sr	147	Cs	38	Hg	71.9
V	380	Y	280	Ba	110	Tl	78.5
Cr	630	Zr	291	La	142		

Figure 2.3 shows  $T_0(\mathbf{H})$  at 300 K using the Debye temperature of aluminum and diamond. The vertical axis represents  $T_0(\mathbf{H})$  and the horizontal axis the diffraction angle  $2\theta$ . Black and blue lines are aluminum and diamond. The wavelength of the incident X-ray is set at 0.328 Å. The decreasing of intensity of diffraction peaks at  $2\theta = 40^\circ$  due to  $T_0(\mathbf{H})$  at 300 K in aluminum and diamond are 82% and 35%, respectively. A small Debye temperature leads to a large decreasing of the diffraction intensity.

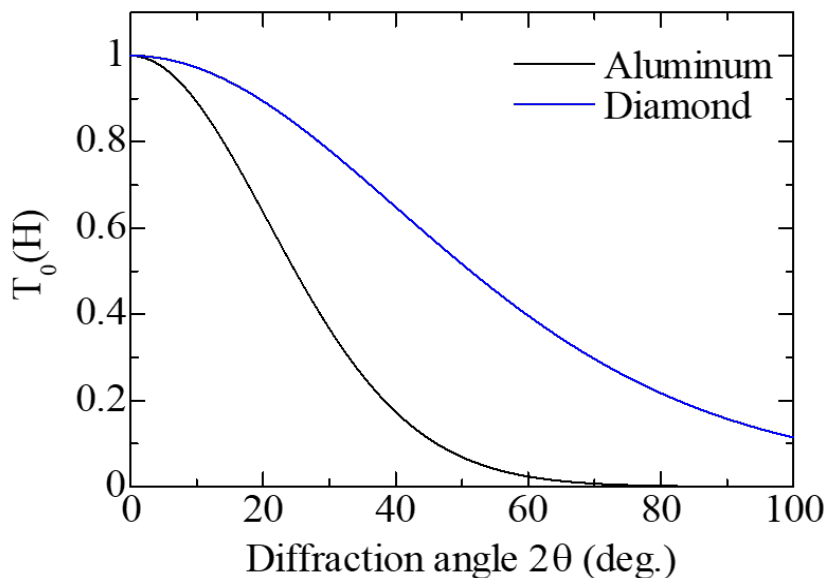


Figure 2.3  $T_0(\mathbf{H})$  at 300 K using Debye temperature of aluminum and diamond.

Figure 2.4 shows the results of the powder X-ray diffraction measurements of aluminum at 30 K and 600 K. The vertical axis represents the intensity and the horizontal axis the diffraction angle  $2\theta$ . Further experimental details are in Chapter 3. The black lines in both upper and bottom figures show the intensities measured at 30 K and 600 K respectively. The delta function-like peaks show the intensity of the diffraction X-ray. Diffraction X-ray is caused by interference of the scattered X-ray from the measurement sample. The area of each diffraction peak gives the diffraction intensity. Because of the difference in  $U_{\text{iso}}$  between 30 K and 600 K, the diffraction peaks in 600 K are buried by background intensity at  $2\theta = 40^\circ$ . The decrease in the number of observed diffraction peaks becomes prominent when  $\theta_D$  is small even at the same temperature. For this reason, metals with a low Debye temperature require a low-temperature measurement by securing the number of observed structure factors.

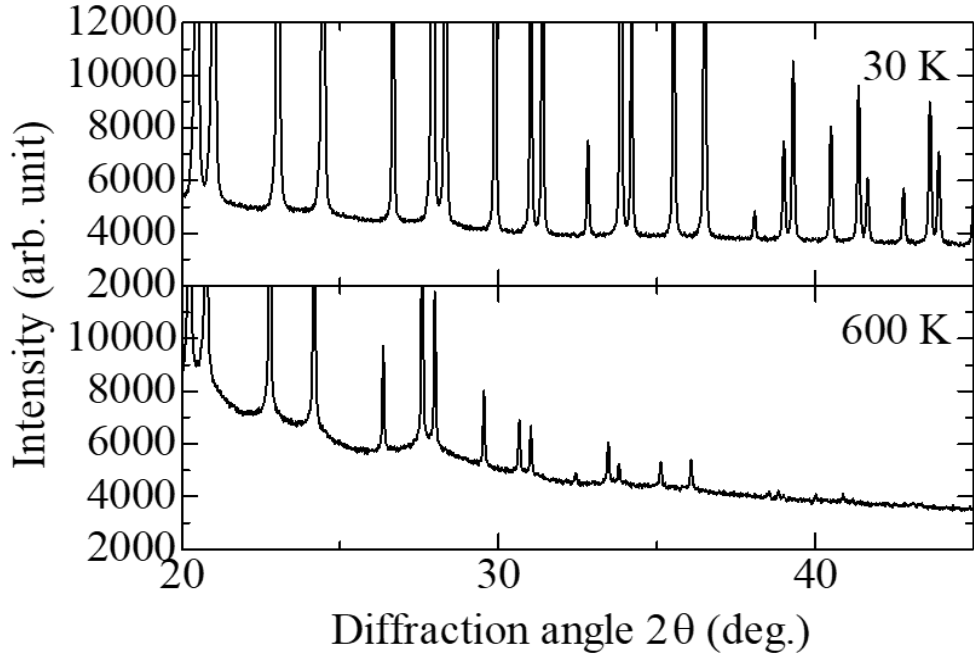


Figure 2.4 Results of powder X-ray diffraction measurements of aluminum at 30 K and 600 K.

Figure 2.5 is a plot of the three sets of structure factors of aluminum. These were calculated from (1) the electron density distribution of the IAM, (2) the theoretical electron density distribution by WIEN2k, and (3) the structure factors of (2) multiplied by the value of  $T_o(\mathbf{H})$  at 100 K. The horizontal axis represents  $\sin \theta / \lambda$ . The inserted figure at the left-side shows an expanded view of the lowest three structure factors of  $hkl = 111, 200,$  and  $220$ . Deviations of the values of the structure factors due to electron redistribution from the IAM are  $\sim 1\%$  in the narrow range of a low diffraction angle. The right-side figure shows an expanded view of the range from 1.5 to 2 on the horizontal axis. Owing to the harmonic thermal vibration of 100 K, there is a difference in the value of the structure factors of 65%. The 1% difference in the lower order structure factor is easily changed by the estimation of the thermal vibration. Increasing the number of structure factors increases the accuracy of the estimation of the thermal vibration. For this reason, a large number of structure factors must be observed.

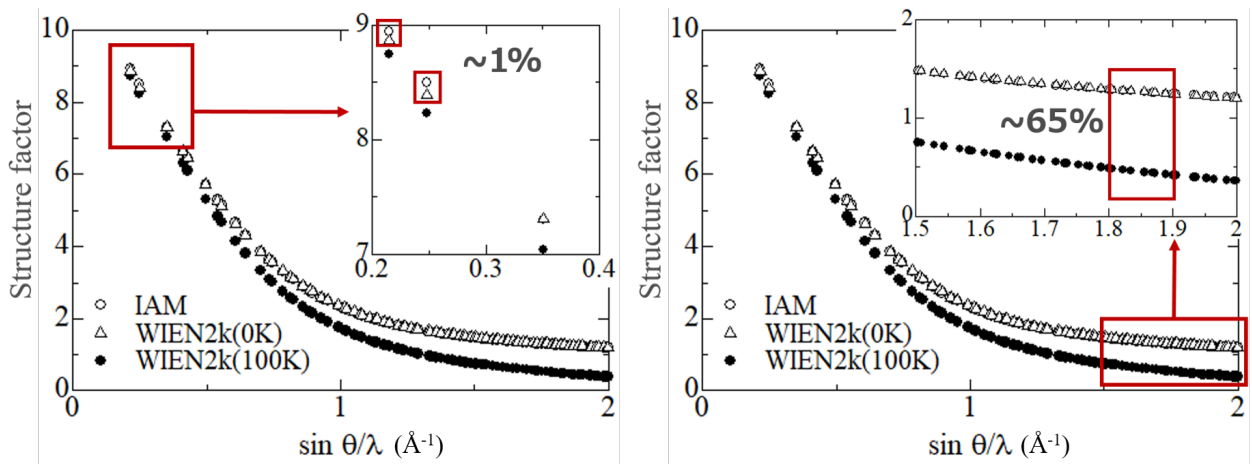


Figure 2.5 Plot of three sets of structure factors of aluminum.

Figure 2.6(a) is expanded view of the background intensity of the results of powder X-ray diffraction measurements in aluminum at 30 K and 600 K. The black and red lines show the results at 30 K and 600 K. The vertical axis represents the intensity and the horizontal axis the diffraction angle  $2\theta$ . At 30 K and 600 K, the shape of background is considerably different. This is caused by an increasing of the contribution of the thermal diffuse scattering. Further details regarding thermal diffuse scattering are given in Chapter 4. Figure 2.6(b) shows a schematic representation of the diffraction peak and intensity of thermal diffuse scattering. The intensity of thermal diffuse scattering takes a maximum value at the  $2\theta$  position of the diffraction peak. Since the intensity of the diffraction peak apparently increases, the estimation of  $T_i(\mathbf{H})$  becomes inaccurate. For an accurate observation of the electron density distribution of metals, the thermal diffuse scattering intensity must be estimated.

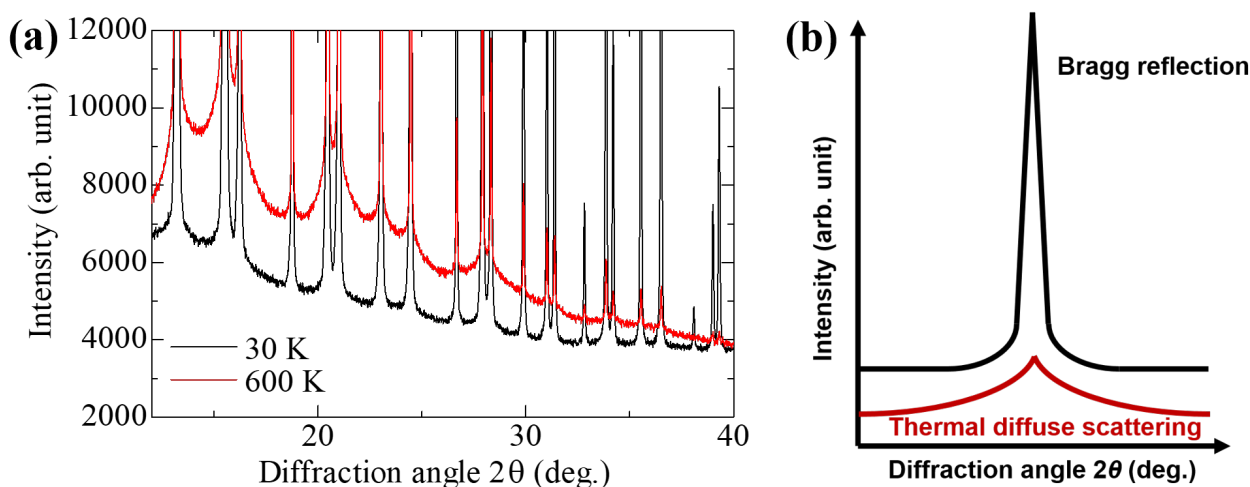


Figure 2.6 (a) The expanded view of the background intensity of results of powder X-ray diffraction measurements in aluminum at 30 K and 600 K. (b) A schematic representation of diffraction peak and intensity of thermal diffuse scattering.

## 2.5 Strain and defect

The internal strain and defects of metals affect the widths of diffraction peaks. This leads to an inaccurate estimation of the diffraction intensity. The softness of metals leads to an easy introduction of the internal strain. The internal strain changes the interplanar spacing  $d$  in the Bragg's equation. Defects disturb the periodicity of a crystal lattice. These cause a phase shift of scattered waves. The phase shifts affect the diffraction intensity through a change of structure factors.

Figure 2.7 shows the diffraction peaks of  $hkl = 222$  and  $400$  in the measurement results of the powder X-ray diffraction of copper. The vertical axis represents the intensity and the horizontal axis the diffraction angle  $2\theta$ . Both ranges of the horizontal axis is  $0.4^\circ$ . A decrease in the width of the diffraction peak in the  $111, 222, \dots$  series and an increase in the width of the  $200, 400, \dots$  series were observed. For instance, the values of the full-width-half-maximum of  $222$  and  $400$  diffraction peaks are  $0.06$  and  $0.09^\circ$ , respectively. This is the effect of internal distortion.

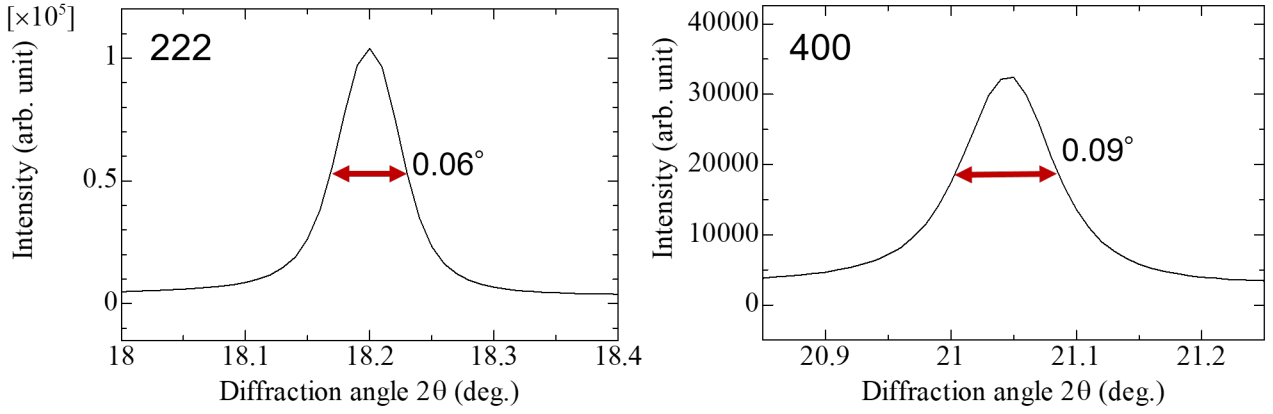


Figure 2.7 Diffraction peaks of  $hkl = 222$  and  $400$  in the measurement results of powder X-ray diffraction of copper.

## 2.6 Aluminum and molybdenum

Aluminum and molybdenum are suitable metals for the accurate observation of the electron density distribution. Aluminum has the second largest  $\rho_v/X$  value in simple metals. Ogata et al. [2] reported that the intrinsic stacking fault energy of aluminum is very high. Therefore, the amount of stacking faults is smaller to that of other metals with the same face-centered cubic (fcc) structure. The observed electron density distribution by synchrotron powder X-ray diffraction can be compared with the report of Nakashima et al. [6]. Table 2.3 shows the error ratio of reported observed structure factors in aluminum. The ratio is defined by  $\sigma_{F_{\text{obs}}}/|F_{\text{obs}}|$  for each index structure factor.  $\sigma_{F_{\text{obs}}}$  is value of error and  $F_{\text{obs}}$  is value of observed structure factor. Nakashima et al. [6] and Fox [22] used electron diffraction. Takama et al. [23] used Pendellosung-beat measurement. de Macro [24] used single crystal X-ray diffraction. The others [25, 26, 27, 28, 29, 30] are results of powder X-ray diffraction. The results of Nakashima et al. were reported in 2011, while other results have been reported before 2000. The maximum number of observed structure factors before 2000 is eleven. The minimum error of the observed structure factor before 2000 is  $\sim 0.5\%$ , of Takama et al. Nakashima et al. [6] showed that these observed structure factors have no unified picture of electron distribution of the chemical bonding in aluminum. They used only the lowest two structure factors to observe a metallic bonding. Other structure factors are the same as those of the neutral atom. The error of these two are less than  $0.24\%$ . The observed bonding electron distributions almost agreed with a calculated electron distribution by WIEN2k.

Table 2.3 The error ratio of reported observed structure factors in aluminum.

$hkl$	Nakashima [6]	Fox [22]	Takama [23]	Batterman [25]	Jarvinen [27]	de Marco [24]	Racchah [26]	Rantavuori [28]	Inkinen [30]	Bench [29]
1 1 1	0.11	0.45	0.34	1.62	0.69	0.49	0.68	0.45	0.79	1.51
2 0 0	0.24	0.24	0.59	1.70	1.21	0.80	0.72	0.48	0.95	0.96
2 2 0	1.09		0.41	1.83	1.26	0.80	0.83	0.55	1.10	0.97
3 1 1	0.90		0.30	1.87			0.90	0.45	1.05	1.07
2 2 2	1.07		0.46	2.10			0.93	0.77	1.40	0.92
4 0 0	1.03			2.74			1.04	1.05	1.58	1.02
3 3 1	3.77		0.38	2.82			1.13	0.94	1.33	1.48
4 2 0	0.19		0.58	2.78			0.96	0.96	1.36	1.47
4 2 2	2.00		0.85	3.42			1.07	1.07	1.28	4.16
3 3 3	4.35			4.00						4.05
5 1 1	2.15			4.00						4.02
4 4 0	9.76									
5 3 1	11.36									
4 4 2	2.22									

Molybdenum is a hard metal with a Mohs hardness of 5.5. Because of its hardness, it can be expected to suppress introductions of strain and defects. Molybdenum has the simplest system of the chromium group metals. That is, there is no magnetism and spin-orbit interaction is very small. There are no reports of the observed structure factors of molybdenum. The theoretical electron density distribution, theoretical structure factors, the experimental and theoretical Fermi surface, and band structures were reported [18, 19, 31, 32].

Among other difficulties, the structures of pure metals with high symmetry and small lattice constants prevent the observation of accurate structure factors. A highly symmetrical structure leads to a reduction of the number of diffraction peaks in powder X-ray diffraction. The structure also introduces systematically weak intensity diffraction peaks. High multiplicity for diffraction peaks in the low angle region of diffraction angle  $2\theta$  produces a large diffraction intensity. The ratio of the diffraction intensity between the first diffraction peak and the 100th in aluminum or molybdenum is 1,000,000: 1. The ratio in counts is 1000:1. The intensities of the systematically weak diffraction peaks are less than 1/4 of the surrounding diffraction peaks.

The fact that observed structure factors have no unified picture of the electron density distribution of chemical bonding is attributable to errors in the observed structure factors. Figure 2.9 shows deviation from the IAM with reported observed structure factors in aluminum. The vertical axis shows the deviation and the horizontal axis the  $\sin \theta / \lambda$ . The calculation method of the deviation is defined in Section 4.7. All deviations at the lowest order are normalized to 1. The deviation results from the chemical bonding in principle. The deviation of the second lowest structure factor of Nakashima et al. have a significant difference to that of the lowest structure factor. All other deviations of higher order from the lowest deviations are the same as their lowest deviation. An observation of the

deviation of structure factors by chemical bonding in aluminum requires an accuracy of the structure factors which is same as Nakashima et al. in the lowest two. This accuracy requires a statistical error of  $\sim 0.34\%$  in the powder X-ray diffraction intensity.

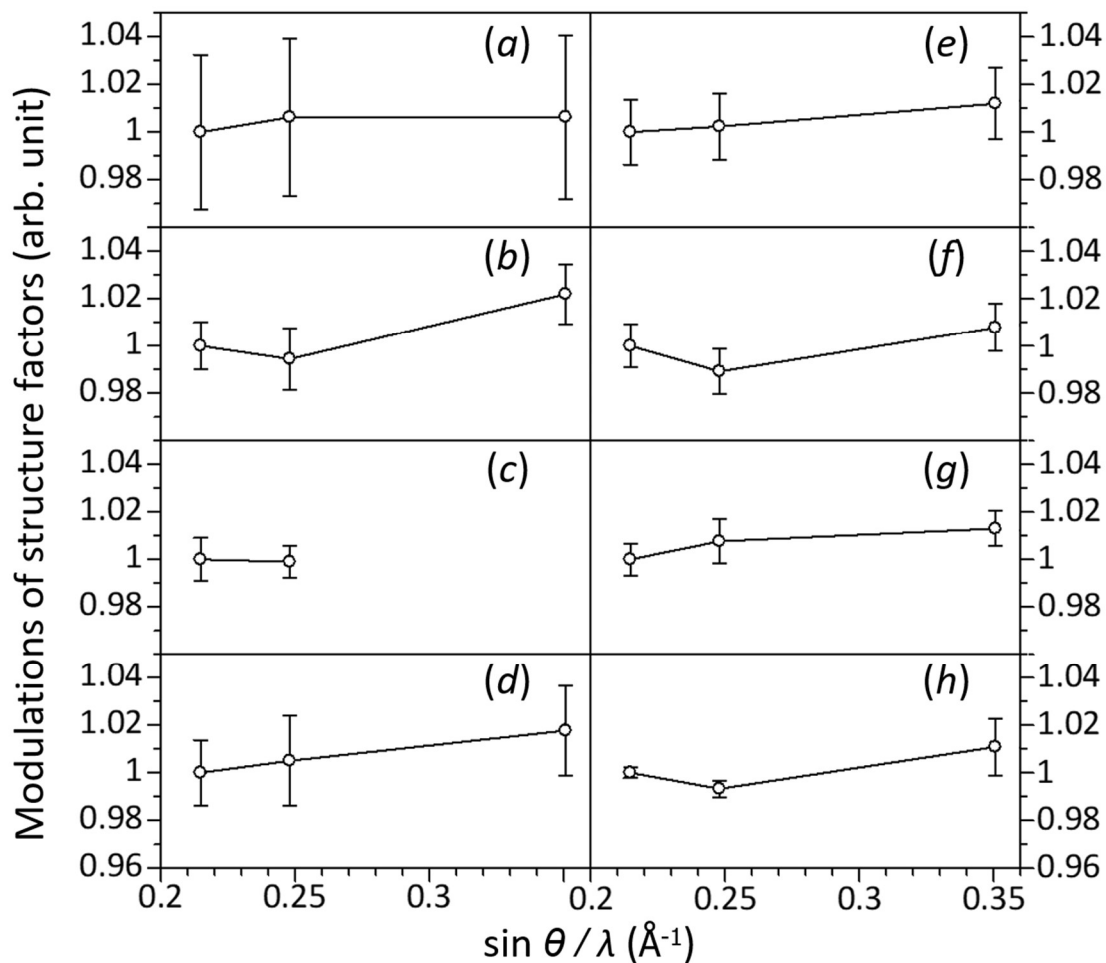


Figure 2.9 Deviations from IAM with reported observed structure factors in aluminum. (a) Batterman et al. [25], (b) de Marco [24], (c) Fox and Fisher [22], (d) Jarvinen et al. [27], (e) Raccah and Henrich [26], (f) Rantavuori and Tanninen [28], (g) Takama et al. [23], (h) Nakashima et al. [6].

## Chapter 3 Measurement of synchrotron powder X-ray diffraction

### 3.1 Introduction

The synchrotron powder X-ray diffraction of aluminum and molybdenum were measured. In X-ray diffraction, information about electron distribution is included in the structure factor. Observation of the electron distribution for one conduction electron in LaB<sub>6</sub> [15] required the resolution of  $d > 0.23 \text{ \AA}$  in the measurement data of the powder X-ray diffraction. A component of the harmonic oscillation of atomic thermal vibration can be observed by decreasing the structure factor with respect to the diffraction angle  $2\theta$ . The higher order components of the thermal vibration are anharmonic terms. The anharmonic terms of thermal vibration can be analyzed by electron distribution modeling using a Gaussian probability density function. As X-ray diffraction is the elastic scattering of X-rays, thermal diffuse scattering is included in the background intensity.

To measure accurate powder X-ray diffraction data, it is necessary to deal with oxidation and distortion of the aluminum and molybdenum powder. To prevent oxidation, exposure of the two powders to the atmosphere must be avoided. The two powders were stored in a desiccator evacuated with a rotary pump. The sealing of the powder in the Lindemann glass capillary for X-ray diffraction measurement was carried out in a glove box under inert gas, as necessary. To prevent distortion, milling in a laboratory cannot be done. It is fundamental to purchase aluminum and molybdenum powder of a suitable particle size for accurate measurement.

To improve the resolution of measurement data, high-energy incident X-rays, low temperature measurement, and measurement of the diffraction peaks in a high diffraction angle region are required. A small value of resolution  $d$  value indicates the measurement of a large number of diffraction peaks and can be expressed by  $d = \lambda/(2 \sin \theta)$ , where  $\lambda$  is the wavelength of the incident X-ray, and  $\theta$  is the diffraction angle. The relationship between the wavelength  $\lambda$  and energy  $E$  is  $E = 12.4/\lambda$ . The units of measurement for  $E$  and  $\lambda$  are keV and  $\text{\AA}$ , respectively. The resolution  $d$  decreases with the increase in the maximum diffraction angle  $\theta$  of measurement region. High-energy incident X-rays have short wavelengths, which reduce the value of  $d$ . Low-temperature measurements reduce the effects of the atomic thermal vibrations. The thermal vibration leads to a rapid attenuation of diffraction peak intensities to the diffraction angle. Increasing the intensity of the thermal diffuse scattering increases the background intensity. The Debye temperatures of aluminum and molybdenum are 390 and 377 K, respectively. The low-temperature measurement enables the observation of the diffraction peaks in the high angle region.

High-energy incident X-rays reduce the extinction effect. The extinction effect, comprising primary and secondary, in X-ray diffraction decreases low order structure factors. The primary extinction effect depends on the size of perfect crystals in the measurement sample. In the powder sample, the size of the perfect crystal was, at most, equal to the particle size of the powder. The extinction distance  $t$  is expressed by  $t = V/(\lambda F)$ , where  $V$  is the volume of the unit cell,  $\lambda$  is the wavelength of the incident X-ray, and  $F$  is the structure factor. The larger the extinction distance compared to perfect crystals, the smaller the primary extinction effect. Short incident X-ray

wavelengths increase the extinction distance. Low-order structure factors have large values, which reduce the extinction distance. The secondary extinction effect depends on the degree of parallelism between perfect crystals. In the powder sample, the direction of perfect crystals is random.

To improve the counting statistics of the X-ray diffraction data, it is necessary to divide the measurement range of the diffraction angle  $2\theta$ , and to ensure stability of the X-ray source and high intensity of the incident X-ray. Increasing the measurement counts improves the statistical error. The intensities of the X-ray diffraction peaks were decreased exponentially with respect to the diffraction angle  $2\theta$ . The ratio of the counts of the diffraction peaks between  $2\theta = 8^\circ$  and  $100^\circ$  in aluminum is 10,000:1. The saturation of counts in the Imaging Plate detector limits the counts of diffraction peaks at high angles of  $2\theta$ . To improve the counting statistics of the diffraction peaks in the high angle region, it is necessary to divide the measurement range into the low angle side and the high angle side. Increasing the counts of diffraction peaks requires high-intensity incident X-rays. For a prolonged measurement in the high angle side, an X-ray source with good stability is necessary.

Metal foil is useful for removing the background intensity with a specific wavelength. The background intensity of X-ray diffraction comprise thermal diffuse scattering, X-ray fluorescence from sample, air scattering, scattering by capillaries, among others. The wavelength of the X-ray fluorescence for each element has a unique value. X-ray fluorescence can be reduced by placing metal foil between the diffracted X-ray and the detector. The selection of the optimum metal foil and the setting place are necessary to utilize metal foils.

The third-generation synchrotron radiation source SPring-8 satisfies the requirements of this measurement. BL02B2 is a beamline for high-energy synchrotron powder X-ray diffraction. The maximum energy of the incident X-ray of BL02B2 is 37.7 keV. Low temperature measurement is available with a helium gas cooling device. Owing to the movement of the Imaging Plate detector, it is possible to measure the high angle region of the diffraction angle  $2\theta$ . Metal foil can be placed on the front of slit of the Imaging Plate cassette. Split measurements can be performed on the low angle side and high angle side of  $2\theta$ . SPring-8 is the most stable synchrotron X-ray source in the world.

The purpose of the experiments is to accurately measure the powder X-ray diffraction dataset of pure metals. The diffraction data for a charge density study of metal require an electron density resolution better than  $0.01 \text{ e}/\text{\AA}^3$ . The electron density between the nuclei of pure metals is evaluated by the average valence electron density per unit cell. In trivalent aluminum, the density is  $0.18 \text{ e}/\text{\AA}^3$ .

From the measurement results of the QCBED structure factors in aluminum by Nakashima et al. [6], the observation of chemical bonding in aluminum requires an errors of 0.24% in counts at the diffraction peaks of the lowest-order two structure factors. For a statistical error,  $\sim 90,000$  counts are necessary.

## 3.2 Experimental

This section explains experimental devices, equipment, and the diffractometer in this research.

3.2.1 explains the glovebox system for the sample preparation. 3.2.2 shows the X-ray diffractometer at SPring-8 BL02B2. 3.2.3 shows the examination of a new Imaging Plate reader.

### 3.2.1 Glovebox

Figure 3.1 shows the glovebox system used for sample preparation. It was used to prevent the oxidation of the powder during sample preparation. The black frame is the glovebox, the blue frame is a vacuum chamber, the red frame is a hygrometer, and the orange frame is an oximeter and an automatic internal pressure regulator. The glovebox is under an Ar atmosphere due to the flow of Ar gas from the Ar cylinder. In the system, both the moisture and oxygen concentration can reach an order of  $\sim 1000$  ppm order. The powder was sealed in a Lindemann glass capillary using the following system.



Figure 3.1 The glove box system used for sample preparation.

### 3.2.2 Large Debye-Scherrer camera

Figure 3.2 shows the large Debye-Scherrer camera installed at the SPring-8 beamline BL02B2. The measurement sample was placed on the  $2\theta$  axis. The sample was rotated during measurement. The measurement temperature was set by a gas flow device. The X-ray was incident to the sample through the collimator. The diffracted X-ray was recorded on an Imaging Plate detector. BAS IP MS 2040E was used for measurement.

Figure 3.3 shows a schematic view of the arrangement of the large Debye-Scherrer camera. The red arrows represent the incident and diffracted X-rays. The black circle represents the sample. The diffraction angle is between the direction of the incident and diffraction X-rays. The green and orange curves indicate the two measurement positions of the Imaging Plate. The measurement region of a single Imaging Plate is  $78^\circ$  in  $2\theta$ . The starting position of  $2\theta$  in the low-angle side was  $2\theta = 0^\circ$ . The starting position on the high angle side was  $2\theta = 30^\circ$ .

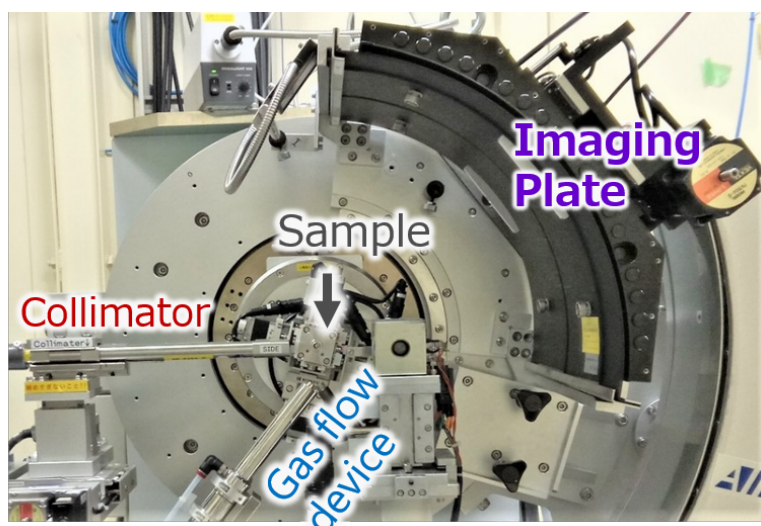


Figure 3.2 The large Debye-Scherrer camera installed at SPring-8 beamline BL02B2.

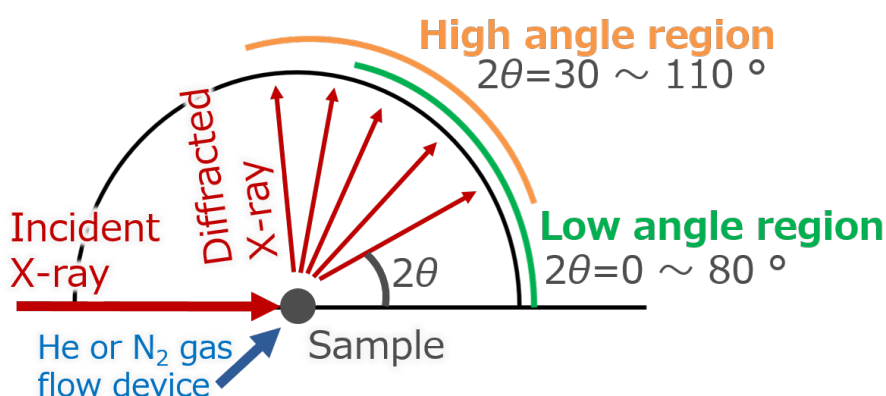


Figure 3.3 A schematic view of the arrangement of the large Debye-Scherrer camera.

### 3.2.3 Imaging Plate reader

A new Imaging Plate reader that reproduces the reading result of the Imaging Plate from Fuji BAS-2500 is necessary. The IP reader Fuji BAS-2500 has been employed at beamline BL02B2. The reader has, so far, successfully observed a large number of electron distributions. The Imaging Plate reader cannot be maintained in the future due to a withdrawal of Fuji from support work of the Imaging Plate reader series.

A candidate for a new Imaging Plate reader is the Rigaku RAXIA-Di. The dynamic range of the Imaging Plate is over  $10^6$ . To realize the linearity of the reading result of photoemission from the Imaging Plate, the Imaging Plate reader usually uses two photomultiplier tubes. The sensitivity of the photomultiplier tube can be tuned by voltage. An optimized setting for reading of the Imaging Plate at BL02B2 is needed for accurate measurement of the synchrotron powder X-ray diffraction.

The synchrotron powder X-ray diffraction measurement of  $\text{CeO}_2$  was carried out at SPring-8 beamline BL02B2. This is an investigation of the reproducibility of the reading result in IP reader Rigaku RAXIA-Di. To compare the results between the BAS-2500 and Rigaku RAXIA-Di, the measurement results of the powder X-ray diffraction of the standard sample  $\text{CeO}_2$  was read by RAXIA.

To investigate the position dependence of the measurement results by reading the position of the Imaging Plate, seven 2-dimensional (2-D) diffraction data were measured in one Imaging Plate. The slit width was 20 mm. The measurement position in the Imaging Plate was moved to 21 mm, and the initial measurement position was 20 mm.

Figure 3.4 shows the results of the Rietveld refinement of the 1-dimensional (1-D) diffraction data from RAXIA, auto-wave.exe was used for the analysis. The vertical axis represents the intensity and the horizontal axis the diffraction angle  $2\theta$  for each figure. The refined parameters were the scale factor  $s$ , background parameters  $b1$  to  $b12$ , zero point adjustment parameter  $t1$ , lattice constant, parameters of half width of diffraction peaks  $w$ ,  $v$ , and  $u$ , asymmetric parameter of the half width of diffraction peaks  $a_2$ , parameter of the ratio of the Gaussian and Lorentzian in the pseudo Voigt function,  $eta$ , the ratio of half width,  $eps$ , and the temperature factors of Ce and O. The full width at half maximum of the measured diffraction peaks are larger than those of the pseudo Voigt function. This is remarkable at the high angle region. The deviation between the peak position  $2\theta$  in the measurement data and that of the pseudo Voigt function cannot be corrected by  $t_1$ . The peak positions of the measurement data and fitting results are reversed  $2\theta = 20^\circ$ . From the middle angle region to the high angle region, the deviation amount for each peak are different.

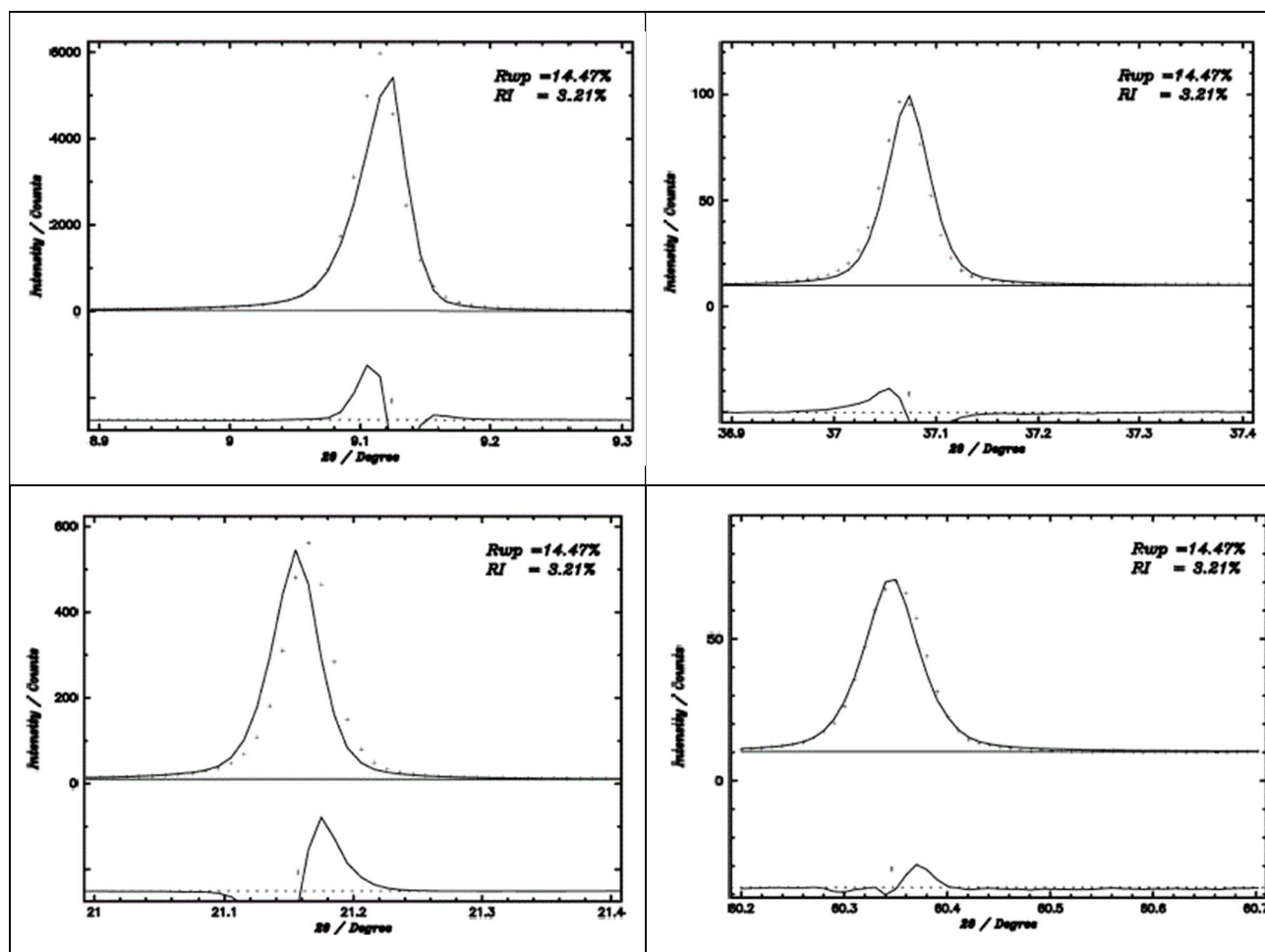


Figure 3.4 The results of Rietveld refinement of 1-dimensional diffraction data from RAXIA-Di.

Figure 3.5 shows the superposition of the diffraction peaks in seven measurement data within

the same Imaging Plate. This is to investigate the dependence of the reading position of the Imaging Plate for the deviation. The measurement is carried out at room temperature. The incident X-ray wavelength is  $0.328 \text{ \AA}$ . The exposure time is 5 minutes. The upper side shows an expanded view of the diffraction peak with the maximum intensity. The peak position increases with the increasing vertical position (mm) of the Imaging Plate. This phenomenon is maintained at a low angle. The bottom side shows an expanded view of the peak in the medium angle region. The phenomena is reduced around  $2\theta = 40^\circ$ .

Fuji BAS-2500 was employed in the present powder X-ray diffraction measurement. This is because the deviation of the peak position between the experiment and fitting in the Rigaku RAXIA-Di considerably affects the estimation of the diffraction intensity.

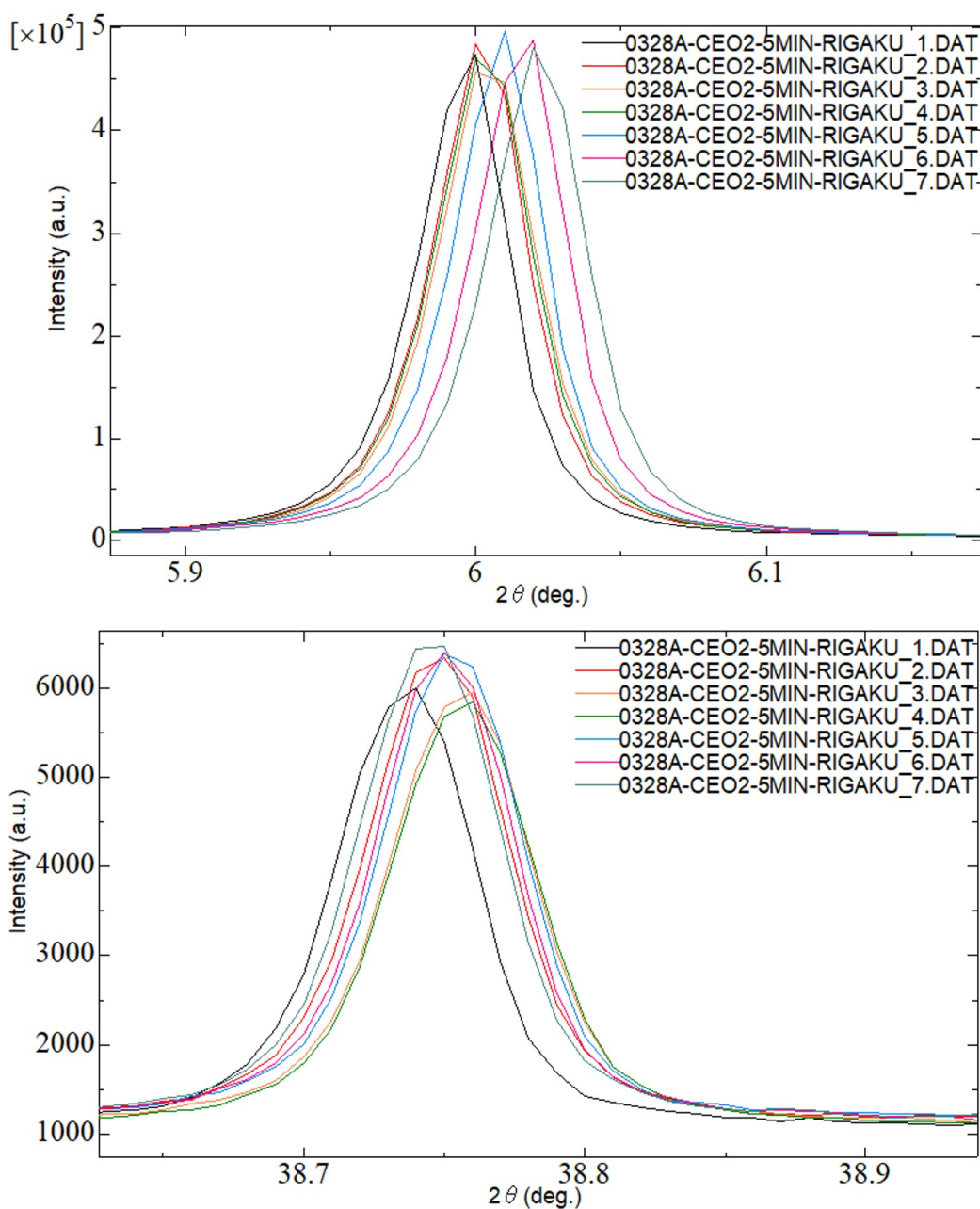


Figure 3.5 The superposition of diffraction peaks in seven measurement data within the same Imaging Plate.

### 3.3 Preparation of measurement sample

Aluminum powder and molybdenum powder were brought from the Kojundo chemical laboratory and Nilaco Corporation, respectively. The purity of the powders was 99.9%. The particle sizes were 3  $\mu\text{m}$  for the aluminum and 3-5  $\mu\text{m}$  for the molybdenum powder. Both powders were not milled to avoid introduction of internal strains and defects of grains.

The aluminum powder was sealed in a Lindemann glass capillary with Ar gas. The internal diameter of the capillary is 0.4 mm and 0.2 mm for aluminum and molybdenum, respectively. The glovebox was used in the process. Ar gas was made to flow through the glovebox after the evacuation of air with a rotary pump. The hygrometer and oximeter showed  $\sim 1000$  ppm. The capillary was inserted in a straw. The capillary and tube were fixed with mending tape. Two sets of these and one spatula were put in a styrene case. The aluminum or molybdenum powder, grease tube, a piece of parafilm and weighing papers were also put in the case. The case was then placed in the pass box in the glovebox system. The pass box was evacuated up to a pressure of -0.1 MPa. The box was filled with Ar gas at a pressure up to 0 MPa. Then, the case was moved into the glovebox.

The aluminum and molybdenum powders were packed into the capillaries in the glovebox. Small amounts of aluminum or molybdenum powder were picked up and dropped in the capillary. The powder dropped to the bottom of the capillary by vibration through the tube. A small amount of grease was put out on a weighing paper. The upper part of the capillary was sealed using silicon grease with Ar gas. The capillaries and others were put into the styrene case. The case was removed from the glovebox through the pass box. The capillary was sealed using a fire from a lighter outside of the glovebox.

Figure 3.6 shows the prepared sample of aluminum in a sample case. One sample was prepared and was attached to a small amount of black clay at the edges of the capillaries. The sample was fixed in the sample case with the clay. The sample was labelled "Al<sub>2</sub>", with a length of 54 mm. The molybdenum samples were fixed in the sample case using the same method.

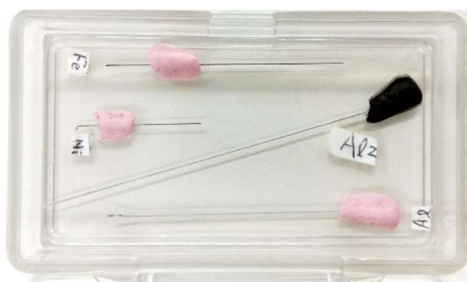


Figure 3.6. The prepared samples of aluminum.

### 3.4 Synchrotron powder X-ray diffraction experiment of aluminum and molybdenum

Synchrotron powder X-ray diffraction measurements were carried out with a transmission

arrangement using the large Debye-Scherrer camera installed at the large synchrotron radiation facility SPring-8 beamline BL02B2. BL02B2 is a dedicated beamline for crystal structure analysis by synchrotron powder X-ray diffraction. The beamline can measure powder X-ray diffraction data with the highest resolution in Japan, and has many achievements and know-how. The capillary was fixed with a compound along the groove of the sample folder. To avoid the preferred orientation in X-ray diffraction, the capillary was rotated during measurements. Automatic centering was used to correct the rotation axis of the capillary. The measurement wavelength was set to 0.328 Å. An Imaging Plate was used for the X-ray detector due to its high counting efficiency at the wavelength. A BAS-MS 200×400 mm Imaging Plate made by Fuji Film was used. The pixel size during the reading process was 50 × 50 μm. The  $2\theta$  axis of the diffractometer was set to  $2\theta = 0^\circ$  and  $30^\circ$ . The standard sample CeO<sub>2</sub> was measured from  $2\theta = 0$  to  $78^\circ$  at room temperature. The exposure time was 5 minutes. Wavelength calibration was performed with the lattice constant of CeO<sub>2</sub> which is 5.4111 Å.

Preliminary measurements of the aluminum and molybdenum were performed under the same experimental conditions as that of CeO<sub>2</sub>. The saturation times of the Imaging Plate for aluminum and molybdenum were calculated from the results of the preliminary measurements. The measurement time for the low angle side was set to 70% of the saturation time. The high angle side was set to 4 times that of the low angle side.

### 3.4.1 Reduction of fluorescence X-ray from molybdenum

A combination of copper and nickel foil with a thickness of 0.05 mm was placed in front of the Imaging Plate to reduce the X-ray fluorescence of molybdenum and to reduce X-ray fluorescence from the copper foil. The energy of the *K* absorption edge of the molybdenum is 20 keV. To identify the cause of the large background scattering in high energy X-ray powder diffraction and to select a combination of optimum metal foils, the synchrotron powder X-ray diffraction of molybdenum was preliminary performed at the SPring-8 BL02B2 beamline. The wavelength of the incident X-ray was 37.7 keV. The measurement time was 5 min. An Imaging Plane was used as the detector.

The black line in figure 3.7A represents the 1-D diffraction data of the preliminary measurements at room temperature. The horizontal axis represents the diffraction angle  $2\theta$  and the vertical axis the intensity. The peak intensity of 110 reflection and the background intensity are approximately 940,000 and 16,500 counts, respectively. The statistical fluctuation of the background intensity is 128 counts. Reflections from the (*h*00), (*hk*0), and (*hkl*) planes ( $h=k$ ,  $h=k=l$ ,  $h,k,l$  are multiples of 4) are systematically weak. For  $2\theta = 72.5^\circ$ ,  $\sin \theta / \lambda > 1.80 \text{ \AA}^{-1}$ , the intensities of the weak peaks were less than the statistical fluctuation.

In Figure 3.7A, the intensities of the black line indicate the independence from diffraction angle. The angle-independent background is a feature of X-ray fluorescence. The wavelengths of the incident X-ray and X-ray fluorescence of molybdenum were 0.328 and 0.711 Å, respectively. To remove the X-ray fluorescence intensity, a metal foil was placed in front of the detector.

The red line in Figure 3.7A shows the 1-D diffraction data at room temperature using 0.015 mm tantalum foil. The tantalum foil transmits 75% of the diffracted X-rays and 11% of the X-ray fluorescence. Compared with the case without tantalum foil, the background intensity was 1/5. Figures

3.7B and C show expanded views of  $2\theta = 70$  to  $76^\circ$  with and without tantalum foil, respectively. Owing to the X-ray fluorescence from the tantalum foil caused by the diffracted X-rays, additional peaks formed, indicated by the blue lines at C.

The purple line in figure 3.7A shows the 1-D diffraction data at room temperature using the combination of 0.05 mm copper and 0.05 mm nickel foils. To remove X-ray fluorescence from the copper foil, the nickel foil was placed between the copper foil and the detector. The copper foil transmits 77% of the diffracted X-rays and 12% of the X-ray fluorescence. The wavelength of the X-ray fluorescence of copper foil is 1.38 Å. The nickel foil transmits 79% of the diffracted X-rays, 12% of the X-ray fluorescence of molybdenum, and 0% of the X-ray fluorescence of copper foil. Figure 3.7D shows an expanded view of  $2\theta = 70$  to  $76^\circ$  with the combination of copper and nickel foils. There are no additional peaks from the copper foil. The fluctuation of the background intensity clearly decreased. A small diffraction peak at  $2\theta = 72.5^\circ$  is also recognized.

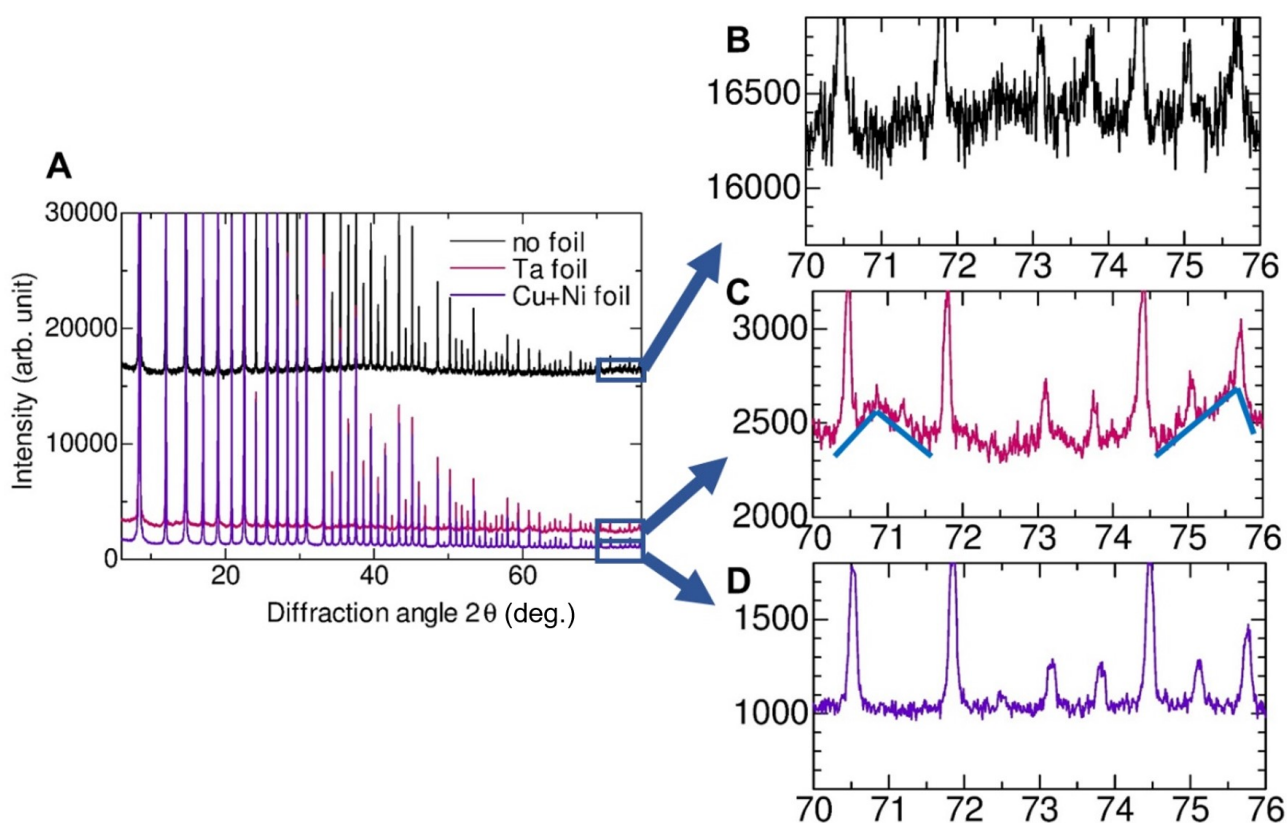


Figure 3.7 (a) 1-D diffraction data of molybdenum in the preliminary measurement at room temperature. (b-c) The expanded views of  $2\theta = 70$  to  $76^\circ$  (b) without metal foil and with (c) tantalum foil and (d) copper and nickel foils.

Figure 3.8 shows plots of the 1-D diffraction data of the preliminary synchrotron powder X-ray diffraction in molybdenum for each combination of metal foils. The horizontal axis represents the diffraction angle  $2\theta$  and the vertical axis the intensity. The black line shows the measurement data without the metal foil. The data have approximately 22,000 counts of background intensity. Figure 3.8 (bottom) shows an expanded view of the 1-D diffraction data with metal foils. Red, green, and orange

represent the copper, nickel, and tantalum foils, respectively. Using a single metal foil, the background intensity was less than 1/5. The intensity of the X-ray fluorescence from the tantalum foil can be clearly observed. Blue, pink, and purple show the results of the copper + tantalum, nickel + tantalum, and copper + nickel combined foils, respectively. The measurement data with these three combinations are similar. To avoid the use of tantalum foil with a high intensity of X-ray fluorescence, the combination of copper + nickel foil was employed for the synchrotron powder X-ray diffraction measurement of molybdenum.

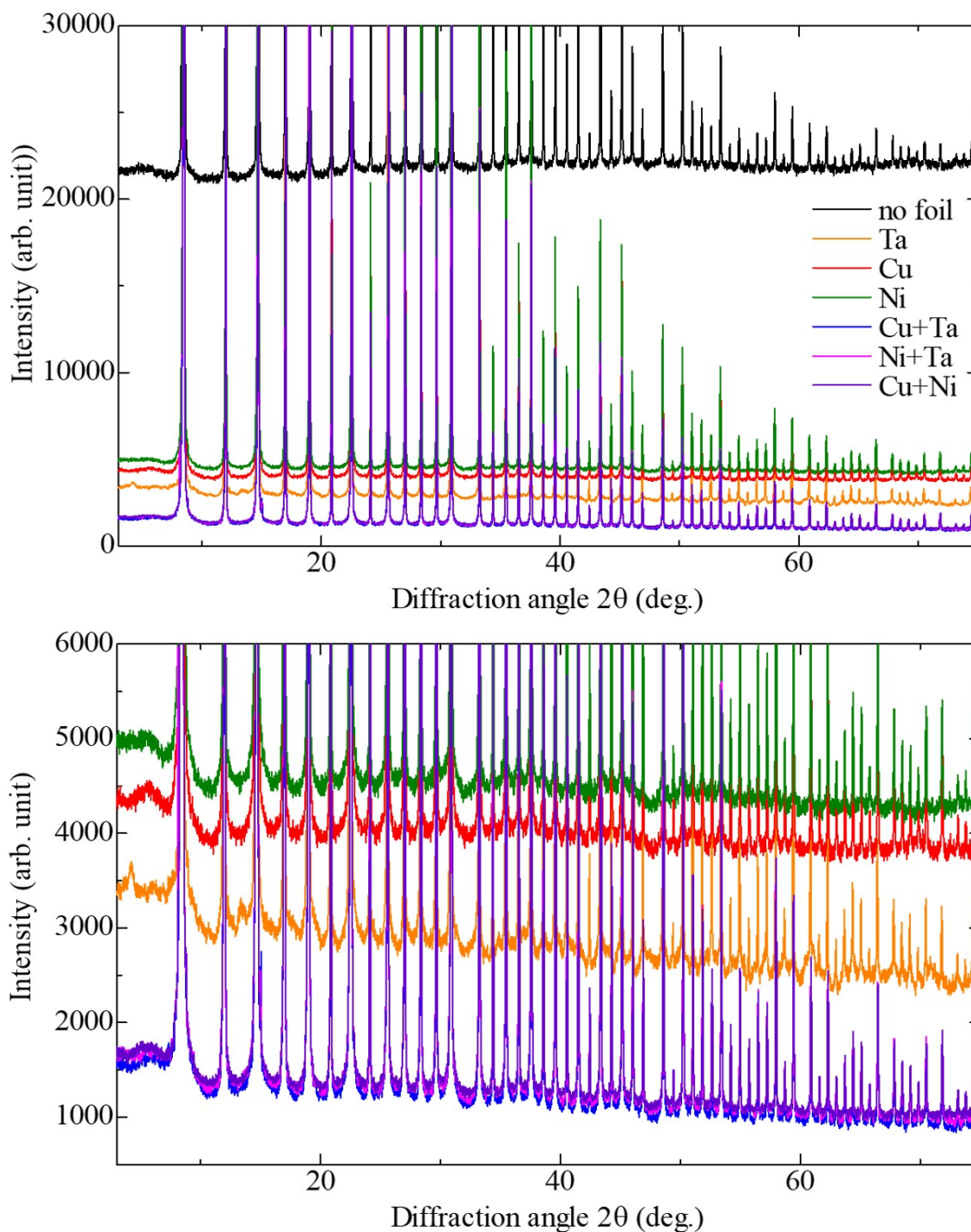


Figure 3.8 Plots of 1-dimensional diffraction data of the preliminary synchrotron powder X-ray diffraction in molybdenum for each combination of metal foils.

### 3.4.2 Experimental conditions of aluminum and molybdenum

Table 3.1 shows the experimental conditions of the aluminum and molybdenum. The columns from the left to right show the wavelength of the incident X-ray, measurement time, measurement temperature, slit width, and the initial diffraction angle  $2\theta$ . In molybdenum, the measurements were carried out using the combination of copper and nickel foil. There are two sets of measurement times for aluminum. The first is 30 min in the low angle side and 120 min in the high angle side. The second is 27 min in the low angle side and 108 min in the high angle side. The fluctuation of the measurement time is due to the fluctuation of the beam intensity at the measurement wavelength, depending on the difference of the measurement date and time. In molybdenum, 20 min in the low angle side and 80 min in the high angle side were employed. The measurement temperatures were 30, 100, 200, 300, 400, 500, and 600 K. At 30 K, a He gas flow low-temperature device was used. At the other temperatures, a N gas flow device was used. The  $2\theta$  axis of the diffractometer was  $2\theta = 0^\circ$  and  $30^\circ$  for 30, 200, 300, 400, 500, and 600 K. In molybdenum at 100 K, the axis was  $2\theta = 0^\circ, 30^\circ$ , and  $45^\circ$ .

Table 3.1 Experimental conditions of aluminum and molybdenum.

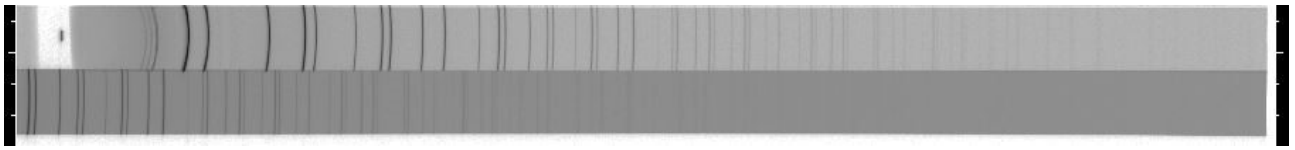
Sample	Wavelength ( $\text{\AA}$ )	Measurement time (min)	Temperature (K)	Slit width (mm)	Diffraction angle (deg.)
Al	0.328	30 / 120	100, 200, 300	30	0 / 30
Al	0.328	27 / 108	30, 400, 500, 600	20	0 / 30
Mo	0.328	20 / 80	30, 200, 300, 400, 500, 600	20	0 / 30
Mo	0.328	20 / 80	100	20	0 / 30 / 45

## 3.5 Diffraction data

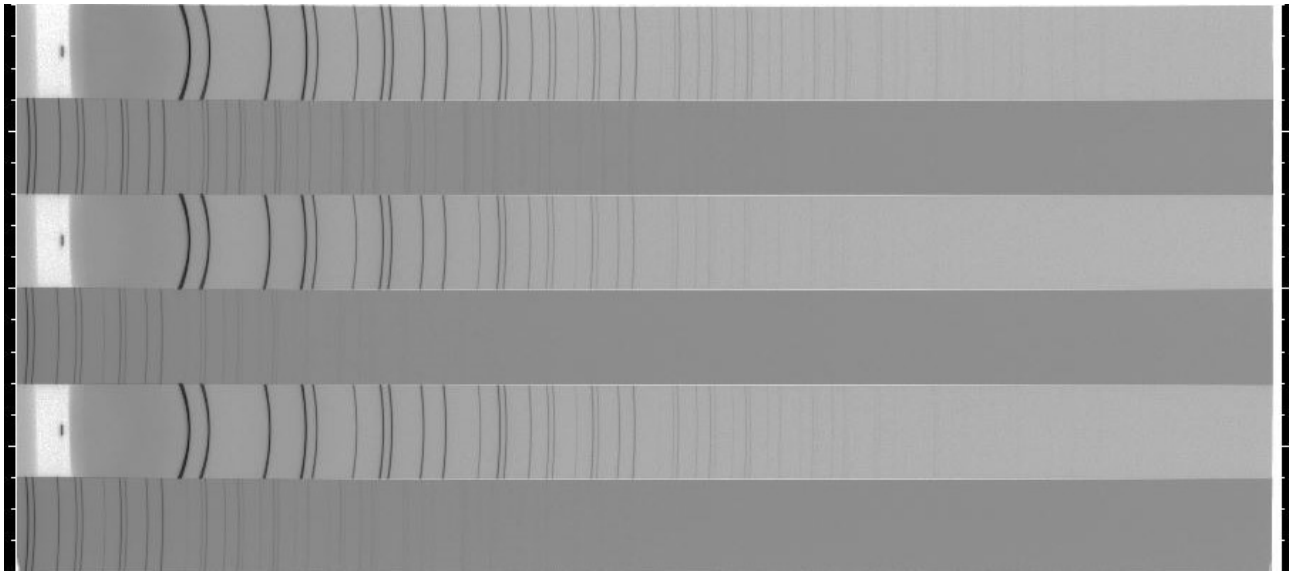
### 3.5.1 2-dimensional diffraction data of aluminum and molybdenum

Figure 3.9 shows the 2-D diffraction data of the aluminum measured at (a) 30, (b) 100, 200, 300, (c)400, and (d) 500 and 600 K. The data were plotted by ipview.exe. The pixel size was read at  $50 \mu\text{m}$ . The sensitivity was 1000. The left side in the figures shows the low diffraction angle and the right side shows the high diffraction angle. The X-ray irradiation intensity is represented by a black gradation. The white region is not irradiated with the X-ray. The short black line in the white region on the left side shows the direct beam of the incident X-ray. The direct beam is a transmitted X-ray that was not diffracted by the sample. One measurement is recorded as one rectangular band. The vertical width of the band is the slit width. The left side of low angle measurement is the diffraction angle of  $2\theta = 0^\circ$ . The left side of the high angle measurement is the diffraction angle of  $2\theta = 30^\circ$ . The upper band at each measurement temperature shows the low angle measurement. The lower side shows the high angle measurement. The upper, middle, and bottom sets in (b) are 100, 300, and 200 K, respectively. The upper and bottom sets in (d) are 500 and 600 K, respectively. The vertical black curves for each band indicate a part of the Debye-Scherrer ring. There were no black spots present on the Debye-Scherrer rings due to coarse particles. No influence on the 2-D diffraction data owing to a

defect of the Imaging Plate was found.



(a) 2-dimensional diffraction data of aluminum at 30 K.



(b) 2-dimensional diffraction data of aluminum at 100,200, and 300 K.



(c) 2-dimensional diffraction data of aluminum at 400 K.

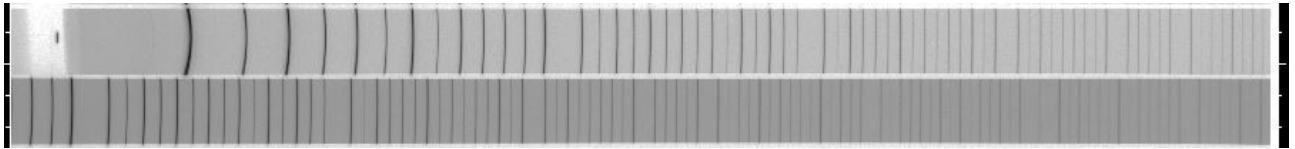


(d) 2-dimensional diffraction data of aluminum at 500 and 600 K.

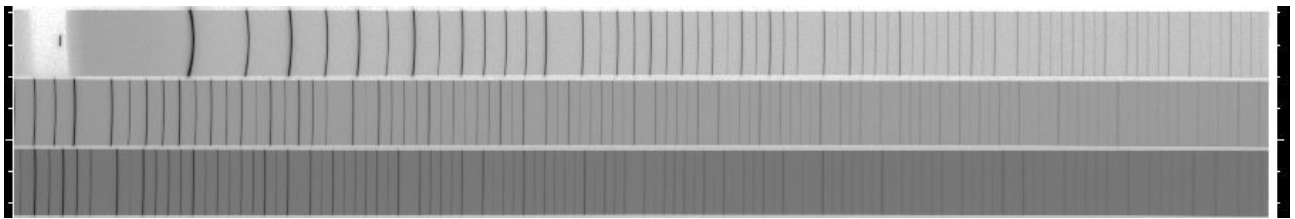
Figure 3.9 2-dimensional diffraction data of aluminum measured at (a) 30, (b) 100, 200, 300, (c) 400, (d) 500 and 600 K.

Figure 3.10 shows the 2-dimensional diffraction data of molybdenum measured at (a) 30, (b) 100, (c)200 and 300, (d)400 and 500, and (e) 600 K. The geometry is same as the aluminum. The upper and bottom sets in (c) are 200 and 300 K, respectively. The upper and bottom sets in (d) are 500 and

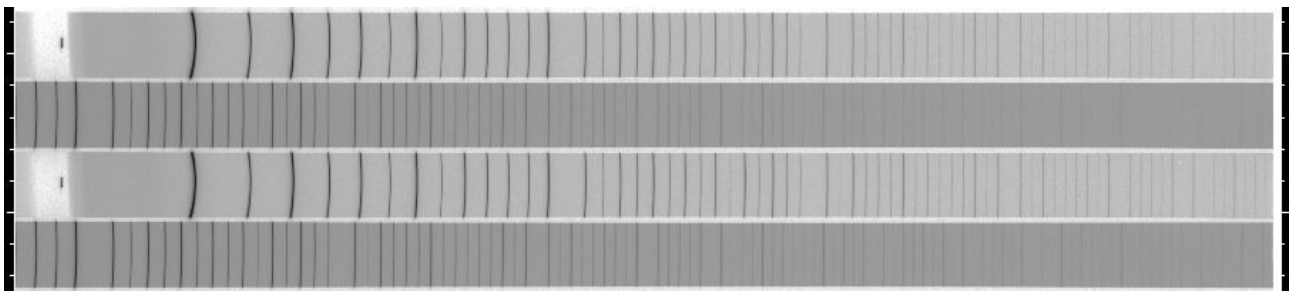
400 K, respectively. The data of 100 K has the three diffraction angles. The upper, middle, and bottom rectangular are  $2\theta = 0^\circ$ ,  $30^\circ$ , and  $45^\circ$ , respectively. As with the results of aluminum, there were no black spot present on the Debye-Scherrer rings, and no influence on the 2-D diffraction data owing to a defect of the Imaging Plate.



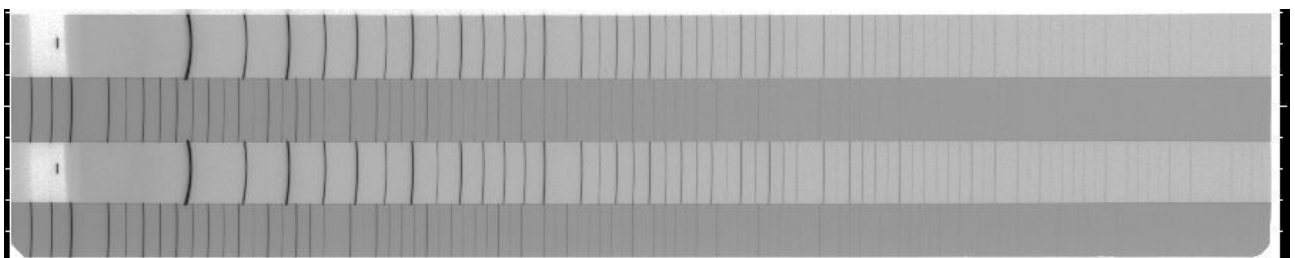
(a) 2-dimensional diffraction data of molybdenum at 30 K.



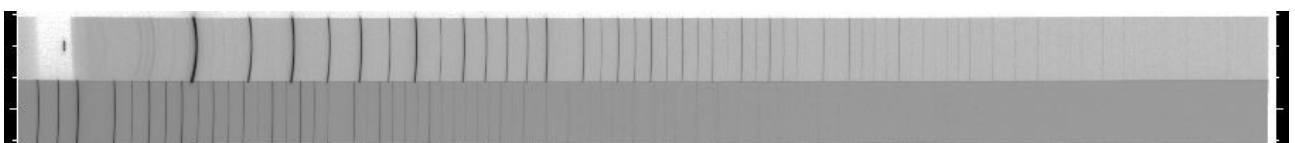
(b) 2-dimensional diffraction data of molybdenum at 100 K.



(c) 2-dimensional diffraction data of molybdenum at 200 and 300 K.



(d) 2-dimensional diffraction data of molybdenum at 400 and 500 K.

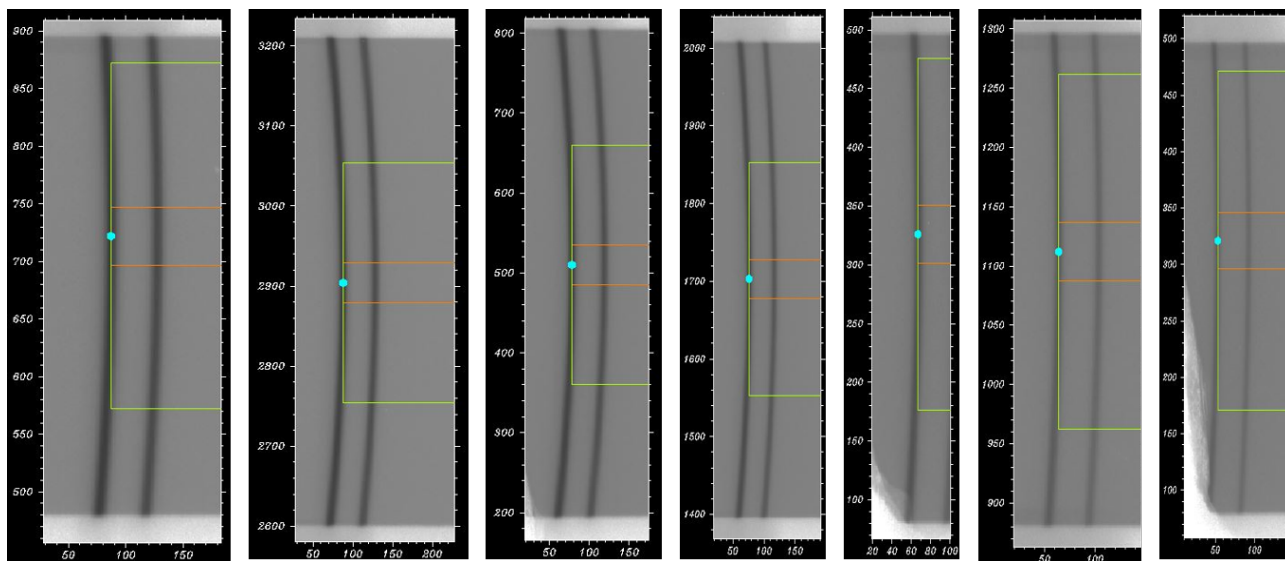


(e) 2-dimensional diffraction data of molybdenum at 600 K.

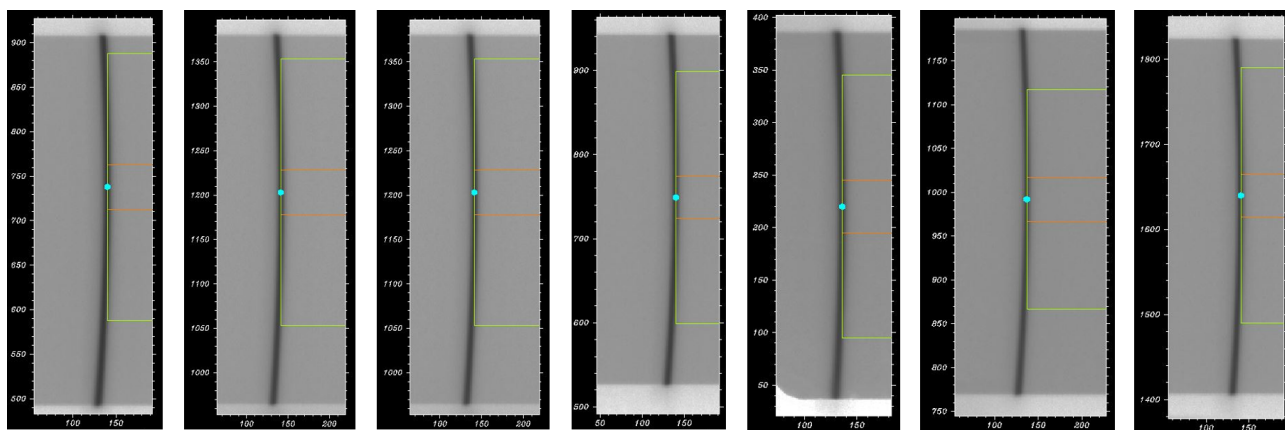
Figure 3.10 2-dimensional diffraction data of molybdenum measured at (a) 30, (b) 100, (c) 200 and 300, (d) 400 and 500 and (e) 600 K.

### 3.5.2 Integration of 2-dimensional diffraction data to 1-dimensional diffraction data

Figure 3.11 shows the origins of integration of the high angle measurement from the 2-D diffraction data to the 1-D diffraction data of the (a) aluminum and (b) molybdenum. The 2-D diffraction data were integrated to the 1-D diffraction data using `ipview.exe`. The integration widths in one band were 51 px and 251 px. The red and green lines show the integration range of 51 and 251 px, respectively. An “Automatic” mode in dual powder data tab was used to determine the origin of integration in the low angle side. For the high angle side, “manual” mode in dual powder data tab was used.



(a) The origins of integration for aluminum.



(b) The origins of integration for molybdenum.

Figure 3.11 The origins of integration of high angle measurement from 2-dimensional diffraction data to 1-dimensional diffraction data of (a) aluminum and (b) molybdenum.

Figure 3.12 shows the method of determining the origin of the integration region in the 2-D diffraction data of the high angle side. The integration regions are represented by the red line of 51 px and green line of 251 px. The yellow line is parallel to the vertical axis of the rectangular band of

integration range. Aligning the left edge of the measured Debye-Scherrer ring with the yellow line; if the horizontal positions of the contact point between the yellow line and the top and bottom of the Debye-Scherrer ring are different, the horizontal position of the yellow line is set to the right side of the contact point. In Figure 3.12, the upper side of the contact point between the Debye-Scherrer ring and the yellow line is further right than the bottom side. The red double-headed arrow indicates the vertical width of 40 px. The blue double arrow indicates a width of 520 to 900 px. The center position in the blue double arrow is taken as the vertical axis center of the integral width. The center position is 710 px in the vertical axis. A similar procedure was used for the other integration of the 2-D diffraction data.

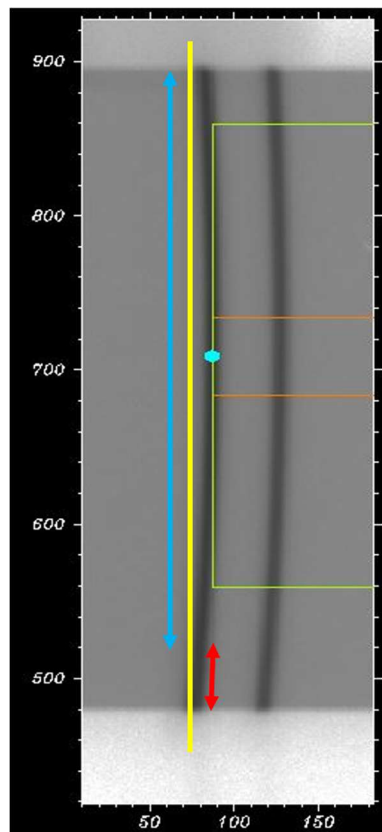
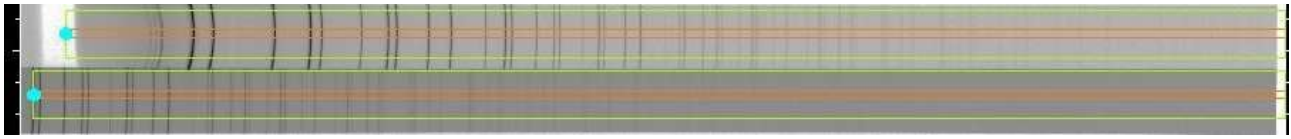


Figure 3.12 The method of determining origin of integration region in 2-dimensional diffraction data of high angle side.

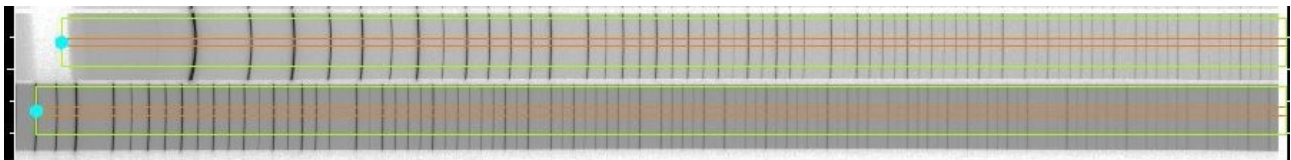
Figure 3.13 shows the integration regions in the integration procedures of the aluminum and molybdenum at 30 K. A band surrounded by the red line shows an integration width of 51 px. The green line shows an integration width of 251 px. The geometry of the figures is the same as 3.6.1. The vertical width of the measured 2-D diffraction data is sufficiently larger than the integration width of 251 px.

Figure 3.14 shows an expanded view of the boundary region of the rectangles between the lower measurement angle and higher angle in the aluminum and molybdenum data at 30 K data. This is a confirmation whether the 251 pixel region does not overlap to a part of Debye-Scherrer ring in the rectangle of the lower measurement angle. The green lines with an integration width of 251 px are in

each band. The high-intensity Debye-Scherrer ring at a low angle slightly protrudes from the band area. These protruding Debye-Scherrer rings are not in the integrated region of 251px.

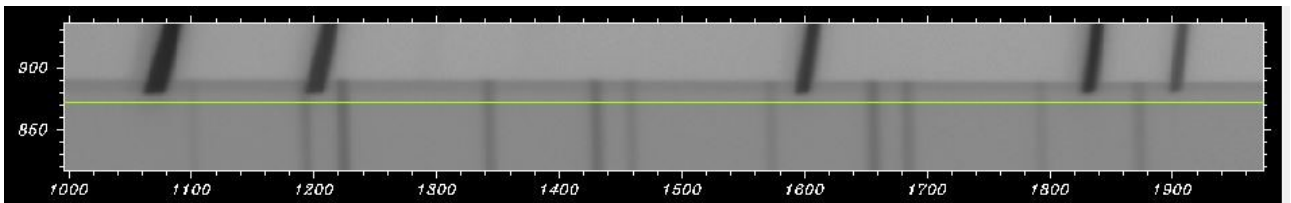


(a) Integration region of aluminum at 30 K.

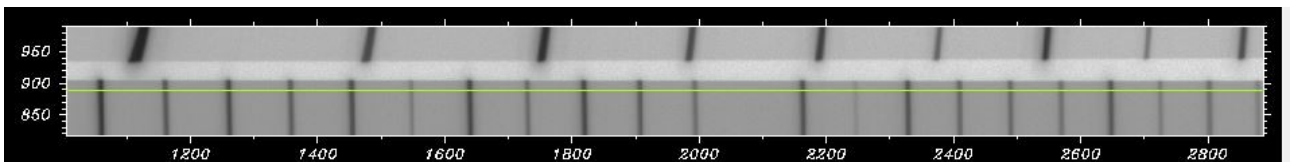


(b) Integration region of molybdenum at 30 K.

Figure 3.13 shows integration region in the integration procedures of (a) aluminum and (b) molybdenum at 30 K.



(a) The boundary region of rectangles in aluminum at 30 K



(b) The boundary region of rectangles in molybdenum at 30 K

Figure 3.14 An expanded view of the boundary region of rectangles between lower measurement angle and higher angle in (a) aluminum and (b) molybdenum at 30 K data.

### 3.5.3 1-dimensional diffraction data of aluminum and molybdenum

Figure 3.15 shows the 1-D diffraction data of aluminum at 30, 100, 200, 300, 400, 500, and 600 K of the aluminum. The vertical axis is the intensity in the log scale and the horizontal axis is the diffraction angle  $2\theta$ . This is the low angle measurement data with 51 pixels. As the measurement temperature increases, the number of observable diffraction peaks decreases. At 30 K, there were diffraction peaks of ice attached to the surface of the capillary around  $2\theta = 10^\circ$ . The diffraction peaks of ice do not overlap the diffraction peaks of aluminum. Between 100 and 600 K, there were no second-

phase diffraction peaks. At all temperatures, the intensity of the diffraction peaks of aluminum oxide and other phases is less than the background statistical error of  $\sim 70$  counts. The index of the strongest diffraction peak of aluminum is  $hkl = 111$ , which is 1.25 million counts. The ratio of the intensity of the 111 diffraction peak to the statistical error of the background is 1:18,000. Aluminum oxide is less than 0.01%w in the measurement sample.

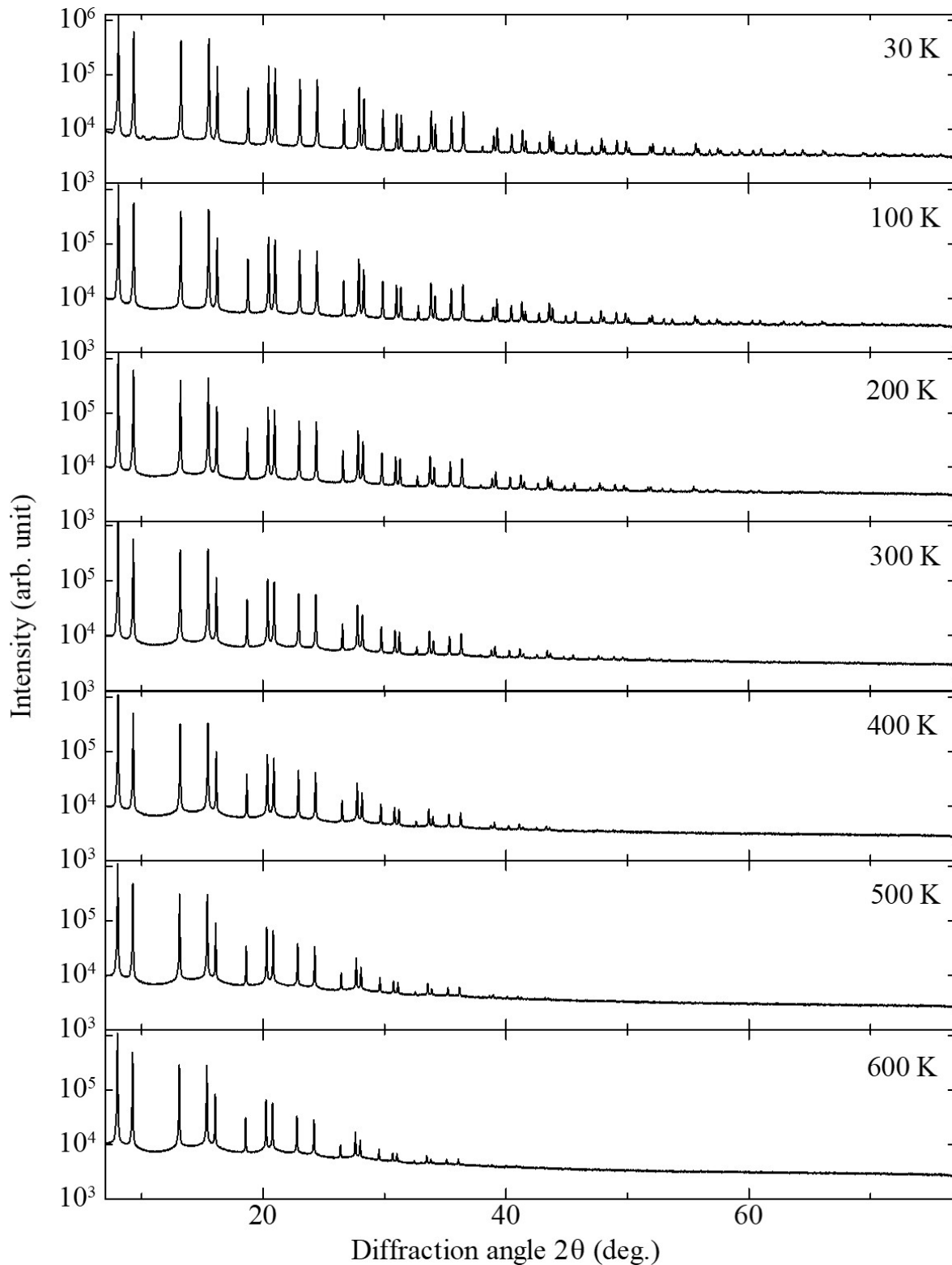


Figure 3.15 1-dimensional diffraction data of aluminum at 30, 100, 200, 300, 400, 500, and 600 K.

Figure 3.16 shows changes in the diffraction peak due to the measurement temperature at 30, 100, 200, and 300 K. The 1-D diffraction data of the low angle side at 30, 100, 200, and 300 K with an integration width of 251 px were superimposed. The position of the strongest peak of 100, 200, and 300 K was made to coincide with the position of 30 K. The black line represents 30 K, the blue line 100 K, the green line 200 K, and the orange line 300 K. The horizontal axis shows the diffraction angle  $2\theta$ , while the vertical axis shows the intensity. The correction amount on the horizontal axis is  $+0.005^\circ$  at 100 K,  $+0.02^\circ$  at 200 K and  $+0.03^\circ$  at 300 K. These intensities are not normalized. At the diffraction peaks at  $2\theta = 13.2^\circ$ , a difference in the intensity due to temperature and a shift due to the thermal expansion of the lattice constant can be visually observed. The 300 K diffraction peaks can be seen up to  $2\theta = 60.8^\circ$ . The 200 K diffraction peaks can be seen up to  $2\theta = 66.5^\circ$ .

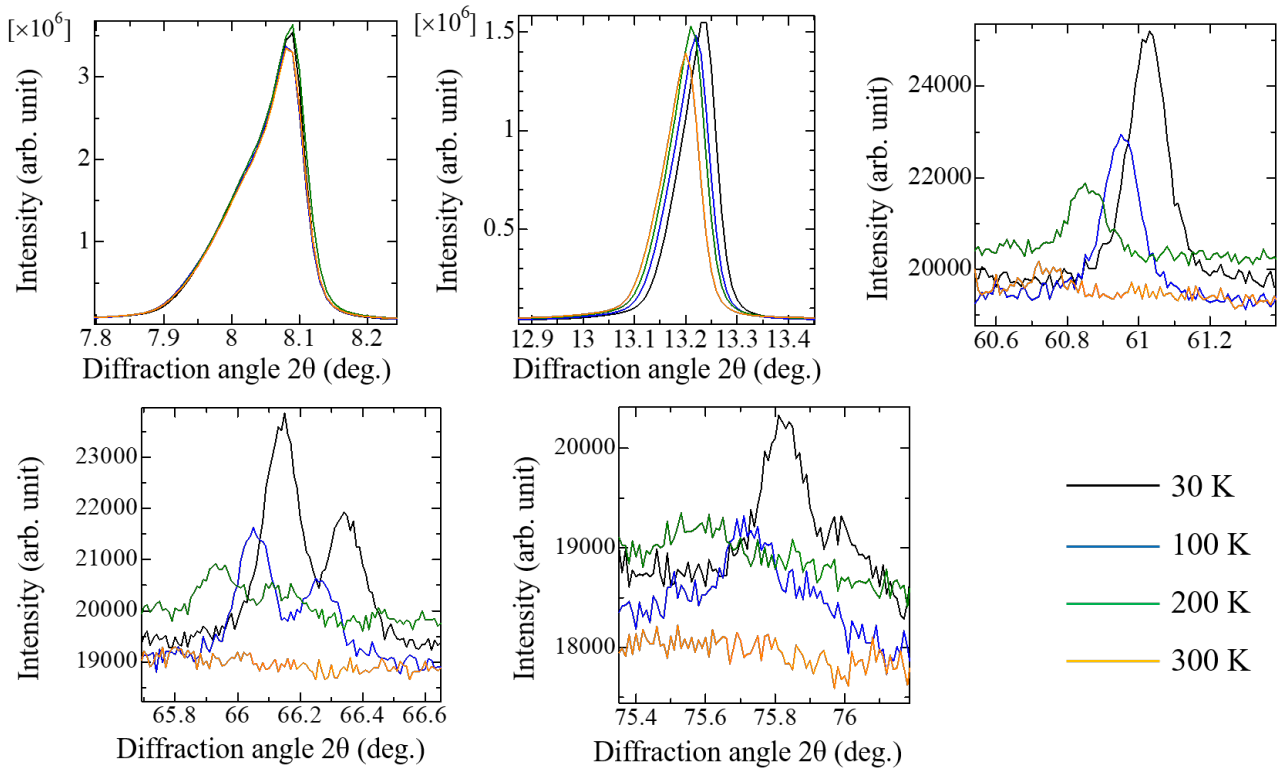


Figure 3.16 Changes in the diffraction peak due to measurement temperature at 30, 100, 200, and 300 K.

Figure 3.17 shows the superposition of the strongest peaks and temperature change of diffraction peaks on the high angle side. The black line represents 30 K, the blue line 100 K, the green line 200 K, and the orange line 300 K. The horizontal axis shows the diffraction angle  $2\theta$ , and the vertical axis shows the intensity. The correction amount on the horizontal axis is  $+27.923^\circ$  at 30 K,  $+27.92^\circ$  at 100 K,  $+27.93^\circ$  at 200 K and  $+27.931^\circ$  at 300 K. The diffraction peaks of 100 K can be seen up to  $2\theta = 86.5^\circ$ . The diffraction peaks at 300 K can be seen up to  $2\theta = 103.5^\circ$ . In total, 217 diffraction peaks can be observed in the low angle and high angle 1-D diffraction data at 30 K.

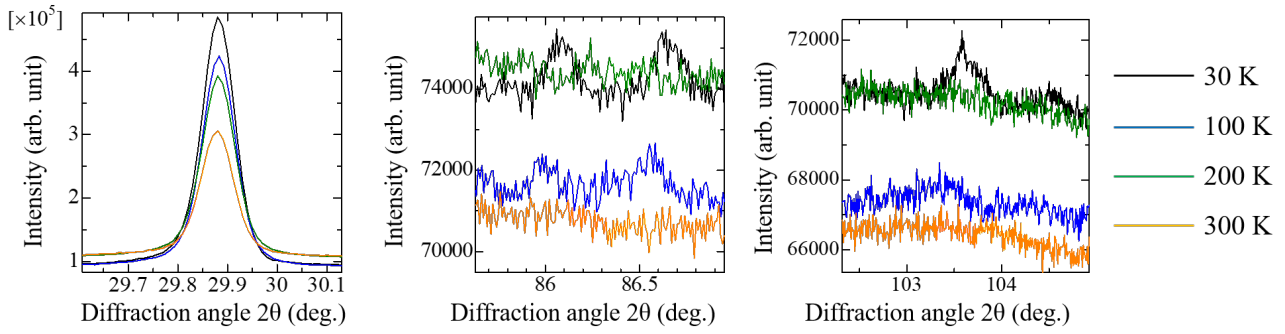
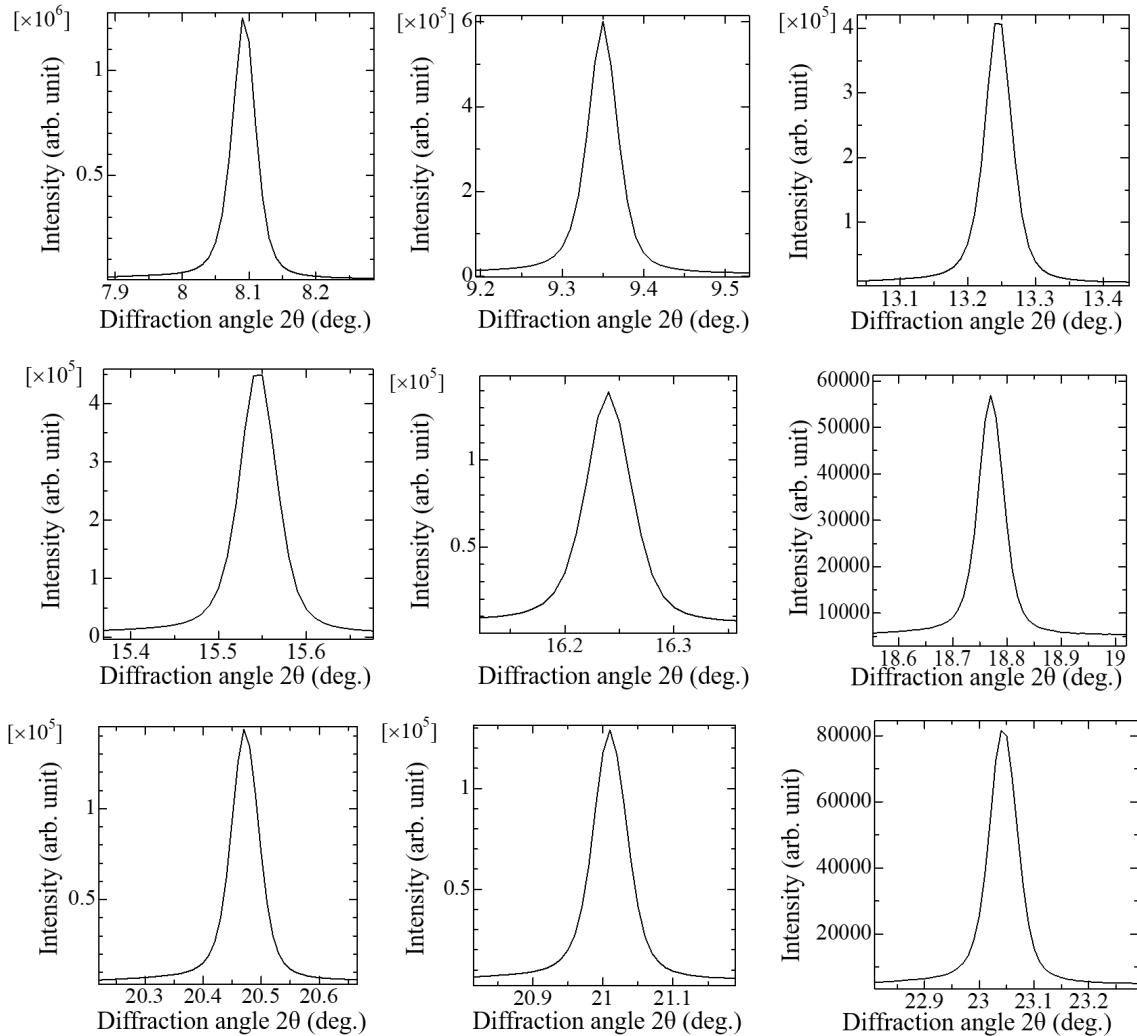
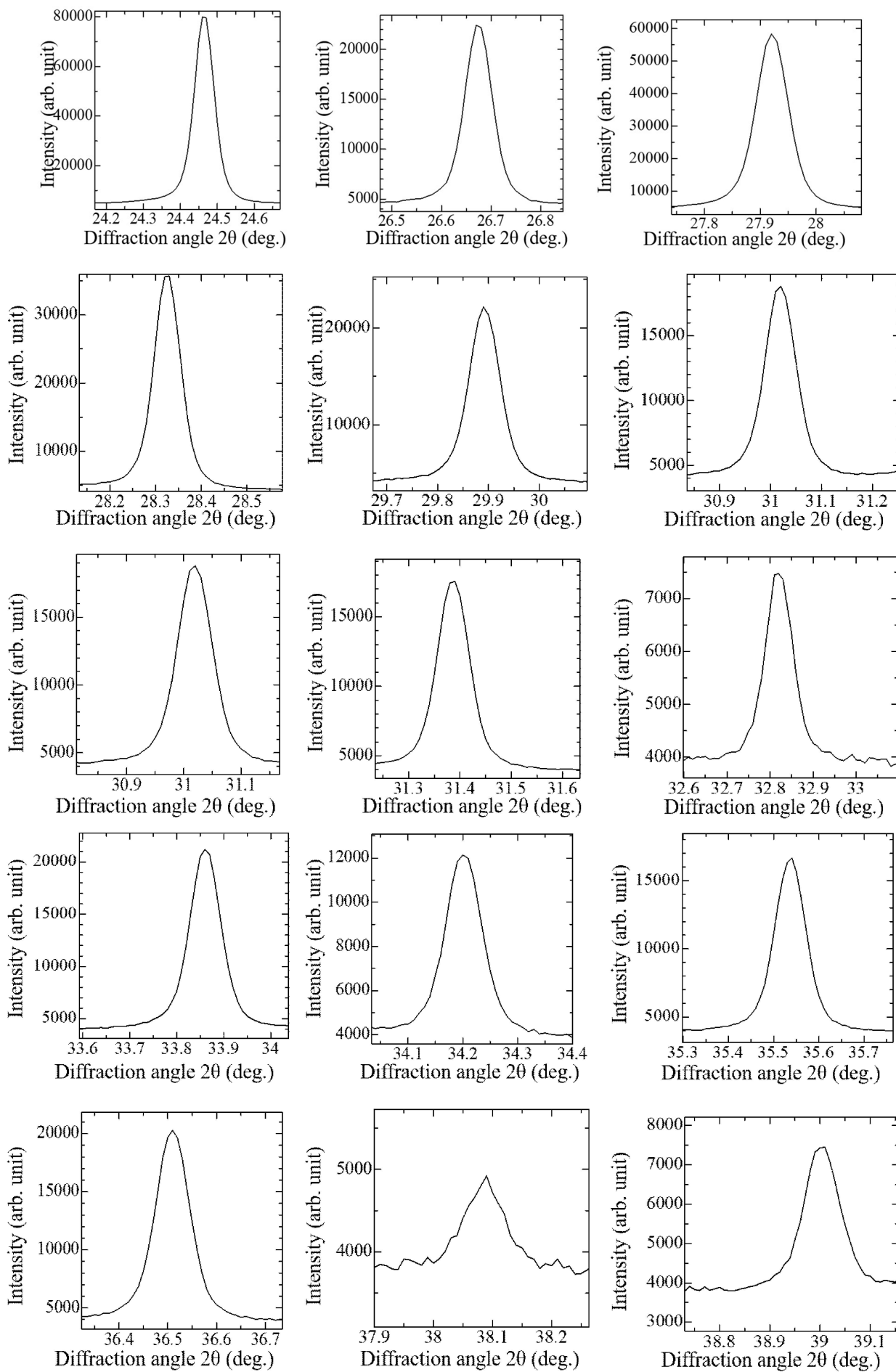
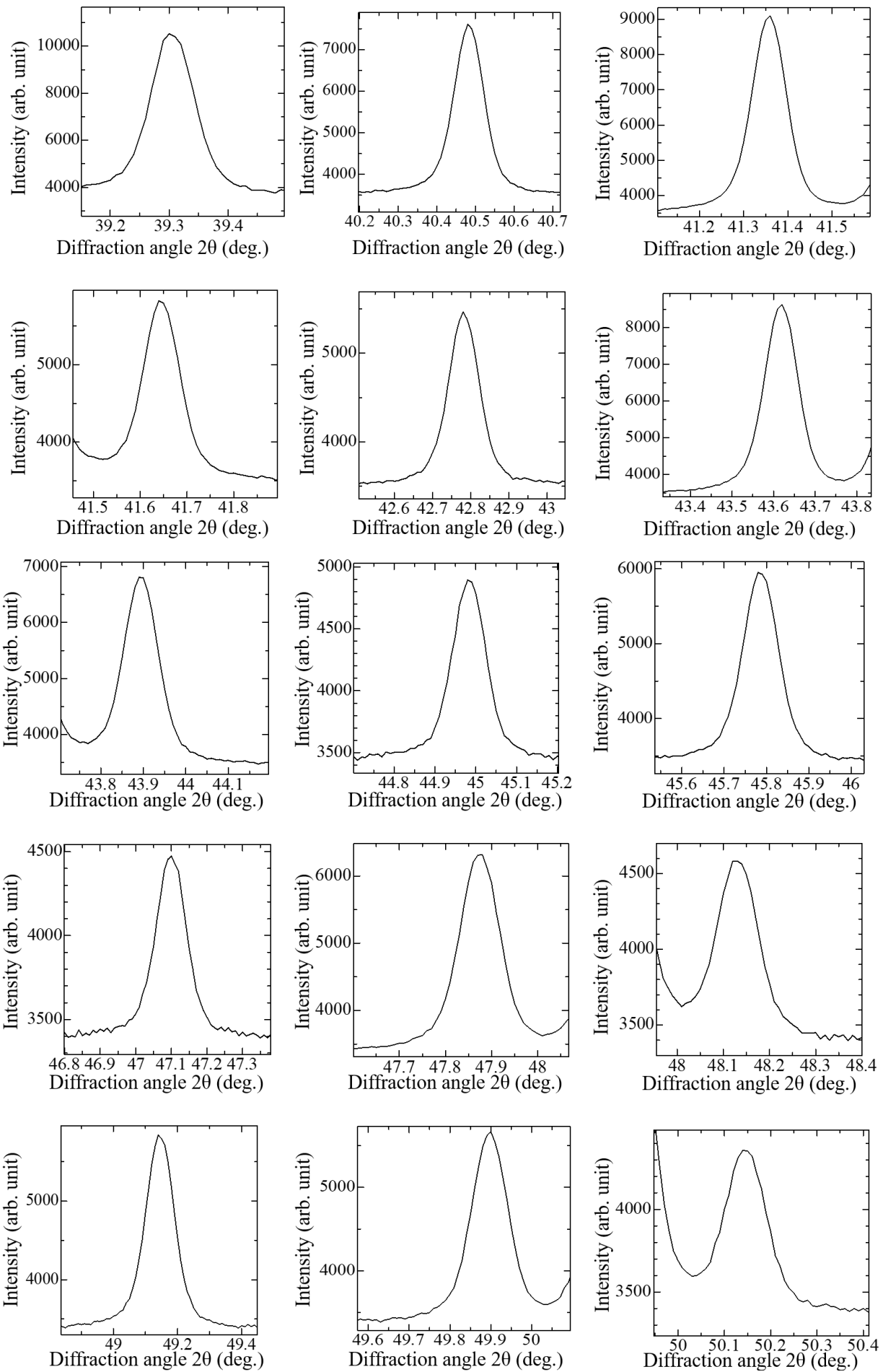


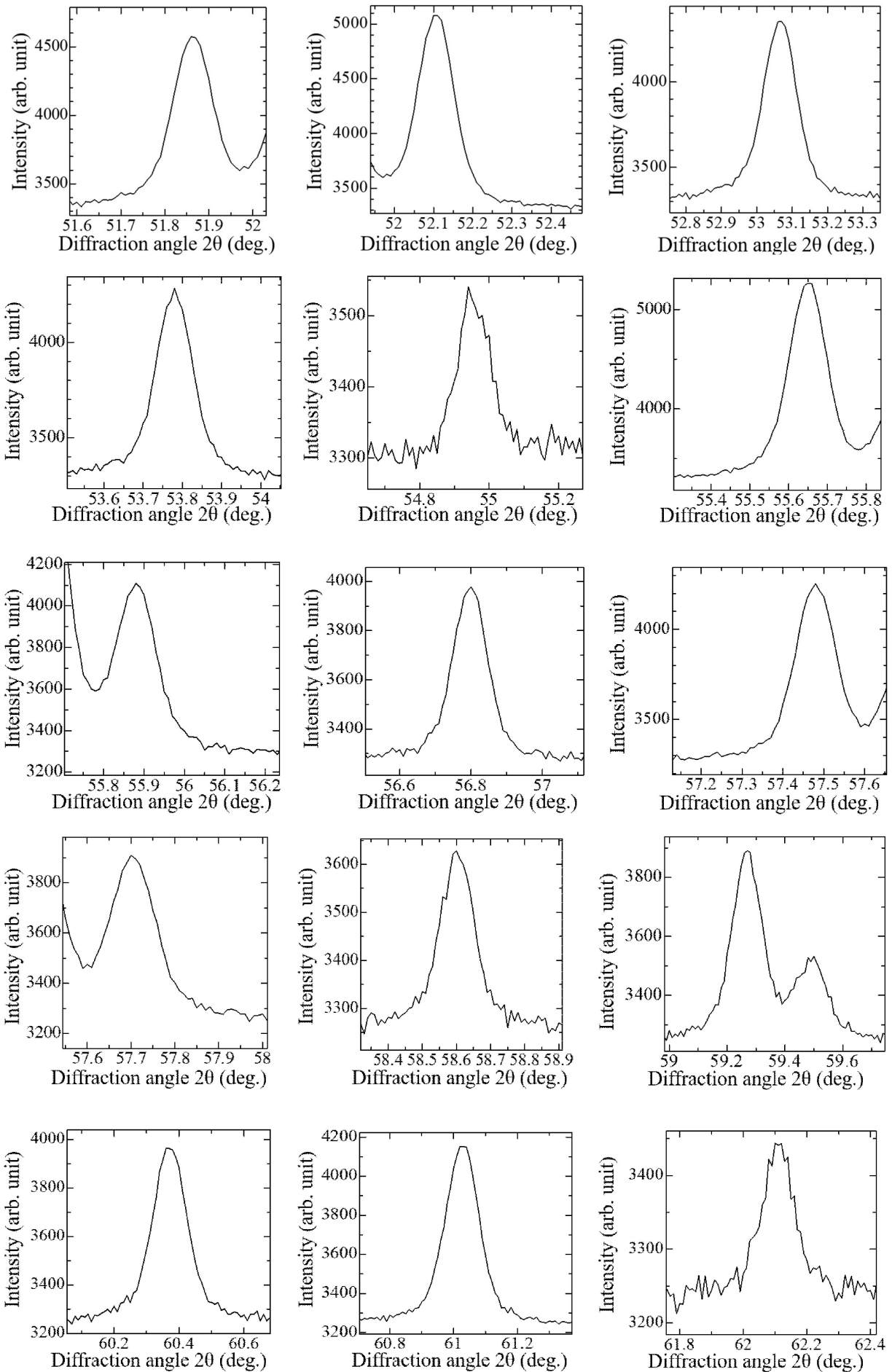
Figure 3.17 The superposition of the strongest peaks and temperature change of diffraction peaks on the high angle side.

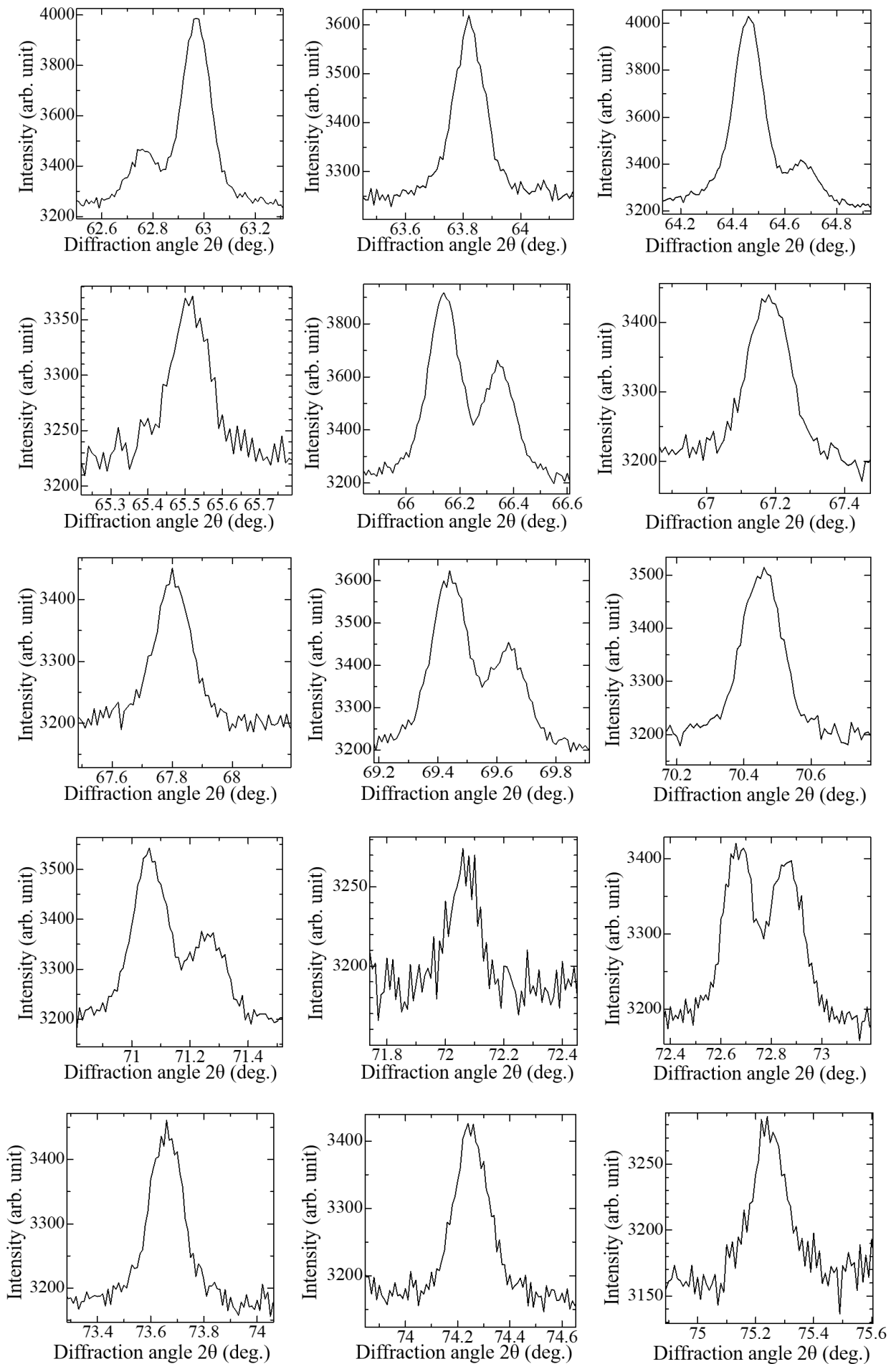
Figure 3.18 shows the shapes of all the diffraction peaks in the 1-D diffraction data of 30 K of the aluminum with 51 px for the low angle side and 251 px for the high angle side. The diffraction peaks from the low and high angle data are  $2\theta = 7\sim 40^\circ$  and  $2\theta = 40\sim 107^\circ$ , respectively. This figure is necessary to confirm a broadening and splitting of the diffraction peaks. As a result, there were no broadening and splitting of the diffraction peaks in aluminum. This means an amount less than the detection limit in the synchrotron powder X-ray diffraction of intrinsic strain and stacking fault.

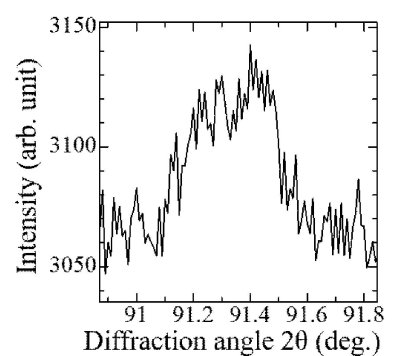
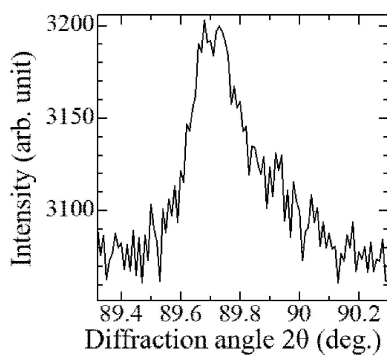
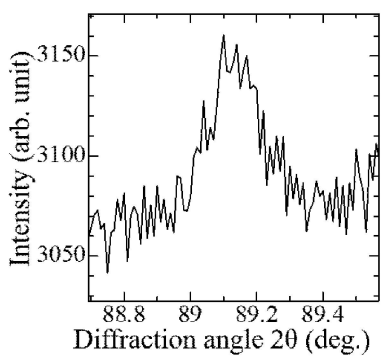
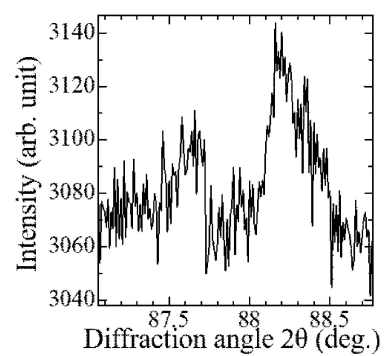
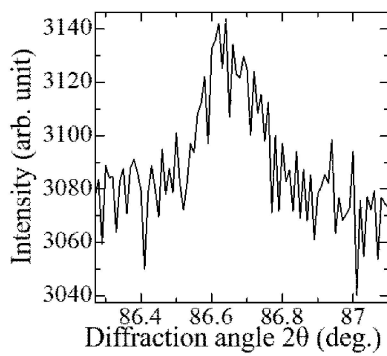
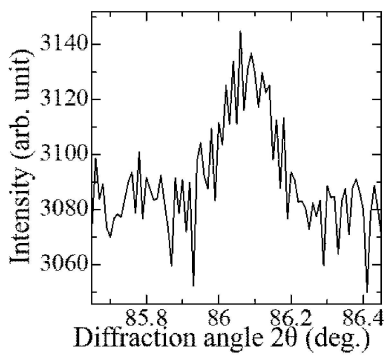
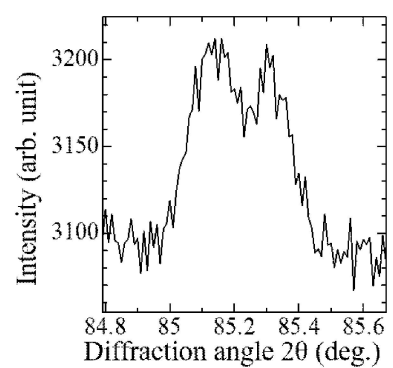
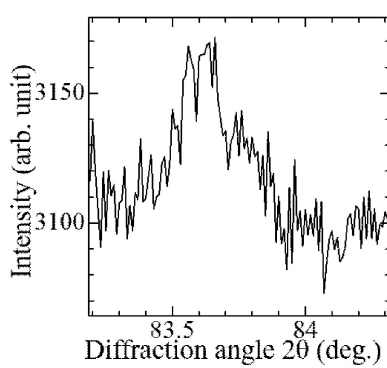
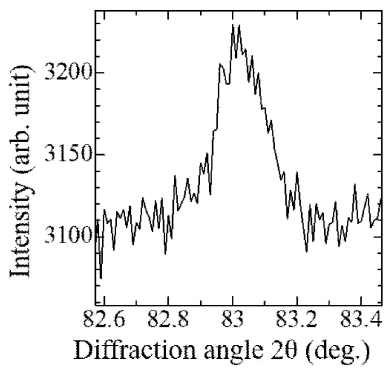
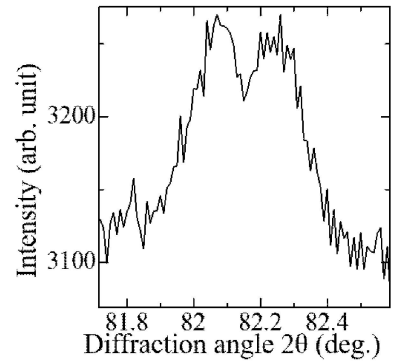
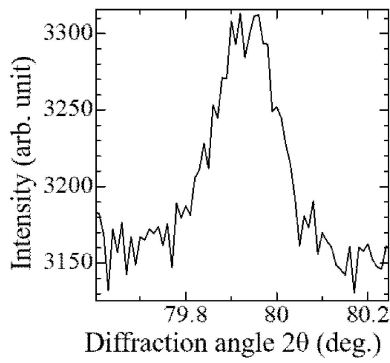
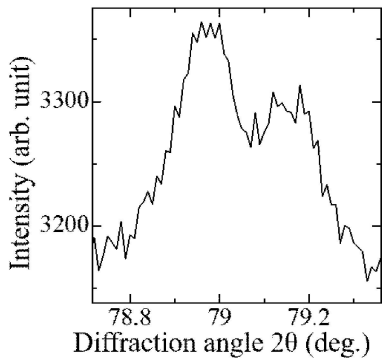
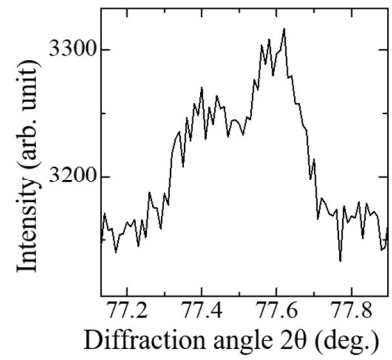
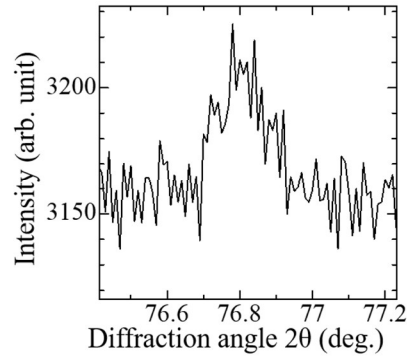
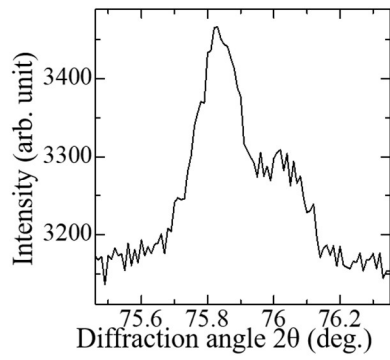












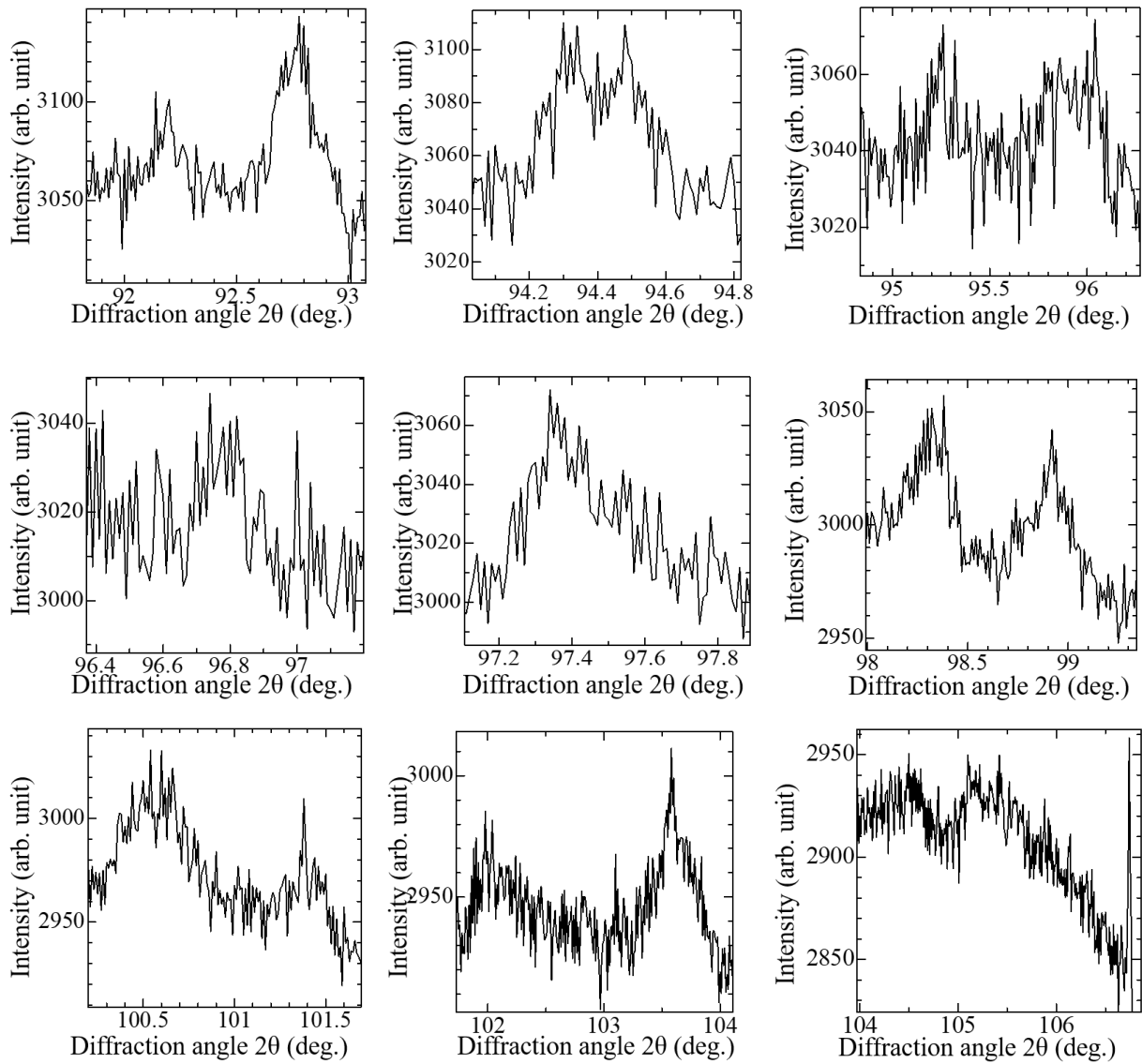


Figure 3.18 The shapes of all diffraction peaks in 1-dimensional diffraction data of aluminum at 30 K with 51 pixels for low angle side and 251 pixels for high angle side.

Figure 3.19 shows the 1-D diffraction data of 30, 100, 200, 300, 400, 500, and 600 K of molybdenum. The vertical axis represents the intensity in the log scale and the horizontal axis the diffraction angle  $2\theta$ . This is the superposition of four 1-D diffraction data. These are the data of 51 px and 251 px on the low angle side and 51 px and 251 px on the high angle side. As the measurement temperature increases, the number of observable diffraction peaks decreases. The 30 K data includes the diffraction peaks of ice attached to the surface of the capillary. A diffraction peak of ice overlaps with the 110 diffraction peak of molybdenum. The ratio of the intensity of the 110 diffraction peak to the diffraction peak of ice is 1:3800. The intensity of the diffraction peak of ice is less than 0.01%. The 600 K data have additional diffraction peaks from the second phase. The diffraction pattern matched those of molybdenum oxide  $\text{MoO}_3$ . No second phase was detected in the data at 100, 200, 300, 400, and 500 K. The intensity of the diffraction peaks of molybdenum oxide is less than the background statistical error of  $\sim 60$  counts. Molybdenum oxide comprises less than 0.01%w in the measurement sample.

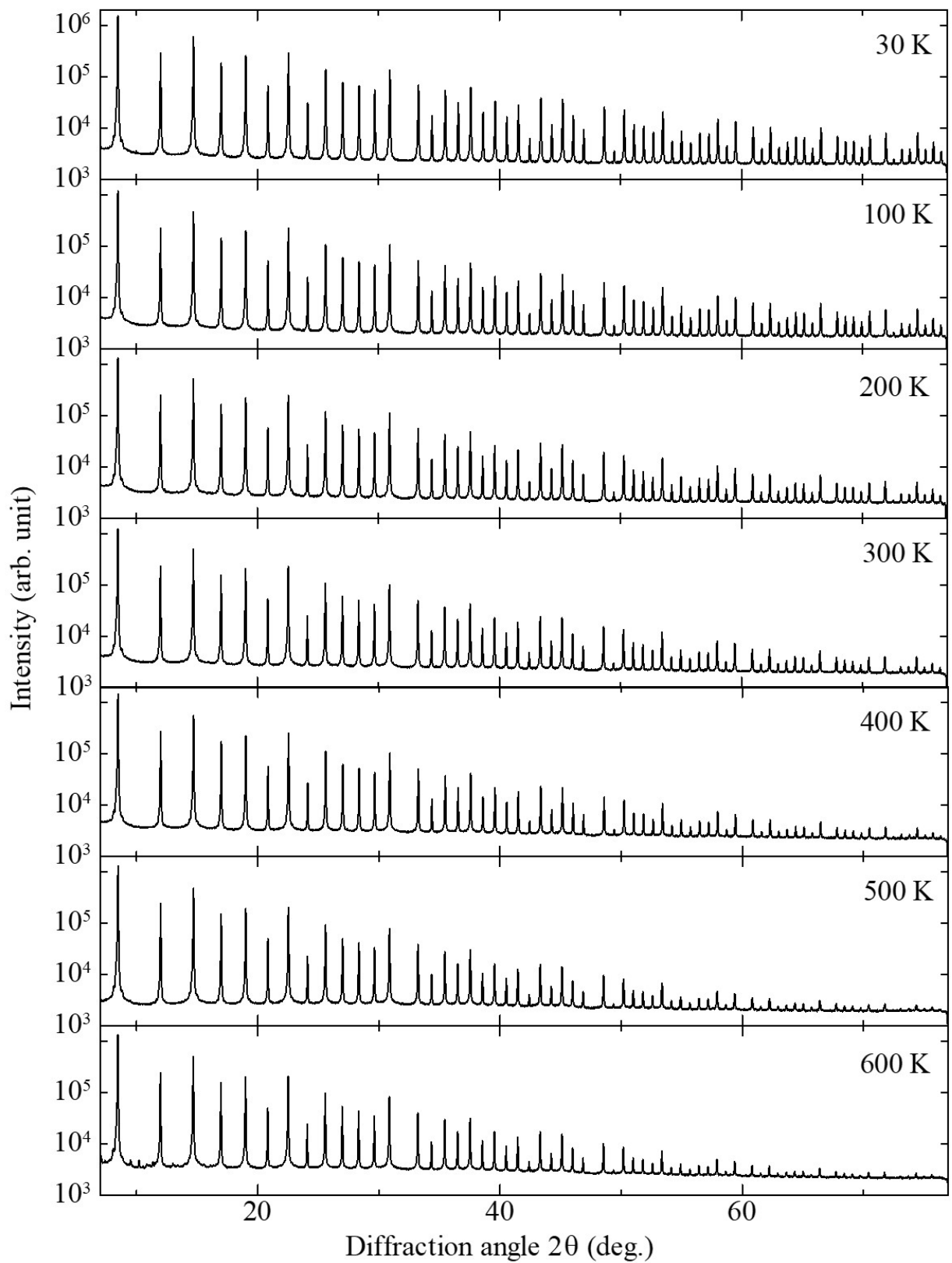


Figure 3.19 1-dimensional diffraction data of 30, 100, 200, 300, 400, 500, and 600 K of molybdenum.

### 3.6 Summary

The synchrotron powder X-ray diffraction measurement of aluminum and molybdenum were performed at SPring-8 BL02B2. The powders of aluminum and molybdenum were sealed in the Lindemann glass capillary in the glovebox under Ar gas. The sample temperatures were controlled at 30, 100, 200, 300, 400, 500, and 600 K using the gas flow devices. The 217 and 193 diffraction peaks were successfully observed for the aluminum and molybdenum at 30 K data. The resolutions  $d$  and reciprocal resolutions  $\sin \theta / \lambda$  of the measurement data at 30 K are 0.22 Å and 2.31 Å<sup>-1</sup> for aluminum and 0.22 Å and 2.32 Å<sup>-1</sup> for molybdenum, respectively. The counts of the most intense diffraction peaks of aluminum and molybdenum were over 1.2 million counts. The error of less than 0.34% in the diffraction intensity was achieved with the 7 diffraction peaks for aluminum and the 8 for molybdenum. Oxides, internal strain, and stacking fault in the aluminum and molybdenum did not detect in the measurement. Both the aluminum and molybdenum samples include less than 0.01%w oxides. The diffraction peaks of aluminum and ice were not overlapped. The intensity of the diffraction peak of ice was less than 0.01% to the 110 diffraction peak of molybdenum.

# Chapter 4 Principles and Analysis

## 4.1 Introduction

This chapter explains the analysis method and sets of structure factors used in this research. The fundamental processing in the analysis are (1) sum up of the counts of diffraction peaks in 1-D diffraction data, and (2) division of integrated Bragg intensity of completely overlapped diffraction peaks. The process of (1) can be determined by counting the number of counts above the background scattering. The background was determined in Rietveld refinement. The intensity of thermal diffuse scattering was estimated for accurate determination of background scattering. The integrated intensity is proportional to square of the absolute value of the structure factor. The proportionality coefficient at each diffraction peak was calculated by Rietveld analysis. The multipole refinement was used for the process of (2). The 1-D diffraction data at 30 K were selected for the observation of electron density distributions of both aluminum and molybdenum. The reasons are as follows: these 30 K data has the largest number of observed diffraction peaks, the effect of ice can be ignored, and the effect of thermal vibration is the smallest.

Firstly, an intensity of the thermal diffuse scattering was estimated with the 1-D diffraction data of 30 K. Secondly, the Rietveld refinement was performed. Here, the lattice constants,  $U_{\text{iso}}$ , and background intensity were determined. Thirdly, the anharmonic thermal vibration was estimated. Finally, intensity ratios of completely overlapped diffraction peaks were determined by the multipole refinement. The Section 4.2 is the principle of the Rietveld refinement. This includes a description of the model of the structure factor of the Rietveld refinement. The Section 4.3 explains the principle of the multipole refinement and the model of structure factors. The determination of intensity ratios of completely overlapped diffraction peaks is also described. The Section 4.4 shows a method for the analysis of thermal diffuse scattering intensity. The Section 4.5 shows the analysis method of the estimation of anharmonic thermal vibration. The Section 4.6 explains the set of structure factors used in this study. This includes a description of the difference of structure factor models between the Rietveld refinement and multipole refinement.

## 4.2 Principle of Rietveld refinement

Rietveld refinement is a refinement method of a model crystal structure using the IAM. Here, the parameters of the model crystal structure are the lattice constant, the fractional coordinate of atomic site, and the atomic displacement parameter. These parameters are determined by the least squares method of the intensity count  $y_{\text{obs}}$  for each data point in the 1-D diffraction data from the experiment and count  $y_{\text{model}}$  calculated from the model:

$$y_{\text{res}} = \sum_{i=1}^N w_i \{y_{\text{obs},i} - y_{\text{model},i}\}^2$$

where  $y_{\text{res}}$  is the residual square summation,  $i$  is the number of data points,  $w_i$  is the weighting parameter, and  $y_{\text{obs}}$  is the count at each  $2\theta$  position in 1-D diffraction data.

The integrated intensity in 1-D diffraction data  $I_{\text{obs}}$  is estimated from  $y_{\text{obs}}$ .  $I_{\text{obs}}$  is represented by the following expression:

$$I_{\text{obs}} = m_{hkl} |F_{\text{obs}}(\mathbf{H}_{hkl})|^2 LP_{hkl} T_i(\mathbf{H})$$

where  $m_{hkl}$  is the multiplicity,  $F_{\text{obs}}(\mathbf{H}_{hkl})$  is the observed structure factor,  $LP_{hkl}$  is the Lorentz-polarized factor,  $LP_{hkl} = (1 + \cos^2 2\theta) / (\sin \theta \sin 2\theta)$ , and  $T_i(\mathbf{H})$  is the thermal vibration term. The integrated intensity of Rietveld refinement  $I_{\text{model}}$  is represented by the following expression:

$$I_{\text{model}} = sm_{hkl} |F_R(\mathbf{H}_{hkl})|^2 LP_{hkl} T_o(\mathbf{H})$$

where  $s$  is the scale factor between  $I_{\text{obs}}$  and  $I_{\text{model}}$ ,  $F_R(\mathbf{H}_{hkl})$  is the structure factor of model,  $T_o(\mathbf{H})$  is harmonic thermal vibration term.  $F_R(\mathbf{H}_{hkl})$  is expressed by the following equation:

$$F_R(\mathbf{H}_{hkl}) = \sum_j^N f_j(\mathbf{H}) \exp\{2\pi i(hx_j + ky_j + lz_j)\}$$

where the atomic scattering factor  $f_j(\mathbf{H})$  is a Fourier transform of a spherical electron density distribution of atom. For this reason, the structure factor  $F_R(\mathbf{H}_{hkl})$  follows the IAM model and does not consider the electron redistribution.

Figure 4.1 is a schematic diagram of the integrated intensity,  $I_{\text{obs}}$ , the calculated integrated intensity,  $I_{\text{calc}}$ , and the relationship between the integrated intensity and structure factor.  $I_{\text{obs}}$  is the area of the diffraction peak above the background intensity. The integrated intensity is proportional to the square of the structure factor.  $I_{\text{calc}}$  is estimated by the sum of rectangles whose height is the count of the model  $y_{\text{model}}$ . The interval between measurement points on diffraction angle in the diffraction data is  $0.01^\circ$ .

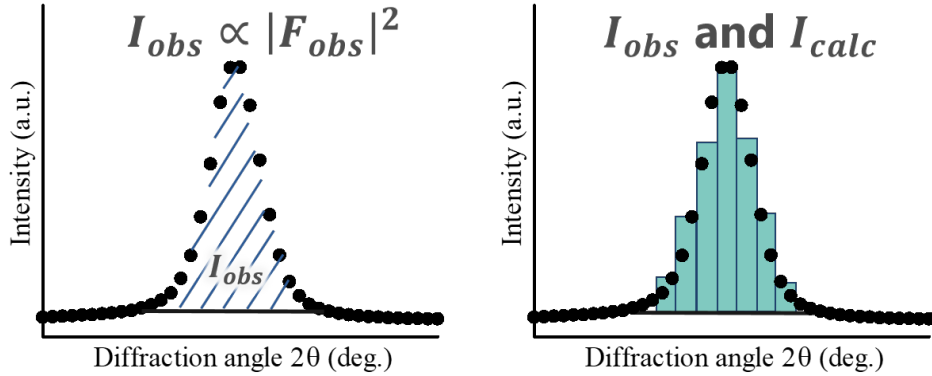


Figure 4.1 A schematic diagram of the integrated intensity of the experiment  $I_{\text{obs}}$ , the integrated intensity of the model  $I_{\text{calc}}$ , and the relationship between the integrated intensity and structure factor.

In the case of powder X-ray diffraction of aluminum, several diffraction peaks such as 333/511 and 600/442 completely overlap on  $2\theta$  position. Table 4.1 lists the structure factors of the Rietveld refinement of these completely overlapping diffraction peaks. For Rietveld refinement, the estimated values of the respective structure factors in the pairs are equal, since the estimation is based on the IAM model. On the other hand, the values of these structure factors are important because these represent an anisotropy of the electron density distribution by the electron redistribution.

Table 4.1 The structure factors of Rietveld refinement of completely overlapping diffraction peaks of 333/511 and 600/442.

$hkl$	Rietveld
3 3 3	3.99
5 1 1	3.99
6 0 0	3.18
4 4 2	3.18

The agreement of count between experiment and Rietveld refinement is represented by a reliability factor  $R_{wp}$ .

$$R_{wp} = \left\{ \frac{\sum_{i=1}^N w_i [y_{obs,i} - y_{model,i}]^2}{\sum_{i=1}^N w_i y_{obs,i}^2} \right\}^{\frac{1}{2}}$$

where,  $w_i$  is the weighting parameter,  $w_i = 1/y_{obs}$ . The agreement of integrated intensity between experiment and Rietveld refinement is represented by a reliability factor  $R_1$ .

$$R_1 = \frac{\sum_{j=1}^M |I_{obs,j} - I_{calc,j}|}{\sum_{j=1}^M I_{obs,j}}$$

### 4.3 Principle of multipole refinement

Multipole refinement employs a non-spherical atomic electron density distribution called multipole model. The non-spherical atomic electron density distribution  $\rho_{mp}(\mathbf{r})$  is expressed by the following equation:

$$\rho_{mp}(\mathbf{r}) = P_c \rho_{core}(r) + P_v \kappa^3 \rho_{valence}(\kappa r) + \sum_{l=0}^{l_{max}} \kappa'^3 R_l(\kappa' r) \sum_{m=0}^l P_{lm\pm} d_{lm\pm}(\theta, \phi).$$

The first term on the right-hand-side gives the spherical electron distribution of the inner shell electrons. The second term gives the spherical electron distribution of the outer shell electrons. The third term gives the deformation density distribution from the spherical electron density distribution of the outer shell electrons.  $r$ ,  $\theta$ , and  $\phi$  are the radial distance from the atomic center of origin and the azimuth angles.  $l$  is a positive integer,  $-l \leq m \leq l$ .  $R_l$  is the radial function,  $P_{lm\pm}$  is the electron population parameter in the multipole functions, and  $d_{lm\pm}(\theta, \phi)$  is the density function by the real spherical harmonics.  $P_c$  is the electron population of the inner shell electrons,  $P_v$  is the electron population of the outer shell electrons,  $\kappa$  is the expansion / contraction parameter of the spherical distribution of the outer shell electrons, and  $\kappa'$  is the expansion / contraction parameter of the radial function in the deformation density distribution.

Figure 4.2 shows the equation of multipole model and the schematic view of the electron density distribution for each term. The third term is called static deformation density. This multiplies the radial function and the spherical harmonic function. Here, “static” means the elimination of effects of thermal vibrations. The static deformation density has positive and negative electron densities. The

sum of the charges in the distribution is zero.

$$\rho_{\text{at}}(r) = P_c \rho_{\text{core}}(r) + P_v \kappa^3 \rho_{\text{valence}}(\kappa r) + \sum_{l=0}^{l_{\text{max}}} \kappa'^3 R_l(\kappa' r) \sum_{m=0}^l P_{lm\pm} d_{lm\pm}(\theta, \phi)$$

Multipole model
Spherical inner electron density
Spherical outer electron density
Deformation electron density



Figure 4.2 The equation of multipole model and schematic view of electron density distribution for each term.

In cubic symmetry, point group symmetric elements are linear combinations of spherical harmonic functions. This is called Kubic harmonics [33]. Kubic harmonics  $K_{ij}$  is a linear combination of the multiplication of coefficients  $k_{jm\pm}^l$  and real spherical harmonics  $y_{lm\pm}$ .

$$K_{ij} = \sum_{m\pm} k_{jm\pm}^l y_{lm\pm}$$

A pick-up rule of indices for spherical harmonics under a site symmetry was given by Kurki-Suonio [34]. In cubic symmetry, only  $lj = 01, 41, 61 \dots$  are symmetry allowed. Table 4.2 shows the coefficients  $k_{jm\pm}^l$  of the Kubic harmonics. 0+ and 4+ are indices  $m \pm$ .

Table 4.2 The coefficients  $k_{jm\pm}^l$  of the Kubic harmonics.

$l$	$j$	0+	4+
0	1	1	
4	1	0.76376	0.64550
6	1	0.35355	-0.93541

Multipole refinement is the least squares fitting of the input structure factor  $F$  and the structure factor based on multipole model  $F_{\text{MP}}$ . The fitting parameters are the electron population parameters and the expansion / contraction parameters. These parameters are determined by the least squares fitting. Then, the parameters are introduced into the multipole model. Finally, the non-spherical atomic electron density distribution  $\rho_{\text{mp}}(\mathbf{r})$  is reproduced. The superposition of  $\rho_{\text{mp}}(\mathbf{r})$  reproduces the electron density distribution of a crystal.  $F_{\text{MP}}$  is the superposition of the atomic scattering factor of  $\rho_{\text{mp}}(\mathbf{r})$ . Since the multipole model is merely a superposition of the atomic center electron density distribution, the parameters of the electron population and expansion / contraction do not have any physical meaning. The parameters are only for the accurate reproduction of the electron density distribution. The agreement between  $F$  and  $F_{\text{MP}}$  is represented by a reliability factor  $R_F$ .

$$R_F = \frac{\sum |F - kF_{\text{MP}}|}{\sum |F|}$$

where,  $k$  is the scale factor between  $F$  and  $F_{\text{MP}}$ .

Figure 4.3 shows the procedure of determination of observed structure factor. The background intensity in 1-D diffraction data is determined by the Rietveld refinement. Here, the integrated intensity  $I_{\text{obs}}$  of independent diffraction peak is determined. In the determination of the structure factor  $F_{\text{obs}}$  from  $I_{\text{obs}}$ ,  $m_{hkl}$  and  $LP_{hkl}$  at each diffraction peak are required. These values were calculated in the Rietveld refinement.  $T_i(\mathbf{H})$  was analyzed separately for harmonic thermal vibration and anharmonic thermal vibration. The integrated intensity of completely overlapping diffraction peaks is determined by multipole refinement. For this reason, the model bias of the multipole refinement only affects the structure factor of the completely overlapping diffraction peak.

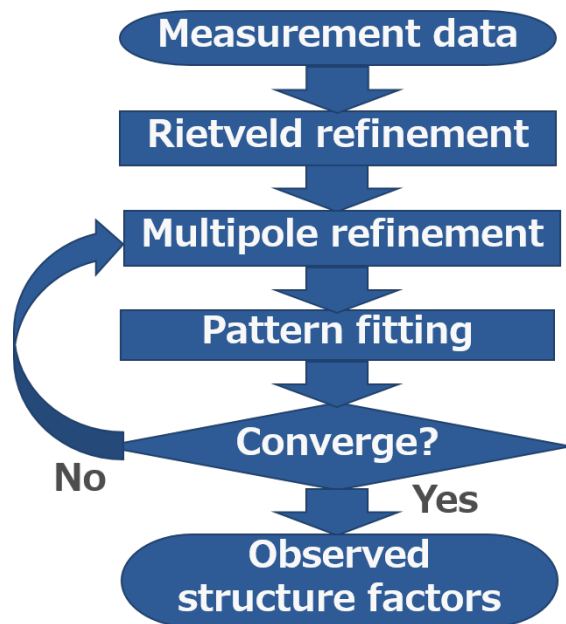


Figure 4.3 The analysis procedure in this research.

Table 4.3 shows the structure factors in the multipole refinement of completely overlapping diffraction peaks in Table 4.1. The structure factors in the pair take the difference values due to the electron redistribution. In  $F_{\text{obs}}$ , these are same value due to their errors. For reproduction of the electron density distribution by the multipole refinement, these different values in  $F_{\text{MP}}$  are used.

Table 4.3 The structure factors values in multipole refinement of completely overlapping diffraction peaks.

$hkl$	Multipole	Rietveld
3 3 3	3.98	3.99
5 1 1	3.97	3.99
6 0 0	3.17	3.18
4 4 2	3.16	3.18

The  $d$ -orbital population of transition metal atoms is derived from the electron population parameter of the multipole model. Assuming that (1) the  $d$ -orbital can be expressed by a single Slater type orbital and (2) the overlapping of the  $d$ -orbitals between the nearest atoms is small. The

relationship between the  $d$ -orbital population and electron population parameter of the multipole model is derived from an equivalence of two different descriptions of the atomic electron density. The one is a linear combination of atomic orbitals (LCAO) based atomic electron density and another one is based on the multipole model.

The  $d$ -electron density distribution in the LCAO is expressed by the atomic orbitals  $d_i$ .

$$\rho_d = \sum_{i=1}^5 P_i d_i^2 + \sum_{i=1}^5 \sum_{j>i}^5 P_{ij} d_i d_j$$

$\rho_d$  is the  $d$ -electron density distribution,  $d_i = R(r)y_{lm\pm}$ . The mixing term  $d_i d_j$  occurs when overlapping of the  $d$ -orbitals exists. The terms only occur between orbitals which belong to the same symmetry representation. In an octahedral group, that is  $m\bar{3}m$  ( $O_h$ ), the  $d$ -orbital is split into the bonding orbital  $T_{2g}$  and the antibonding orbital  $e_g$ . In multipole model, the atomic  $d$ -electron density is expressed by the spherical outer electron density distribution and deformation density terms.

$$\rho_d = P_v \rho_{\text{valence}}(\kappa r) + \sum_{l=0}^4 \left\{ R_l(\kappa' r) \sum_{m=0}^l P_{lm\pm} y_{lm\pm} \left( \frac{r}{r} \right) \right\}$$

When the two  $\rho_d$  are equal, a coefficient of a relationship between  $P_{lm}$  and  $P_i$  or  $P_{ij}$  can be defined.

Table 4.4 shows the relationship between the  $d$ -orbital populations  $P_i$  or  $P_{ij}$  and the electron population parameter  $P_{lmp}$ . From  $P_z$  to  $P_{xy}$  belong to  $P_i$ .  $P_{x^2-y^2/xy}$  represents a mixing term  $P_{ij}$ .  $P_{00}$ ,  $P_{40}$ , and  $P_{44+}$  are the electron population parameters of the multipole model. Multipole functions which consist of the radial function and real spherical harmonic function are limited by the site symmetry of a crystal. In the molybdenum bcc lattice, the site symmetry is  $m\bar{3}m$  ( $O_h$ ), hence the symmetry-allowed multipole functions in the  $d$ -orbital density are  $lmp = 00, 40$ , and  $44+$ , where  $44+ = 0.74048 \times 40$ .

Table 4.4 The relationship between the  $d$ -orbital populations  $P_i$  or  $P_{ij}$  and the electron population parameter  $P_{lmp}$ .

Orbital	$P_{00}$	$P_{40}$	$P_{44+}$
$P_z$	0.200	1.396	0.000
$P_{xz}$	0.200	-0.931	0.000
$P_{yz}$	0.200	-0.931	0.000
$P_{x^2-y^2}$	0.200	0.233	1.571
$P_{xy}$	0.200	0.233	-1.571
$P_{x^2-y^2/xy}$	-	-	3.142

## 4.5 Analysis of anharmonic thermal vibration

The anharmonic thermal vibrations are expressed by third or higher order terms in the Taylor series expansion of the potential energy of a crystal due to atomic displacement.

$$\mathcal{V} = \mathcal{V}_0 + \sum_{slj} u_{sl}^j \left[ \frac{\partial \mathcal{V}}{\partial u_{sl}^j} \right]_0 + \frac{1}{2} \sum_{ss', ll', jj'} u_{sl}^j u_{s'l'}^{j'} \left[ \frac{\partial^2 \mathcal{V}}{\partial u_{sl}^j \partial u_{s'l'}^{j'}} \right]_0 + \frac{1}{3!} \sum_{\substack{ss's'' \\ ll'l'' \\ jj'j''}} u_{sl}^j u_{s'l'}^{j'} u_{s''l''}^{j''} \left[ \frac{\partial^3 \mathcal{V}}{\partial u_{sl}^j \partial u_{s'l'}^{j'} \partial u_{s''l''}^{j''}} \right]_0 \dots$$

$\mathcal{V}$  is the potential energy of whole crystal,  $u_{sl}$  is the displacement from the equilibrium position of the  $s$ -th atom in the  $l$ -th unit cell, and  $j$  represents the components of the Cartesian coordinates. The 0th order term is the potential energy in a static crystal. The first-order term is 0 because it is near equilibrium. The second-order term is a harmonic term.

The probability density function (pdf) of atomic thermal vibration is expressed by the Gram-Charlier expansion. In harmonic oscillation, the pdf is Gaussian pdf. When including anharmonic thermal vibrations, the Taylor series expansion with the Gaussian pdf is used. This is called the Gram-Charlier expansion.

$$P(\mathbf{u}) \approx \left[ 1 - c^j D_j + \frac{c^{jk}}{2!} D_j D_k - \frac{c^{jkl}}{3!} D_j D_k D_l + \frac{c^{jklm}}{4!} D_j D_k D_l D_m \cdots + (-1)^r \frac{c^{\alpha_1 \cdots \alpha_r}}{r!} D_{\alpha_r} \cdots D_{\alpha_1} \right] P_0(\mathbf{u})$$

$P(\mathbf{u})$  is the pdf,  $P_0(\mathbf{u})$  is the Gaussian pdf,  $D_{\alpha_r} \cdots D_{\alpha_1}$  represents the partial derivatives, and  $c^{\alpha_1 \cdots \alpha_r}$  is the element of coefficient tensor. The pdf of anharmonic vibration is expressed by third or higher order terms. In the expansion up to the fourth order, only the fourth terms  $D_{1111}$  and  $D_{1122}$  remain under site symmetry  $m\bar{3}m$ .

Figure 4.4 shows the schematic diagram of the 2-dimensional contour plot of pdfs by  $D_{1111}$  and  $D_{1122}$  around an atom.  $y$  and  $z$  shows the crystal axis. The origin is the center of the atom. The blue regions represent negative values, while the red regions are positive values. The positive values distribute to the  $[111]$  and  $[100]$  directions in  $D_{1111}$  and  $D_{1122}$ , respectively. The negative values distribute around the atom.

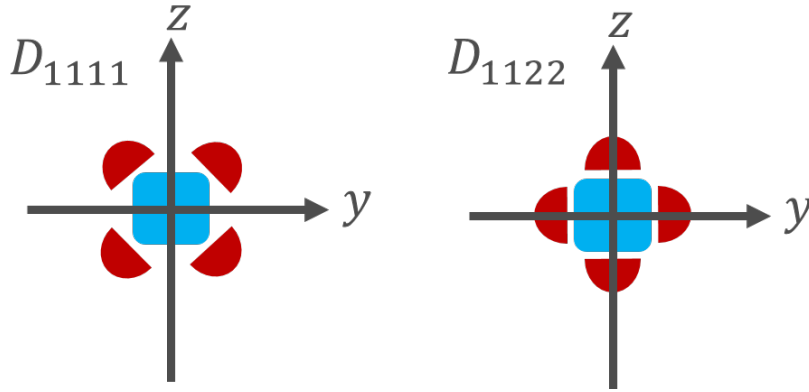


Figure 4.4 The schematic diagram of the 2-dimensional contour plot of pdfs by  $D_{1111}$  and  $D_{1122}$  around an atom.

## 4.5 Analysis of thermal diffuse scattering

Thermal vibration causes a change of electron density distribution due to the atomic vibration and thermal diffuse scattering in the X-ray diffraction. The former is explained in Section 4.4. The latter is the phonon-assisted Bragg reflection due to the sum of the diffraction vector and the wave vector of the phonons of lattice vibration. The thermal diffuse scattering occurs in both the harmonic thermal vibration and anharmonic thermal vibration. Figure 4.5 is a schematic view of the normal Bragg reflection and thermal diffuse scattering in the reciprocal lattice space. (a) is the normal Bragg

reflection, (b) is the first order thermal diffuse scattering, and (c) is the second order thermal diffuse scattering. The frame of black lines represent the reciprocal lattice. The triplet number shows indices  $hkl$  for the reciprocal lattice points. The diffraction vectors arise from the origin of the reciprocal lattice 000. Note that the thermal diffuse scattering intensity in the figure is largely emphasized. The normal Bragg reflection occurs when the diffraction vector is terminated on the reciprocal lattice point. The first order thermal diffuse scattering is the Bragg reflection assisted by single phonon of lattice vibration. The wave vector of the phonon arise from the reciprocal lattice points with the normal Bragg reflection. Scattered X-rays due to the thermal diffuse scattering have an intensity at the end point of the diffraction vector and the wave vector of the phonon. The thermal diffuse scattering near the reciprocal lattice point occurs even when the lattice vibration is small. The thermal diffuse scattering in a region between adjacent reciprocal lattice points occurs only when the wave vector of the phonon is large, that is, when the thermal vibration is intense at high temperature. For this reason, the first-order thermal diffuse scattering takes a local maximum value at the positions of the reciprocal lattice point with the normal Bragg reflections. The second order thermal diffuse scattering is the Bragg reflection assisted by two phonons. The wave vector of the second phonon arises from the end of the wave vector of the first phonon. The second order thermal diffuse scattering has a local maximum value at the position of the reciprocal lattice point with the normal Bragg reflection as with the first order thermal diffuse scattering. However, the difference in intensity between the local maximum value and value of midpoint between adjacent reciprocal lattice points is smaller than that of the first order thermal diffuse scattering. Olmer [35] reported that the intensity of the second order thermal diffuse scattering between adjacent reciprocal lattice points reaches 30% for that of the first order thermal diffuse scattering.

Figure 4.6 shows (a) an expanded view of the background scattering of 1-D diffraction data of 30 K and 600 K of aluminum and (b,c) the change in intensity of the diffraction peak due to thermal diffuse scattering. In figure 4.6(a), the shape of the background of 600 K of red line is different from 30 K of black line. The blue line shows noticeable parts of the difference. Figure 4.6(b) shows the intensity of diffraction peak  $I_{\text{Bragg}}$  and thermal diffuse scattering intensity  $I_{\text{TDS}}$ . Figure 4.6(c) shows the apparent intensity of the diffraction peak at 600 K by  $I_{\text{Bragg}} + I_{\text{TDS}}$ . If the  $I_{\text{TDS}}$  is not estimated, the intensity of the diffraction peak apparently increases and the estimate of the integrated Bragg intensity becomes inaccurate.

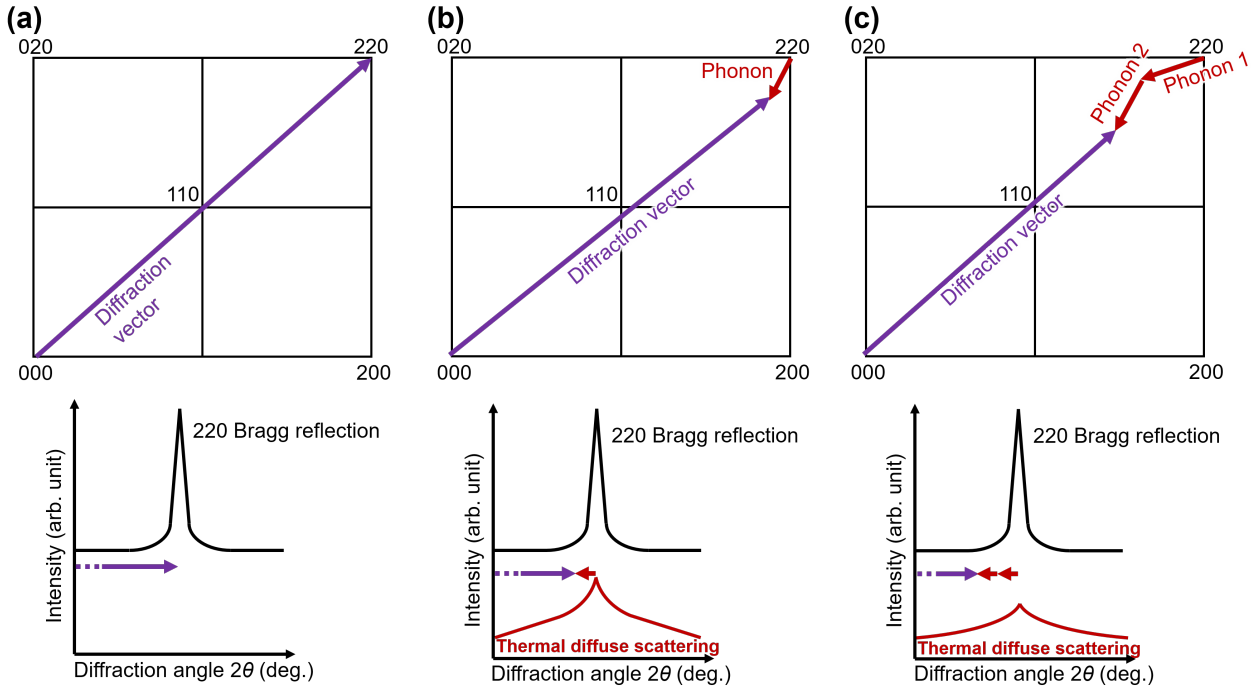


Figure 4.5 Schematic view of (a) normal Bragg reflection, (b) first-order, and (c) second-order thermal diffuse scattering in reciprocal lattice space and 1-D diffraction data.

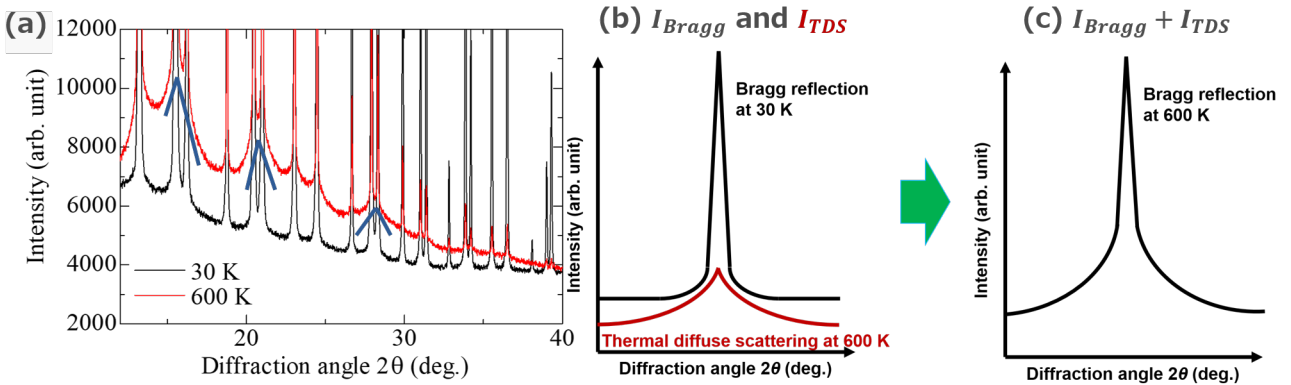


Figure 4.6 (a) An expanded view of the background scattering of 1-D diffraction data of 30 K and 600 K of aluminum and (b,c) the change in intensity of the diffraction peak due to thermal diffuse scattering.

In the estimation of thermal diffuse scattering intensity, an equation of the theoretical thermal diffuse scattering intensity was used. Firstly, the model of a crystal with an atomic thermal vibration is defined. Although the thermal diffuse scattering arises from both harmonic and anharmonic thermal vibrations, the present analysis assumes only the presence of the harmonic thermal vibration. Then, the equation of the intensity of the thermal diffuse scattering at any point in the reciprocal lattice space is derived. The intensity of thermal diffuse scattering in the 1-D diffraction data of powder X-ray diffraction is a summation of the intensity distribution of the thermal diffuse scattering equidistant from the origin of the reciprocal lattice space. This is an integral on a spherical surface at an equidistant from the origin of the reciprocal lattice space. The equation of the thermal diffuse scattering intensity

under a high temperature approximation is derived. Finally, an expression corresponding to the all temperature by Herbstein and Averbach [36] is derived.

Figure 4.7 shows a two-dimensional schematic view of a position of an atom  $s$  in an arbitrary unit cell  $l$  from the origin of a crystal. The area surrounded by the solid black line represents a unit cell. The lower left shows the origin of the crystal. The position of the origin of a unit cell  $l$  is expressed by the following equation.

$$l = l_1 \mathbf{a}_1 + l_2 \mathbf{a}_2 + l_3 \mathbf{a}_3$$

Here,  $\mathbf{a}_{1,2,3}$  are vectors of the crystal axes, and  $l_{1,2,3}$  are integers. Let  $\mathbf{r}_s$  be the position vector from the origin  $l$  of the unit cell to an atom  $s$  in the unit cell. The position vector  $\mathbf{R}_{sl}$  of the atom  $s$  from the origin of the crystal is given by the following equation.

$$\mathbf{R}_{sl} = l_1 \mathbf{a}_1 + l_2 \mathbf{a}_2 + l_3 \mathbf{a}_3 + \mathbf{r}_s$$

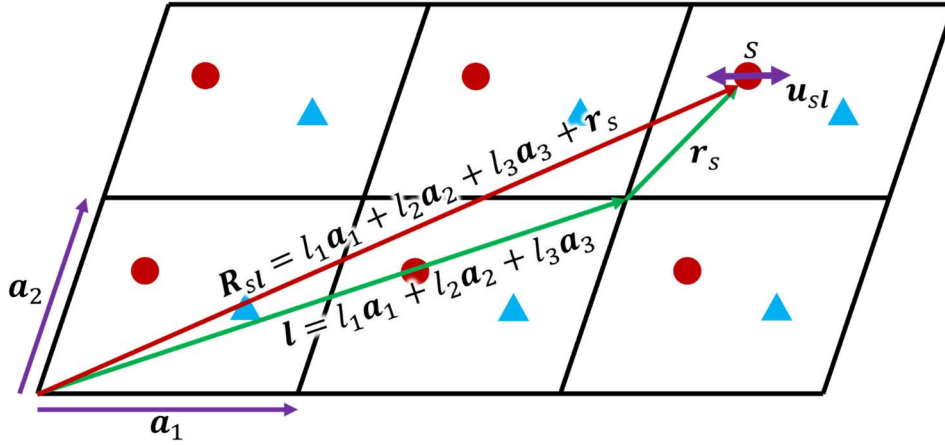


Figure 4.7 Two-dimensional schematic view of a position of an atom  $s$  in an arbitrary unit cell  $l$  from the origin of a crystal.

A thermal effect in the crystal is represented by the atomic thermal vibration. Assuming that (1) the thermal vibrations are represented by the harmonic vibrations around its equilibrium position  $\mathbf{R}_{sl}$ , (2) the thermal vibration of each atom is not independent, that is, multiple atoms have the same thermal vibration. Let  $\mathbf{u}_{sl}$  be the displacement of the atom  $s$  in the unit cell  $l$  from its equilibrium position  $\mathbf{R}_{sl}$ . The position of atom  $s$  at a moment is represented by  $\mathbf{R}_{sl} + \mathbf{u}_{sl}$ . The kinetic energy  $E_k^s$  per atom  $s$  is given by the following equation due to harmonic vibration:

$$E_k^s = \frac{1}{2} M_s \left| \frac{d}{dt} \mathbf{u}_{sl} \right|^2$$

where  $M_s$  is a mass of atom  $s$ . The kinetic energy from all atoms  $s$  in the crystal is the summation of the kinetic energies by all atoms  $s, s', s'', \dots$  with the position  $\mathbf{r}_s$  from the origin of each unit cell.

$$E_k = \sum_s \sum_l \frac{1}{2} M_s \left| \frac{d}{dt} \mathbf{u}_{sl} \right|^2$$

When multiple atomic species are contained in the unit cell, the total kinetic energy of the crystal is the summation of  $E_k$  for each atom.

Assuming that the function  $V(\mathbf{u}_{sl})$  represented by the potential energy of the crystal  $E_p$  with displacement  $\mathbf{u}_{sl}$  due to the thermal vibrations exist. When all atoms in the crystal are at its

equilibrium position  $\mathbf{R}_{sl}$  the crystal is most stable.  $V(\mathbf{u}_{sl})$  takes the minimum value with displacement  $\mathbf{u}_{sl} = 0$ . Since the thermal vibration is smaller than the nearest interatomic distance,  $V(\mathbf{u}_{sl})$  can be expanded into a power-series around the equilibrium position.

$$V(\mathbf{u}_{sl}) = V_0 + \sum_s \sum_l u_{sl} \left\{ \frac{\partial}{\partial u_{sl}} V(\mathbf{u}_{sl}) \right\} + \sum_s \sum_{s'} \sum_l \sum_{l'} u_{sl} \left\{ \frac{\partial^2}{\partial u_{sl} \partial u_{s'l'}} V(\mathbf{u}_{sl}) \right\} u_{s'l'} + \dots$$

$V_0$  is  $E_p$  when all atoms  $s, s', s'', \dots$  are at its equilibrium position. Since the thermal vibration was approximated by the harmonic vibration, the equation of motion of the thermal vibration is derived from the third term of  $V(\mathbf{u}_{sl})$ :

$$M_s \frac{d^2}{dt^2} \mathbf{u}_{sl} = - \sum_{s'} \sum_{l'} \left\{ \frac{\partial^2}{\partial u_{sl} \partial u_{s'l'}} V(\mathbf{u}_{sl}) \right\} u_{s'l'}$$

The right-hand-side represents a force acting on the atom  $s$  in the unit cell  $l$  caused by a displacement  $\mathbf{u}_{s'l'}$  of the atom  $s'$  in the unit cell  $l'$ .

The equation of motion satisfies the Bloch's theorem. The force acting between atoms depends only on a relative position of the atoms. Since  $l$  and  $l'$  are absolute positions, the relative position is defined as  $\mathbf{h} = l' - l$ . The equation of motion represented by  $\mathbf{h}$  is the following equation.

$$M_s \frac{d^2}{dt^2} \mathbf{u}_{sl} = - \sum_{s'} \sum_{l+h} \left\{ \frac{\partial^2}{\partial u_{sl} \partial u_{s'l+h}} V(\mathbf{u}_{sl}) \right\} u_{s'l+h}$$

If  $\mathbf{u}_{sl}(t)$  is a time-dependent function representing a displacement  $\mathbf{u}_{sl}$  in a unit cell  $l$ , there is a wave vector  $\mathbf{q}$  of thermal vibration expressed by the following equation from the Bloch condition.

$$\mathbf{u}_{sl}(t) = e^{i\mathbf{q} \cdot l} \mathbf{u}_{s0}(t)$$

$\mathbf{u}_{s0}(t)$  represents the displacement of the atom  $s$  in an arbitrary unit cell which is the origin of the unit cell  $l$ .  $e^{i\mathbf{q} \cdot l}$  is phase factor under the Bloch condition. From these, all atoms  $s, s', s'', \dots$  in the crystals are related to each other by Bloch's theorem. All atoms  $s, s', s'', \dots$  vibrate according to a same traveling wave represented by wave vector  $\mathbf{q}$ . The change due to a translation of unit cell is only phase factor.

In the crystal, there is a traveling wave due to the thermal vibration represented by the wave vector  $\mathbf{q}$ . In the case of three-dimension, the traveling wave  $\mathbf{q}$  can be decomposed into the one longitudinal wave and two transverse waves. Let  $\mathbf{e}_{qj}$  ( $j = 1, 2, 3$ ) be the unit vectors representing each vibration direction for each waves in the traveling wave  $\mathbf{q}$ . Let  $j = 1$  be the longitudinal wave and  $j = 2, 3$  be the two transverse waves. The wave  $j$  obtained by decomposition of a traveling wave  $\mathbf{q}$  is defined as a wave  $qj$ . The displacement  $\mathbf{u}_{sl}(t)$  of the atom  $s$  by a wave  $qj$  is expressed by the following equation:

$$\mathbf{u}_{sl}(t) = a_{qj} \mathbf{e}_{qj} \cos(\omega_{qj} t - 2\pi \mathbf{q} \cdot \mathbf{R}_{sl} - \delta_{qj})$$

where  $a_{qj}$  is amplitude of the wave  $qj$ ,  $\omega_{qj}$  is angular frequency of the wave  $qj$ , and  $\delta_{qj}$  is an arbitrary phase factor.  $\delta_{qj}$  indicates that the phase of each wave is independent and does not interfere with another wave.  $\mathbf{q} \cdot \mathbf{R}_{sl}$  is a component along  $\mathbf{R}_{sl}$  of the traveling wave  $\mathbf{q}$ .

Figure 4.8(a) shows schematic view of displacement of atomic positions according to a longitudinal wave. The green arrow is the traveling wave  $\mathbf{q}$ . The red circles represents atomic positions displaced by the traveling wave, and the blue circles represents their equilibrium positions. Black and gray circles indicate the red and blue atomic positions projected onto the axis  $q_x$ . Figure 4.8(b) shows

the interatomic distance  $\alpha + u_{sl}$  due to the atoms displaced in the longitudinal wave.  $\alpha$  is the distance before displacement between atoms.

The displacement of the atom  $s$  in unit cell  $l$  due to all waves  $qj$  in the crystal is the summation of displacements by all the waves  $qj$  in all traveling wave.

$$\mathbf{u}_{sl}(t) = \sum_{\mathbf{q}} \sum_j a_{qj} \mathbf{e}_{qj} \cos(\omega_{qj}t - 2\pi\mathbf{q} \cdot \mathbf{R}_{sl} - \delta_{qj})$$

In monoatomic crystals,  $s$  is vanished due to  $\mathbf{R}_{sl} = l$ .

$$\mathbf{u}_l(t) = \sum_{\mathbf{q}} \sum_j a_{qj} \mathbf{e}_{qj} \cos(\omega_{qj}t - 2\pi\mathbf{q} \cdot \mathbf{R}_l - \delta_{qj})$$

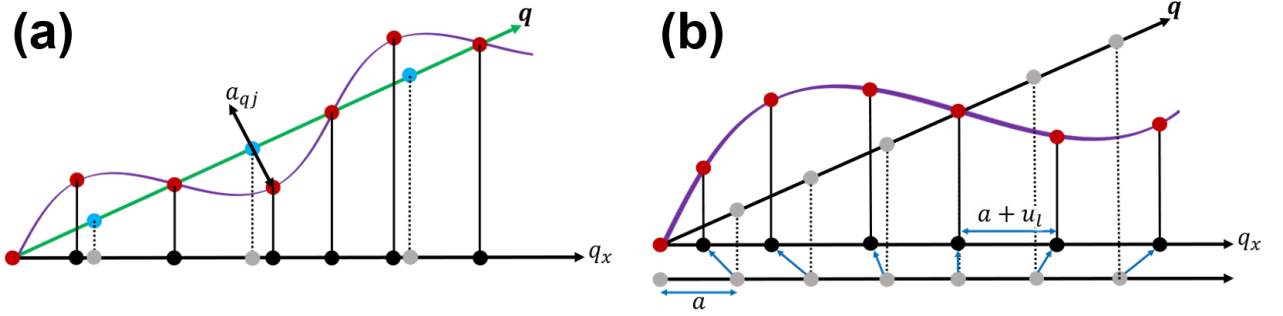


Figure 4.8 (a) Schematic view of displacement of atomic positions according to a longitudinal wave. (b) The interatomic distance  $\alpha + u_{sl}$  due to the atoms displaced in the longitudinal wave.

The following equation shows the first-order thermal diffuse scattering intensity of powder X-ray diffraction in fcc crystals:

$$G(X) = \frac{(3/\pi)^{\frac{2}{3}}}{6 \left\{ \phi(\chi) + \frac{1}{4}\chi \right\}} \frac{1}{X} \sum_{hkl} \frac{j_{hkl}}{X_{hk}} \ln \left\{ \frac{\sinh \frac{1}{2}\chi}{\sinh \left[ \frac{1}{2}\chi \left( \frac{1}{3}\pi \right)^{\frac{1}{3}} |X - X_{hk}| \right]} \right\}$$

where,  $X = 2a \sin \theta / \lambda$ ,  $X_{hkl} = 2a \sin \theta_{hkl} / \lambda$ ,  $\chi = \Theta/T$ .  $\phi(\chi)$  is the Debye integration,  $a$  is the lattice constants,  $j_{hkl}$  is the multiplicity of the  $hkl$  reflection,  $\Theta$  is the Debye temperature, and  $T$  is the measurement temperature. The amplitudes of the atomic thermal vibrations in solids are represented by elastic waves. Here, we assume that all elastic waves in solids have the same velocity. Each Brillouin zone is replaced by a sphere that has the same volume as the Brillouin zone. In a bcc crystal,  $(3/\pi)^{\frac{2}{3}}$  becomes  $(3/2\pi)^{\frac{2}{3}}$ .

The evaluation of the intensities of thermal diffuse scattering employed a scale factor  $\sigma_{\text{exp}}/\sigma_{\text{calc}}$ , where  $\sigma_{\text{exp}}$  is the difference of the background intensity between the 1-D diffraction data of 100 K and 300 K.  $\sigma_{\text{calc}}$  is the difference of  $G(X)$  between the calculated patterns of  $G(X)$  at 100 K and 300 K. It was assumed that the difference of the background intensity occurred only by first-order thermal diffuse scattering.

Figure 4.9 and 4.10 show the  $\sigma_{\text{calc}}$ ,  $\sigma_{\text{exp}}$ , and positions of the calculated scale factors. The upper figure shows the distribution of  $G(X)$  at 30 and 300 K for  $2\theta = 12$  to  $40^\circ$ . The lower figure shows the background intensity of the 1-D diffraction data at 30 K and 300 K for  $2\theta = 12$  to  $40^\circ$ . The vertical

axis is the intensity and the horizontal axis is the diffraction angle  $2\theta$ . 23 black vertical lines show the  $2\theta$  values at minima between the adjacent diffraction peaks. The positions of peaks in  $G(X)$  are completely overlapped with diffraction peaks due to  $|X - X_{hkl}|$  in the equation of  $G(X)$ . The averaged scale factor is calculated by the 23 scale factors. The thermal diffuse scattering is calculated by  $G(X)$  and the averaged scale factor.

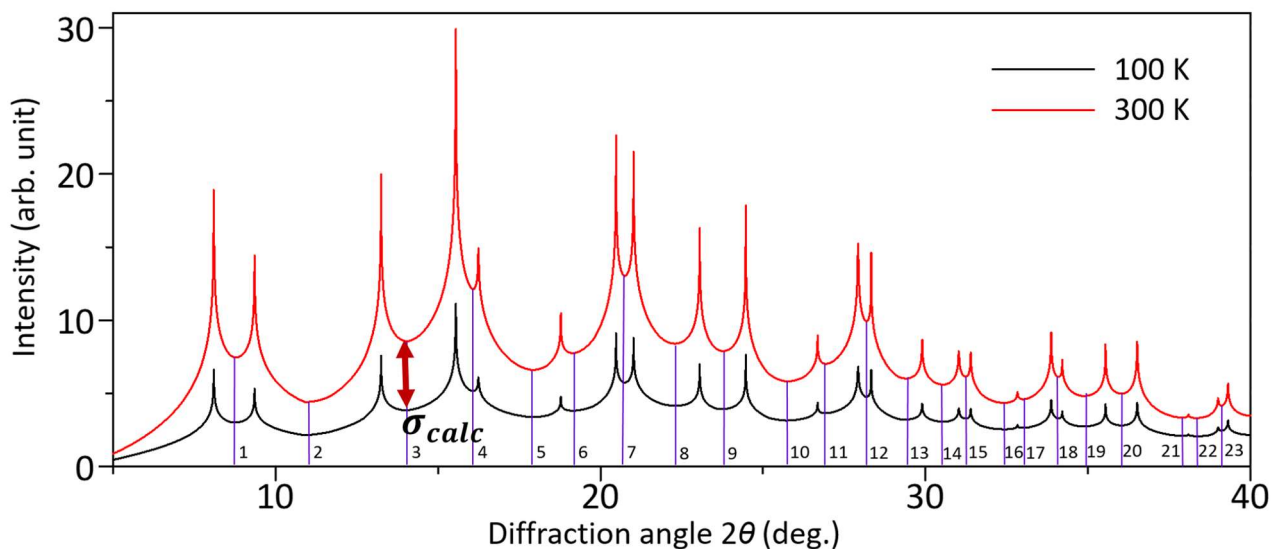


Fig. 4.9 The first order thermal diffuse scattering patterns for 100 and 300 K with labeled minimum points in  $2\theta = 0\sim 40^\circ$ .

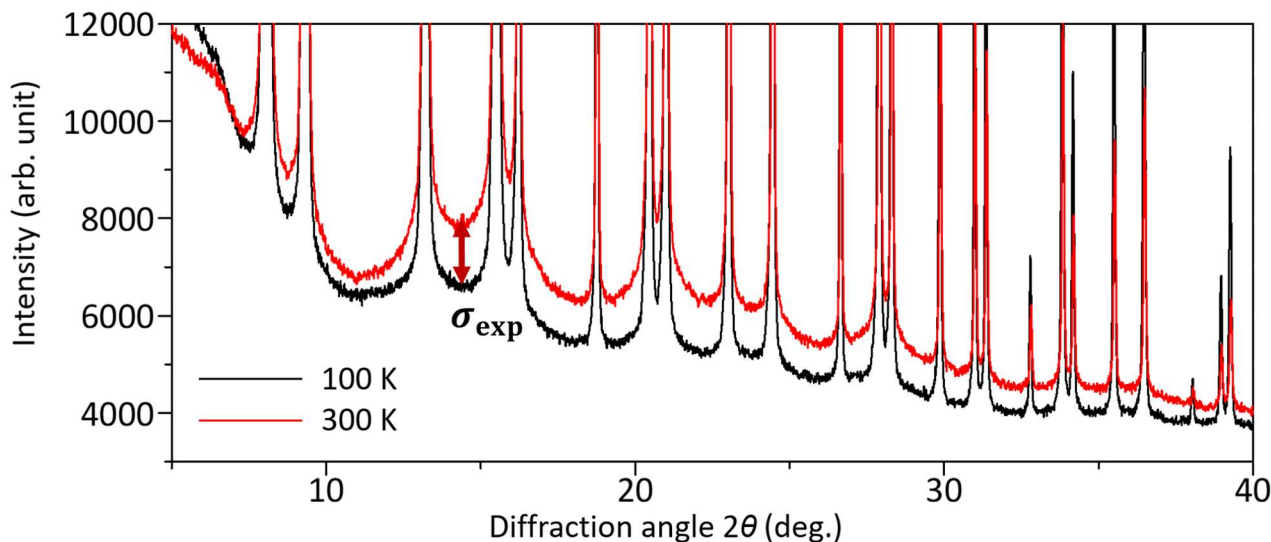


Fig. 4.10 The 1-D diffraction data at 100 and 300 K.

Figure 4.11 shows the intensity of calculated thermal diffuse scattering  $G(X)$  at 30 K and 600 K and 1-D diffraction data of 30 K and 600 K in aluminum. The horizontal axis is the diffraction angle and the vertical axis is the intensity. Red and black lines are the 600 K and 30 K, pink and purple lines are the intensities of thermal diffuse scattering calculated at 600 K and 30 K. The flat part is subtracted as background scattering. Ignore the intensity at the peak position as it diverges to infinity

in  $G(X)$ . For this reason, the intensity of the part surrounded by the red frame is important. In the example of 30 K of aluminum in figure 4.11, this was less than the statistical error in the 1-D diffraction data. For this reason, ignoring the intensity of thermal diffuse scattering with the 1-D diffraction data of aluminum at 30 K.

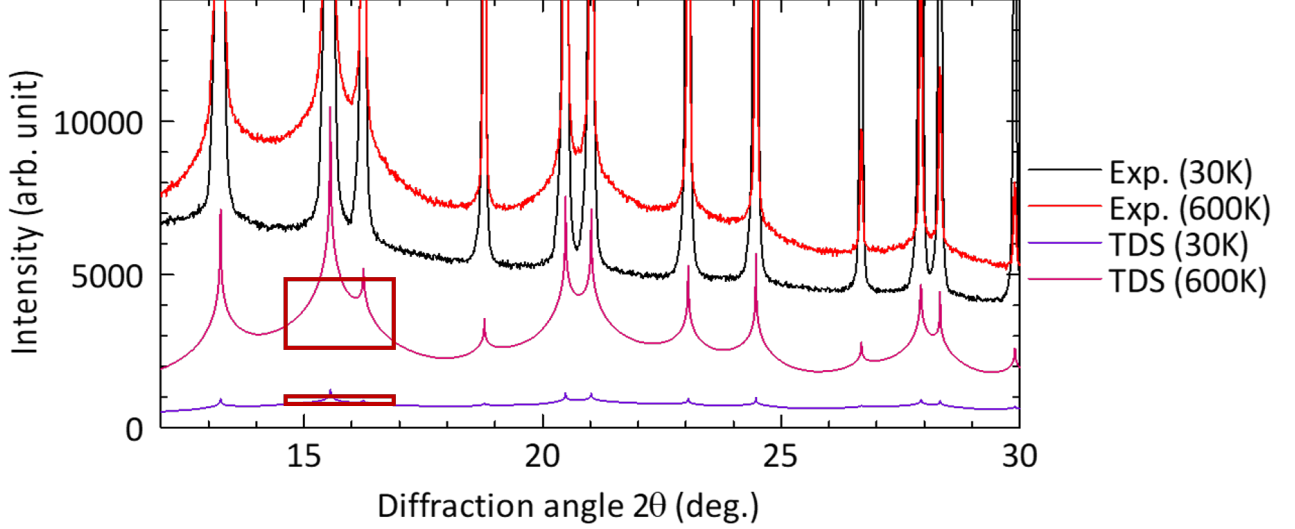


Figure 4.11 The intensity of calculated thermal diffuse scattering  $G(X)$  at 30 K and 600 K and 1-D diffraction data of 30 K and 600 K in aluminum.

## 4.6 Density functional theory

In this study, the theoretical electron density distributions of aluminum and molybdenum by the density functional theory were employed. The theoretical electron density distribution  $\rho_{\text{theo}}(\mathbf{r})$  was determined by FP-LAPW + GGA +  $lo$  +  $ls$  in WIEN2k package where FP-LAPW is the full potential-linearized augmented plane wave, GGA is the generalized gradient approximation,  $lo$  is the local orbitals, and  $ls$  is the local screening potentials. The theoretical structure factors  $F_{\text{theo}}(\mathbf{H})$  are the Fourier coefficients of the theoretical electron density distribution.

$$F_{\text{theo}}(\mathbf{H}) = \int \rho_{\text{theo}}(\mathbf{r}) \exp(2\pi i \mathbf{H} \cdot \mathbf{r}) d\mathbf{r}$$

More details descriptions of the equation are in Section 2.2.

The theoretical structure factor by WIEN2k was used in the multipole refinement to describe the theoretical electron density distribution. In the case of the fine electron density distribution where the difference of  $0.01 \text{ e}/\text{\AA}^3$  is important, the influence of the model bias by the multipole model in the division of the completely overlapping diffraction peak is unknown. To compare the electron density distribution of experiment and theory, the theoretical electron density distribution was described by the same procedure as the experiment. For this reason, structure factors were calculated from the theoretical electron density distribution of WIEN2k, then, the structure factor and the electron density distributions were reproduced by the multipole refinement. An agreement between the reproduced and original structure factor was also confirmed. This agreement guarantees the validity of the reproduced

electron density distribution.

Figure 4.12 shows a residual electron density distribution of the residual structure factors  $F_{\text{res}}$ . The structure factors consist of the theoretical aluminum structure factor  $^{\text{WIEN}}F_{\text{calc}}$  by WIEN2k and the reproduced structure factor  $^{\text{WIEN}}F_{\text{MP}}$  by the multipole refinement, and  $F_{\text{res}} = ^{\text{WIEN}}F_{\text{calc}} - ^{\text{WIEN}}F_{\text{MP}}$ . The residual density is  $\sim 0.01 \text{ e}/\text{\AA}^3$ . This means that the chemical bonding of metals can be reproduced by the multipole refinement. The feature of multipole refinement is a high reproducibility of electron density distribution with respect to that of actual crystals.

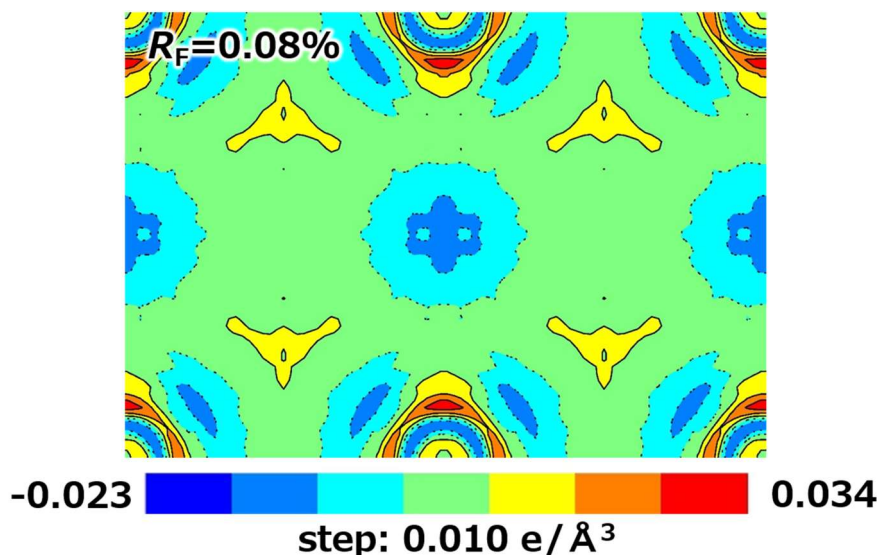


Figure 4.12 A residual electron density distribution of residual structure factors  $F_{\text{res}}$ .

## 4.7 Sets of structure factors

This research contains six sets of structure factors. These are the final observed structure factors and its reproduction by the multipole analysis, the theoretical structure factors and its reproduction by multipole refinement, the structure factors calculated by the IAM. The final observed structure factors is the observed structure factors in Figure 4.3.

Figure 4.13 shows the schematic view of the structure factors of IAM and multipole model in a fcc crystal. The structure factors by IAM can be calculated from the superposition of the atomic scattering factor  $f_{hkl}$  by the spherical electron density distribution of atoms. In fcc, the “static” structure factor  $F_{hkl}$  is expressed by the following equation:

$$F_{hkl} = 4f_{hkl}$$

where the values of  $f_{hkl}$  are taken from international tables for crystallography. When the index  $hkl$  does not satisfy  $h + k + l = \text{even}$ ,  $F_{hkl}$  value is vanished. Though the structure factors by multipole model are also a superposition of the atomic scattering factor, the atomic scattering factor consists of the non-spherical atomic electron density distribution of the multipole model. Hence, the structure factors of multipole model can express the electron redistribution of crystals.

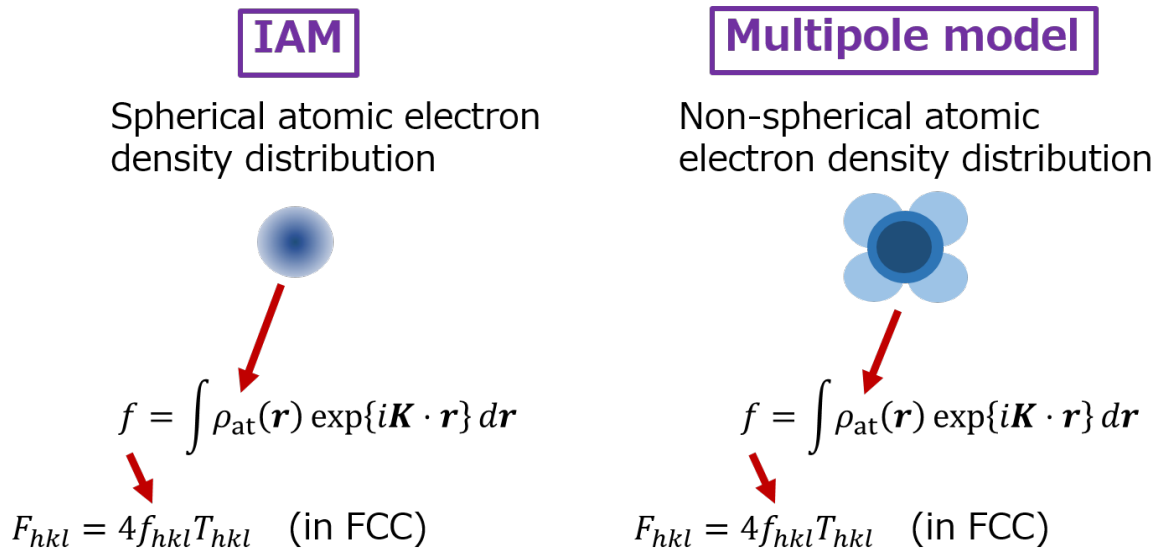


Figure 4.13 Schematic view of structure factors of IAM and multipole model in fcc crystal.  $\mathbf{K}$  represents scattering vector.

A modulation of structure factors is used for the comparison between the present experimental and other structure factors. Since the present synchrotron powder X-ray diffraction is relative measurement, the comparison between absolute values of structure factor sets cannot be executed. The modulation of structure factors is based on the relative values of the experimental or theoretical structure factors and the IAM structure factors  ${}^{\text{IAM}}F_{hkl}$ .

$${}^{\text{IAM}}F_{hkl} = \frac{F_{hkl}}{{}^{\text{IAM}}F_{hkl}}$$

$F_{hkl}$  is the experimental or theoretical structure factors for each  $hkl$ .  ${}^{\text{IAM}}F_{hkl}$  is the IAM structure factors for each  $hkl$ . For instance, at  $hkl = 111$ , the present theoretical structure factor and IAM structure factor of the aluminum is 8.86 and 8.95.  ${}^{\text{IAM}}F_{111} = 8.86 / 8.95 = 0.990$ .  ${}^{\text{IAM}}F_{hkl}$  are calculated for all structure factors in all sets. Then, all  ${}^{\text{IAM}}F_{hkl}$  are normalized with the value of  ${}^{\text{IAM}}F_{111}$  in the aluminum and  ${}^{\text{IAM}}F_{110}$  in molybdenum. The plot of the normalized values versus  $\sin \theta / \lambda$  called “modulation of structure factors”. This is same as Figure 2.9 in Section 2.6.

## Chapter 5 Charge density and thermal motion of aluminum

### 5.1 Introduction

The accurate observation of the electron density distribution of aluminum is a fundamental issue in the solid state physics. The electronic state of aluminum is thought to be close to the free electron gas. This indicates a small electron redistribution due to the small chemical bonding. The small redistribution requires the extremely accurate low order structure factors, which can discriminate the difference of 1% in the structure factors of aluminum. The 11 results of experiments and 10 theoretical calculations have reported about the structure factors of aluminum. The resolution of these experiments before 2000 cannot distinguish the difference of 1%. As shown in Section 2.6, only one report by Nakashima et al. detected the 1% and they observed the chemical bonding of aluminum.

Nakashima et al. practically solved the difficulty of measuring an extremely accurate low order structure factor using the quantitative convergent-beam electron diffraction (QCBED) technique [6]. They measured 111 and 200 reflections of aluminum with sufficient accuracy to detect the deviations from free electron gas model. The charge density distribution of the aluminum was determined using the combined data of QCBED and XRD. They observed an electron accumulation at the tetrahedral site which is consistent with the density functional theory. They also found the relationship between the Young's modulus and observed deformation density.

A quantitatively accurate charge density of a metal provides an important clue for the understanding, development, and improvement of metal and related alloys [6]. Recent progress of synchrotron radiation (SR) XRD for a charge density study has enabled us to perform such a study. The diffractometers and measurement techniques of SRXRD were developed during the past decade [5, 37]. Very small amounts of electron distributions were successfully observed in  $\text{TiS}_2$  [38] and  $\text{LaB}_6$  [15] using the diffractometers and techniques. The method can be applied to a pure metal system. For this research, we conducted an accurate charge density study of aluminum using state of the art SRXRD. Nakashima et al. shows the criteria for accuracy of structure factors to detect the chemical bonding of aluminum. The error of less than 0.3% in observed structure factors must be accomplished in the present experiment.

We selected aluminum as the sample of the present study as it is an ideal metal to determine the accurate experimental charge density. Ogata et al. reported the high intrinsic stacking fault energy by a theoretical calculation [2]. We can measure the diffraction data without contribution from the stacking fault. In addition, aluminum has a relatively large contribution of valence electrons to diffraction data in the metal. The bonding electron density of aluminum based on the Drude model has the second largest value,  $0.18 \text{ e}/\text{\AA}^3$ , in the typical metals [1]. Aluminum is widely used in industry as aluminum alloy.

### 5.2 Flow of data analysis

The powder profiles were analyzed by the combination of Rietveld refinement and multipole

refinement. The details of the analysis are described in Chapter 4. The observed structure factors were extracted from the 30 K data. The total number of structure factors was 217 which corresponds to a reciprocal resolution of  $\sin \theta / \lambda < 2.31 \text{ \AA}^{-1}$ . We also prepared three sets of theoretical structure factors, two of the three were prepared using the WIEN2k program [20] with two types of exchange parameters, the Perdew–Burke–Ernzerhof generalized gradient approximation (PBE) and local spin density approximation (LSDA). The structure factors from the independent atom model (IAM) were also prepared using the XD2016 program [39]. The reciprocal resolution of these data is the same as that of the experimental data.

Figure 5.1 shows the present static deformation density of (a) WIEN2k PBE and (b) LSDA in (110) plane. The contour interval is from  $-0.1$  to  $0.1 \text{ e/\AA}^3$  with  $0.005 \text{ e/\AA}^3$  step width. Solid and dotted lines show positive and negative contours, respectively. There are aluminum atoms at four corners. Tetrahedral sites have positive charge density maxima. The contour maps are almost identical each other. The charge density at the peak maxima are  $0.03$  and  $0.025 \text{ e/\AA}^3$  for WIEN2k PBE and LSDA. The static deformation density of WIEN2k PBE is almost identical to WIEN2k LSDA. Therefore, the WIEN2k PBE were employed in subsequent sections as the theoretical result.

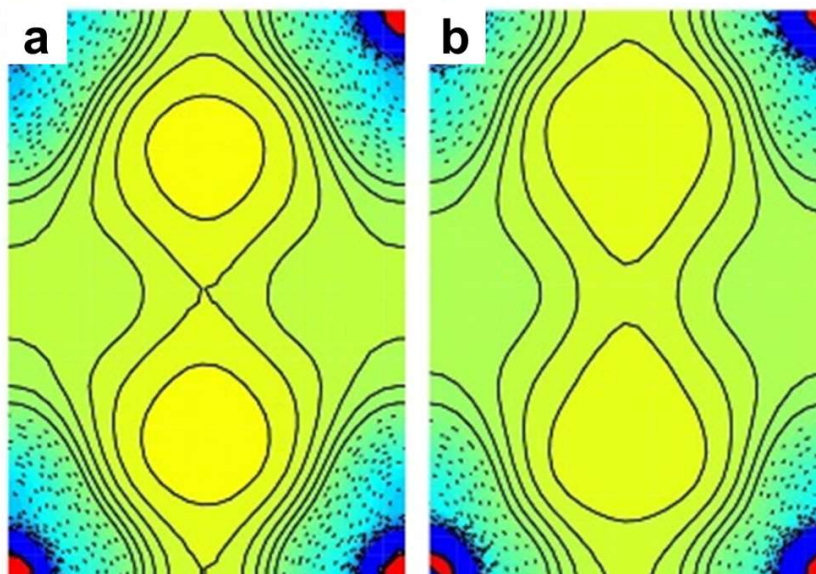


Figure 5.1 The present static deformation density of (a) WIEN2k PBE and (b) LSDA in (110) plane.

### 5.3 Data analysis by Rietveld refinement

Rietveld refinements using the multiple datasets were carried out using the program Synchrotron Powder (SP) [5]. The reciprocal resolution in the analysis correspond to  $\sin \theta / \lambda < 2.31$ ,  $2.15$ ,  $1.77$ , and  $1.62 \text{ \AA}^{-1}$  for 30, 100, 200, and 300 K data. The observed structure factors were initially extracted from the results of the Rietveld refinements based on the IAM. The extraction of the observed structure factors was improved by an iterative procedure of multipole refinement and powder diffraction pattern fitting. The reliability factors based on the weighted profile  $R_{wp}$  of the final pattern fitting were 1.87%, 1.89%, 2.41%, and 2.73% for 30, 100, 200, and 300 K, respectively. The final reliability factors

based on the Bragg intensity  $R_I$  were 2.37%, 2.85%, 3.19%, and 3.13% for 30, 100, 200, and 300 K. The determined lattice constants,  $a$ , isotropic atomic displacement parameter,  $U_{\text{iso}}$ , and their temperature dependences are shown in Table 5.1 and Figure 5.2.

Table 5.1 The results of structural parameters determined by Rietveld refinement.

	30 K	100 K	200 K	300 K
$a$ (Å)	4.03270(1)	4.03318(1)	4.04117(1)	4.04940(1)
$U_{\text{iso}}$ (Å <sup>2</sup> )	0.2284(6)	0.305(1)	0.507(3)	0.731(4)

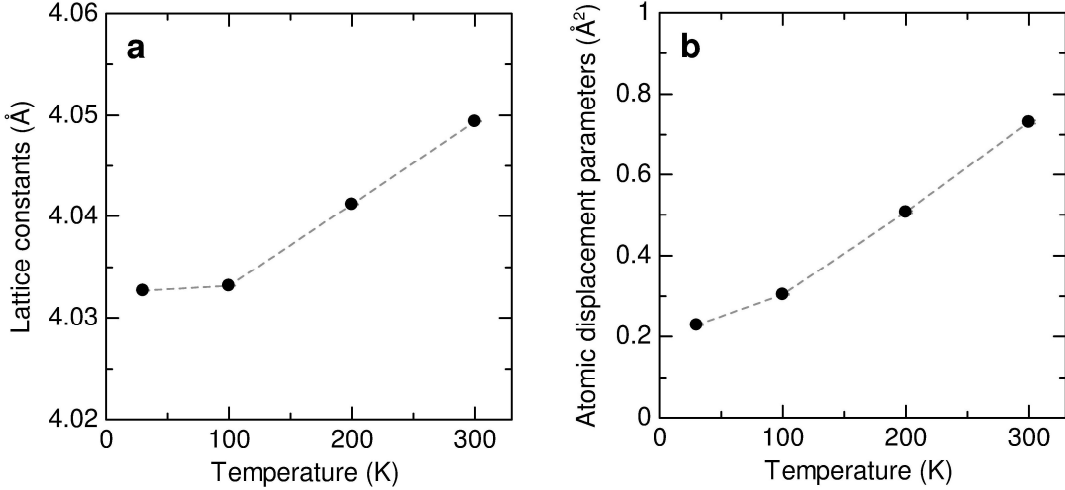


Figure 5.2 Temperature dependences of (a) lattice constants and (b) isotropic atomic displacement parameters.

## 5.4 Theoretical calculation of charge density

Table 5.2 shows the theoretical structure factors  $F$  of aluminum in  $\sin \theta / \lambda < 2.31 \text{ \AA}^{-1}$ . The first principle calculation based on the density functional theory was performed by full potential-linearized augmented plane wave (FP-LAPW) with the generalized gradient approximation (GGA), local orbitals, and local screening potentials in the WIEN2k package [20]. Experimental lattice constants were used for the calculations. We used 1000 k points with a plane-wave cutoff parameter of  $R^{\text{MT}}K_{\text{max}} = 7.0$ . Theoretical structure factors were calculated using the lapw3 program.

## 5.5 Multipole modeling of theoretical structure factors

Table 5.3 shows the multipole parameters by XD2016 [39] for the theoretical structure factors. The extended Hansen-Coppens multipole model including the core deformation term [12] was used for the analysis. The electron configuration of aluminum was  $1s^2 2s^2 2p^6 3s^2 3p^1$  [40]. We set  $1s^2$ ,  $2s^2 + 2p^6$ , and  $3s^2 + 3p^1$  valence electron shells. The local axes for the aluminum atom were parallel to the [100], [010], and [001] directions. The structure factors from the IAM were also prepared using the XD2016 program. The scale factor  $s$ , radial expansion/contraction parameters,  $\kappa_{\text{core}}$  and  $\kappa_{\text{valence}}$ , and hexadecapole parameters,  $H_0$ , were refined in the analysis. There is a relationship between  $H_0$  and  $H_4+$ , where  $H_4+$

$$= 0.74048H_0.$$

Table 5.2 Theoretical structure factors of PBE and LSDA with  $\sin \theta / \lambda < 2.31 \text{ \AA}^{-1}$ .

$h$	$k$	$l$	$\sin \theta / \lambda$	PBE	LSDA	$h$	$k$	$l$	$\sin \theta / \lambda$	PBE	LSDA
1	1	1	0.215	8.86	8.87	10	4	0	1.335	1.65	1.65
2	0	0	0.248	8.38	8.39	10	4	2	1.358	1.62	1.62
2	2	0	0.351	7.30	7.29	7	7	5	1.375	1.60	1.61
3	1	1	0.411	6.64	6.63	11	1	1	1.375	1.60	1.61
2	2	2	0.430	6.45	6.43	8	8	0	1.403	1.58	1.58
4	0	0	0.496	5.73	5.71	9	5	5	1.419	1.56	1.56
3	3	1	0.540	5.27	5.26	9	7	1	1.419	1.56	1.56
4	2	0	0.554	5.13	5.12	11	3	1	1.419	1.56	1.56
4	2	2	0.607	4.64	4.63	10	4	4	1.424	1.55	1.55
3	3	3	0.644	4.32	4.31	8	8	2	1.424	1.55	1.55
5	1	1	0.644	4.32	4.31	8	6	6	1.446	1.53	1.53
4	4	0	0.701	3.87	3.86	10	6	0	1.446	1.53	1.53
5	3	1	0.734	3.64	3.64	9	7	3	1.462	1.52	1.52
4	4	2	0.744	3.57	3.57	11	3	3	1.462	1.52	1.52
6	0	0	0.744	3.57	3.57	10	6	2	1.467	1.51	1.51
6	2	0	0.784	3.32	3.31	8	8	4	1.488	1.50	1.50
5	3	3	0.813	3.15	3.15	12	0	0	1.488	1.50	1.50
6	2	2	0.822	3.10	3.10	7	7	7	1.503	1.48	1.48
4	4	4	0.859	2.91	2.91	11	5	1	1.503	1.48	1.48
5	5	1	0.885	2.79	2.78	12	2	0	1.508	1.48	1.48
7	1	1	0.885	2.79	2.78	10	6	4	1.529	1.46	1.46
6	4	0	0.894	2.75	2.74	12	2	2	1.529	1.46	1.46
6	4	2	0.928	2.60	2.60	9	7	5	1.544	1.45	1.45
5	5	3	0.952	2.51	2.51	11	5	3	1.544	1.45	1.45
7	3	1	0.952	2.51	2.51	12	4	0	1.568	1.43	1.43
8	0	0	0.992	2.37	2.37	9	9	1	1.583	1.42	1.42
7	3	3	1.015	2.29	2.29	8	8	6	1.588	1.42	1.42
6	4	4	1.022	2.27	2.27	10	8	0	1.588	1.42	1.42
8	2	0	1.022	2.27	2.27	12	4	2	1.588	1.42	1.42
6	6	0	1.052	2.18	2.18	10	8	2	1.607	1.41	1.41
8	2	2	1.052	2.18	2.18	9	9	3	1.621	1.40	1.40
5	5	5	1.074	2.13	2.13	11	5	5	1.621	1.40	1.40
7	5	1	1.074	2.13	2.13	11	7	1	1.621	1.40	1.40
6	6	2	1.081	2.11	2.11	13	1	1	1.621	1.40	1.40
8	4	0	1.109	2.04	2.04	10	6	6	1.626	1.39	1.39
7	5	3	1.130	1.99	1.99	12	4	4	1.645	1.38	1.38
9	1	1	1.130	1.99	1.99	9	7	7	1.659	1.37	1.37
8	4	2	1.136	1.98	1.98	11	7	3	1.659	1.37	1.37
6	6	4	1.163	1.92	1.92	13	3	1	1.659	1.37	1.37
9	3	1	1.183	1.88	1.88	10	8	4	1.663	1.37	1.37
8	4	4	1.215	1.83	1.83	12	6	0	1.663	1.37	1.37
7	5	5	1.234	1.79	1.79	12	6	2	1.682	1.36	1.36
7	7	1	1.234	1.79	1.79	9	9	5	1.695	1.35	1.35
9	3	3	1.234	1.79	1.79	13	3	3	1.695	1.35	1.35
8	6	0	1.240	1.78	1.78	8	8	8	1.718	1.34	1.34
10	0	0	1.240	1.78	1.78	11	7	5	1.731	1.33	1.33
8	6	2	1.264	1.75	1.75	13	5	1	1.731	1.33	1.33
10	2	0	1.264	1.75	1.75	12	6	4	1.736	1.33	1.33
7	7	3	1.283	1.72	1.72	14	0	0	1.736	1.33	1.33
9	5	1	1.283	1.72	1.72	10	8	6	1.753	1.32	1.32
6	6	6	1.289	1.71	1.71	10	10	0	1.753	1.32	1.32
10	2	2	1.289	1.71	1.71	14	2	0	1.753	1.32	1.32
9	5	3	1.330	1.66	1.66	11	9	1	1.767	1.31	1.31
8	6	4	1.335	1.65	1.65	13	5	3	1.767	1.31	1.31

10	10	2	1.771	1.31	1.31	11	9	9	2.086	1.16	1.15
14	2	2	1.771	1.31	1.31	15	7	3	2.086	1.16	1.15
12	8	0	1.788	1.30	1.30	12	12	0	2.104	1.15	1.14
9	9	7	1.801	1.29	1.29	16	4	4	2.104	1.15	1.14
11	9	3	1.801	1.29	1.29	11	11	7	2.115	1.14	1.14
12	8	2	1.805	1.29	1.29	13	11	1	2.115	1.14	1.14
14	4	0	1.805	1.29	1.29	17	1	1	2.115	1.14	1.14
10	10	4	1.822	1.28	1.28	12	12	2	2.119	1.14	1.14
12	6	6	1.822	1.28	1.28	16	6	0	2.119	1.14	1.14
14	4	2	1.822	1.28	1.28	14	8	6	2.133	1.13	1.13
11	7	7	1.835	1.27	1.27	16	6	2	2.133	1.13	1.13
13	5	5	1.835	1.27	1.27	14	10	0	2.133	1.13	1.13
13	7	1	1.835	1.27	1.27	13	9	7	2.144	1.13	1.13
12	8	4	1.856	1.26	1.26	13	11	3	2.144	1.13	1.13
11	9	5	1.868	1.26	1.26	15	7	5	2.144	1.13	1.13
13	7	3	1.868	1.26	1.26	17	3	1	2.144	1.13	1.13
15	1	1	1.868	1.26	1.26	10	10	10	2.148	1.13	1.12
10	8	8	1.872	1.26	1.25	14	10	2	2.148	1.13	1.12
14	4	4	1.872	1.26	1.25	12	12	4	2.162	1.12	1.12
14	6	0	1.889	1.25	1.25	15	9	1	2.172	1.12	1.11
15	3	1	1.901	1.24	1.24	17	3	3	2.172	1.12	1.11
10	10	6	1.905	1.24	1.24	12	10	8	2.176	1.11	1.11
14	6	2	1.905	1.24	1.24	16	6	4	2.176	1.11	1.11
9	9	9	1.933	1.23	1.22	14	10	4	2.190	1.11	1.10
13	7	5	1.933	1.23	1.22	13	11	5	2.201	1.10	1.10
11	11	1	1.933	1.23	1.22	15	9	3	2.201	1.10	1.10
15	3	3	1.933	1.23	1.22	17	5	1	2.201	1.10	1.10
12	8	6	1.937	1.22	1.22	16	8	0	2.218	1.10	1.09
12	10	0	1.937	1.22	1.22	11	11	9	2.228	1.09	1.09
12	10	2	1.953	1.22	1.21	15	7	7	2.228	1.09	1.09
14	6	4	1.953	1.22	1.21	17	5	3	2.228	1.09	1.09
11	9	7	1.964	1.21	1.21	12	12	6	2.232	1.09	1.09
11	11	3	1.964	1.21	1.21	14	8	8	2.232	1.09	1.09
13	9	1	1.964	1.21	1.21	16	8	2	2.232	1.09	1.09
15	5	1	1.964	1.21	1.21	18	0	0	2.232	1.09	1.09
16	0	0	1.984	1.20	1.20	16	6	6	2.245	1.08	1.08
13	9	3	1.995	1.20	1.19	18	2	0	2.245	1.08	1.08
15	5	3	1.995	1.20	1.19	13	9	9	2.256	1.08	1.08
12	10	4	1.999	1.19	1.19	15	9	5	2.256	1.08	1.08
14	8	0	1.999	1.19	1.19	14	10	6	2.259	1.08	1.07
16	2	0	1.999	1.19	1.19	18	2	2	2.259	1.08	1.07
10	10	8	2.015	1.19	1.18	16	8	4	2.273	1.07	1.07
14	8	2	2.015	1.19	1.18	13	11	7	2.283	1.07	1.06
16	2	2	2.015	1.19	1.18	17	5	5	2.283	1.07	1.06
11	11	5	2.026	1.18	1.18	13	13	1	2.283	1.07	1.06
13	7	7	2.026	1.18	1.18	17	7	1	2.283	1.07	1.06
14	6	6	2.030	1.18	1.18	14	12	0	2.286	1.07	1.06
12	8	8	2.045	1.17	1.17	18	4	0	2.286	1.07	1.06
16	4	0	2.045	1.17	1.17	12	10	10	2.300	1.06	1.06
13	9	5	2.056	1.17	1.17	14	12	2	2.300	1.06	1.06
15	5	5	2.056	1.17	1.17	18	4	2	2.300	1.06	1.06
15	7	1	2.056	1.17	1.17	13	13	3	2.310	1.06	1.05
14	8	4	2.060	1.17	1.16	17	7	3	2.310	1.06	1.05
16	4	2	2.060	1.17	1.16	15	11	1	2.310	1.06	1.05
12	10	6	2.075	1.16	1.16						

Table 5.3 Multipole parameters for the theoretical structure factors of PBE, LSDA, and the experimental structure factors at 30 K.

	PBE	LSDA	30 K
$R_F / R_{wF}$ (%)	0.08 / 0.1	0.1 / 0.11	1.97 / 1.27
GOF	0.1270	0.1412	1.3321
Scale	0.75	0.75	1.006(1)
$\kappa$ (1s)	0.9848(8)	0.9746(9)	0.9848
$\kappa$ (2s2p)	1.0010(3)	0.9983(3)	1.0010
$\kappa$ (3s3p)	0.943(2)	0.960(2)	0.95(2)
H0	-0.00079(4)	-0.00075(5)	-0.0017(5)
H4+	-0.00062(3)	-0.00059(4)	-0.0013(4)

## 5.6 The estimation of first-order thermal diffuse scattering in diffraction data

Figure 5.3(a) shows the calculated first-order thermal diffuse scattering in the powder X-ray diffraction of aluminum for 30, 100, 200, and 300 K. The horizontal axis is diffraction angle  $2\theta$ . The thermal diffuse scattering intensity were calculated from Herstein's equation [36] with the isotropic atomic displacement parameters for each temperature. Incident X-ray wavelengths and lattice constants were fixed to the results of 30 K owing to an alignment of the intensities in the diffraction angle  $2\theta$ . The intensities of the thermal diffuse scattering at 30 K are dramatically smaller than those at 300 K.

Figure 5.3(b) shows the first-order thermal diffuse scattering for 30 and 300 K together with intensity baselines colored by blue and green, respectively. Figure 5.3(c) shows the modulations of the calculated first-order thermal diffuse scattering from the baselines. The horizontal axis is diffraction angle  $2\theta$ . The Purple and red lines represent the modulations of 30 and 300 K. The modulation at 30 K is approximately 10 times smaller than that at 300 K.

Table. 5.4 shows the estimations of the scale factors between the theoretical and experimental first-order thermal diffuse scattering at several measurement points. The 100 and 300 K data were used for the estimation owing to the same experimental conditions. Figure 5.4 shows the 1-D diffraction data at 100 and 300 K. The temperature dependent variations of the background intensities between 100 and 300 K were regarded as the first-order thermal diffuse scattering intensities. Figure 5.5 shows the first-order thermal diffuse scattering patterns for 100 and 300 K. We used some minimum points between the Bragg positions, labeled by 1 ~ 23 in figure 5.5 up to  $2\theta = 40^\circ$ . The differences between the 100 and 300 K in the calculation pattern and the measurement data at the labeled positions were estimated. The derived average scale factor is  $\sim 230$ . The temperature dependent variation is approximately 1000 counts between 100 and 300 K. The maximum modulation at the Bragg peak in the 30 K data is less than 500 counts. The ratio of the thermal diffuse scattering intensity to the Bragg peak intensity is less than 0.001 at 30 K. We ignored thermal diffuse scattering based on this estimation.

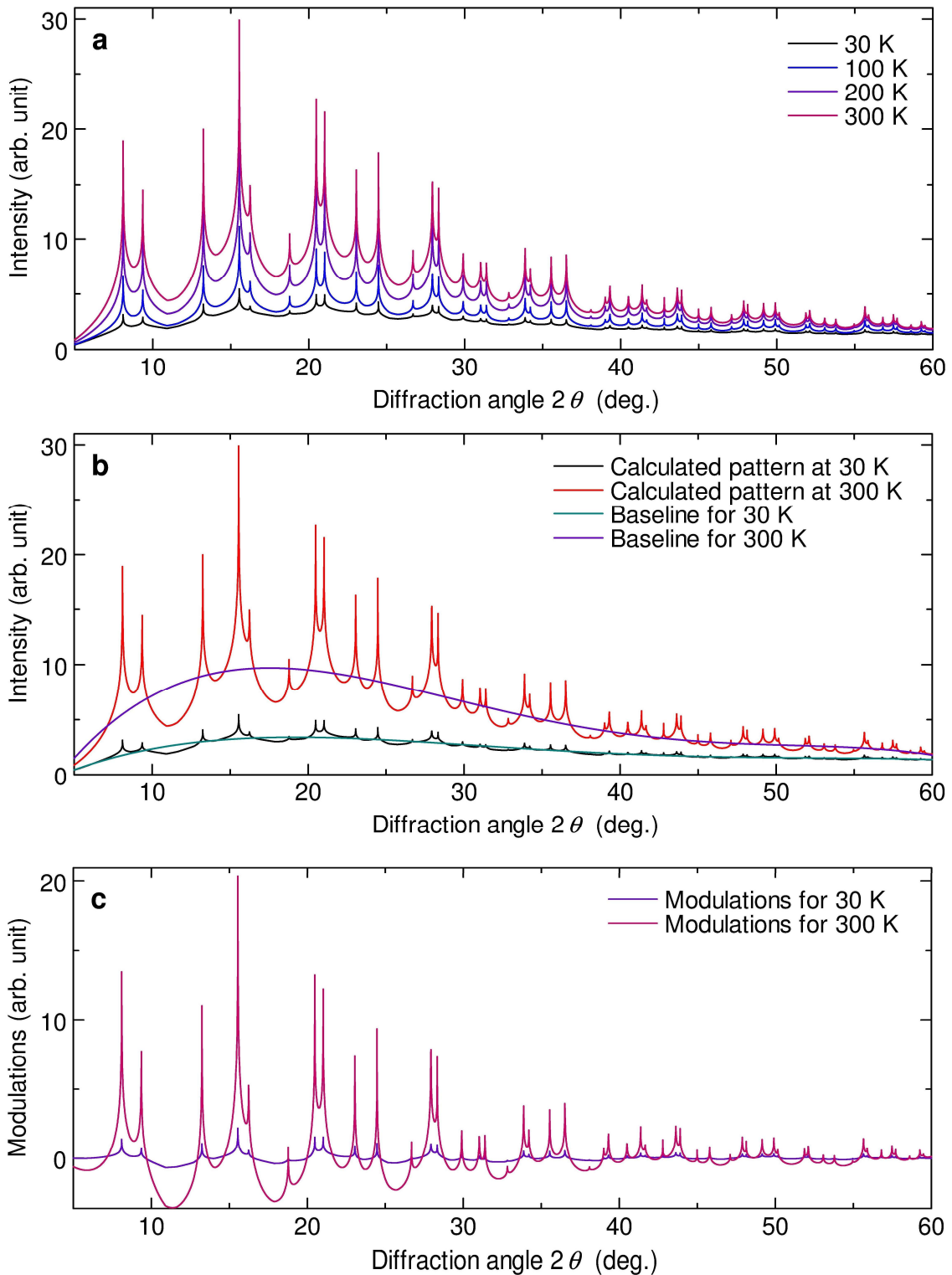


Figure 5.3 The first order thermal diffuse scattering and structure factor modulations of aluminum. (a) The first order thermal diffuse scattering of aluminum for 30, 100, 200, 300 K based on Herbstein's equation. (b) The first order thermal diffuse scattering of aluminum at 30 and 300 K together with purple and green guided spline curves. (c) The modulations of calculated first order thermal diffuse scattering from the baselines.

Table 5.4 The intensity differences between 100 and 300 K in calculation pattern  $\sigma_{\text{calc}}$ , The difference in measurement data  $\sigma_{\text{exp}}$ , and estimated scale factors of first order thermal diffuse scattering intensities

$\sigma_{\text{exp}}/\sigma_{\text{calc}}$	1	2	3	4	5	6	7	8	9	10	11	12
$\sigma_{\text{calc}}$	4.45	2.27	4.72	7.01	3.23	3.93	7.29	4.24	3.98	2.68	3.38	5.15
$\sigma_{\text{exp}}$	763	372	1270	1661	938	899	1660	1060	1040	728	716	975
$\sigma_{\text{exp}}/\sigma_{\text{calc}}$	171	164	269	237	290	229	227	250	261	272	212	189
	13	14	15	16	17	18	19	20	21	22	23	
$\sigma_{\text{calc}}$	2.82	2.54	2.88	1.82	1.98	2.83	2.08	2.18	1.24	1.24	1.71	
$\sigma_{\text{exp}}$	766	618	519	507	482	444	507	494	358	321	272	
$\sigma_{\text{exp}}/\sigma_{\text{calc}}$	272	244	180	279	244	157	244	227	289	260	159	

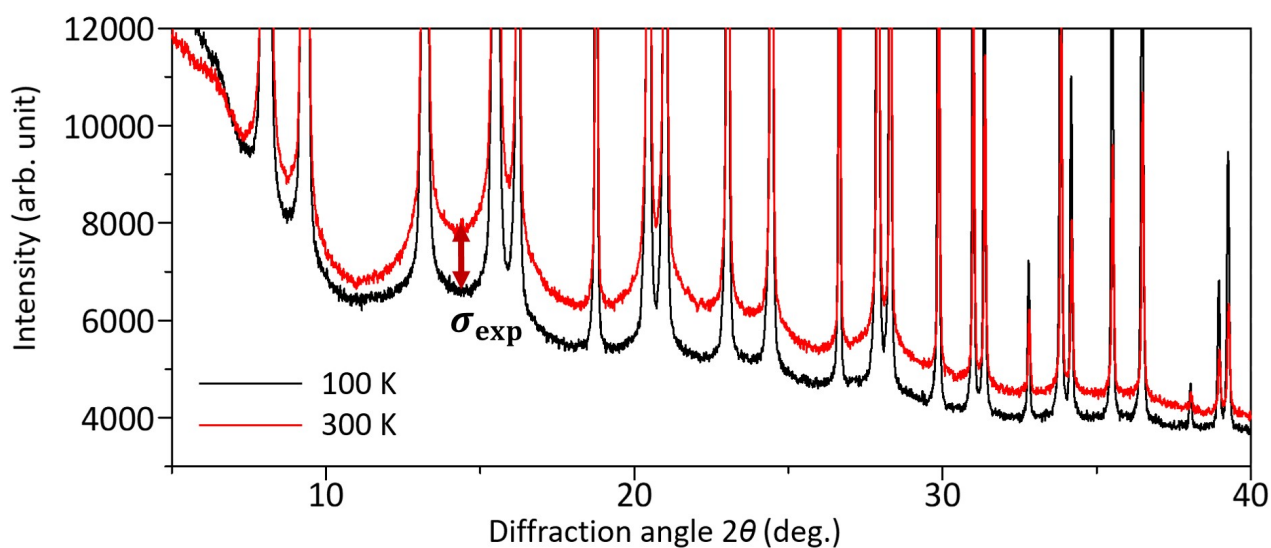


Fig. 5.4 The 1-dimensional diffraction data at 100 and 300 K.

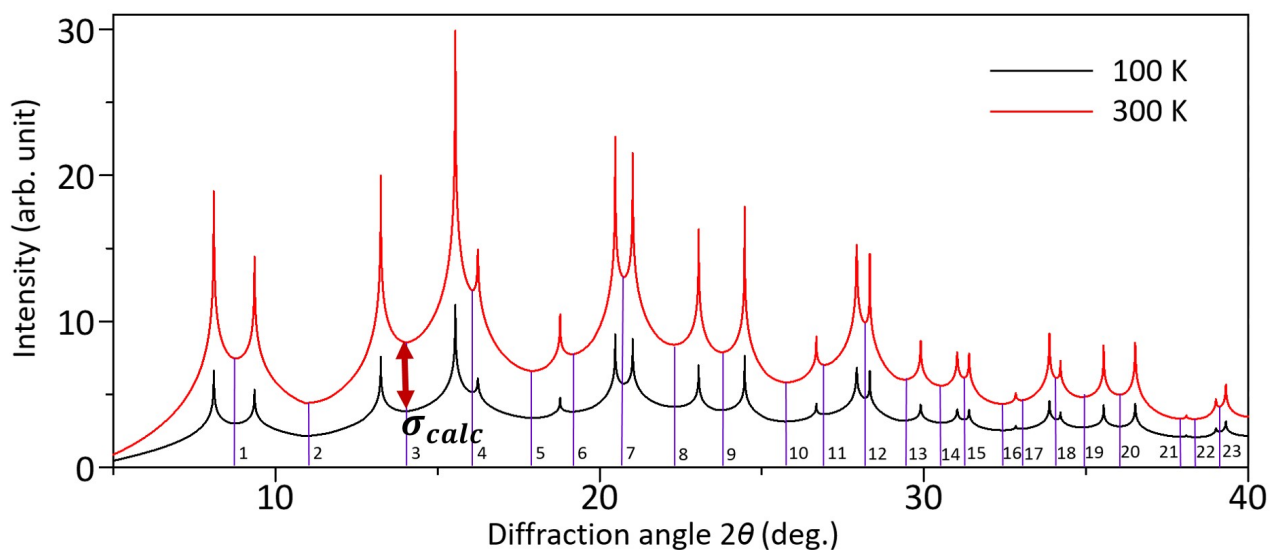


Fig. 5.5 The first order thermal diffuse scattering patterns for 100 and 300 K with labeled minimum points in  $2\theta = 0\sim 40^\circ$ .

## 5.7 The estimation of anharmonic thermal vibration

Figure 5.6 shows the temperature dependence of the anharmonic thermal parameters by the XD2016 [39] for 30, 100, 200, and 300 K. The anisotropic atomic displacement parameters,  $U_{11} = U_{22} = U_{33}$ , and the anharmonic thermal parameters,  $D_{1111} = D_{2222} = D_{3333}$  and  $D_{1122} = D_{2233} = D_{1133}$ , were refined in the analyses. The reliability factors of the multipole refinements  $R_F$  were 1.98%, 1.85%, 2.49%, and 2.59% for 30, 100, 200, and 300 K, respectively. The  $D_{1111}$  at less than 200 K was negative indicating no anharmonic thermal vibration below 200 K. The order of  $D_{1111}$  and  $D_{1122}$  at 30 K was less than the order of 1/1000 of the harmonic thermal vibration parameter  $U_{\text{iso}}$ . For this reason, the anharmonic thermal vibration was ignored at 30 K.

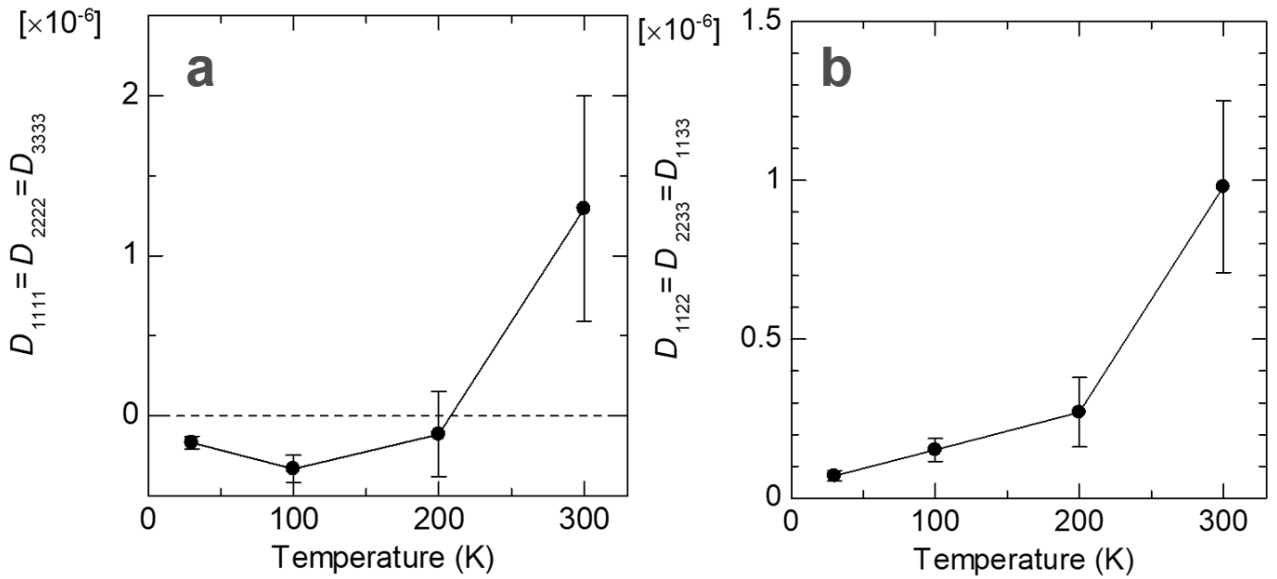


Figure 5.6 The temperature dependence of anharmonic thermal parameters (a)  $D_{1111}$  and (b)  $D_{1122}$  for experimental 30, 100, 200, and 300 K data.

## 5.8 Extraction of experimental structure factors with multipole model

We performed multipole refinement of the observed structure factors extracted from the results of the Rietveld refinement. The multipole refinement updated the calculated structure factors. The intensity ratio of the completely overlapped Bragg reflections changed with the multipole refinement. The observed structure factor values of completely overlapping diffraction peaks were redistributed by pattern fitting of powder diffraction using structure factors obtained from multipole refinement. The iterative procedure of the multipole refinement and pattern fitting was conducted 10 times until all the parameters were converged within standard uncertainty. The final observed structure factors at 30 K are listed in Table 5.5. The low order structure factor have the error rate of less than 0.3%.

The experimental multipole parameters are shown in Table 5.3. The radial expansion/contraction parameters of  $3s^23p^1$  fitted to theoretical structure factors were employed for the initial parameter of the multipole modeling. The extended Hansen-Coppens multipole model, including

the core deformation term, was used for the analysis. The scale factor,  $s$ , radial expansion/contraction parameters of  $3s^23p^1$ ,  $\kappa_{\text{valence}}$ , anisotropic atomic displacement parameters,  $U_{11} = U_{22} = U_{33}$ , and the multipole parameters, H0, were refined in the analyses. The radial expansion/contraction parameters of the inner core electrons  $1s^2$  and  $2s^22p^6$  were fixed to theoretical values.

Table 5.5 The final observed structure factors of aluminum at 30 K.

$h$	$k$	$l$	$\sin \theta/\lambda$	30 K	$h$	$k$	$l$	$\sin \theta/\lambda$	30 K
1	1	1	0.215	8.91(1)	10	4	0	1.335	1.62(3)
2	0	0	0.248	8.36(1)	10	4	2	1.358	1.61(2)
2	2	0	0.351	7.30(1)	7	7	5	1.375	1.59(3)
3	1	1	0.411	6.62(1)	11	1	1	1.375	1.59(3)
2	2	2	0.430	6.48(1)	8	8	0	1.403	1.67(4)
4	0	0	0.496	5.75(2)	9	5	5	1.419	1.54(3)
3	3	1	0.540	5.23(1)	9	7	1	1.419	1.54(2)
4	2	0	0.554	5.14(1)	11	3	1	1.419	1.54(2)
4	2	2	0.607	4.64(1)	10	4	4	1.424	1.54(3)
3	3	3	0.644	4.35(2)	8	8	2	1.424	1.54(3)
5	1	1	0.644	4.34(1)	8	6	6	1.446	1.52(3)
4	4	0	0.701	3.93(2)	10	6	0	1.446	1.52(3)
5	3	1	0.734	3.63(1)	9	7	3	1.462	1.48(2)
4	4	2	0.744	3.58(1)	11	3	3	1.462	1.48(3)
6	0	0	0.744	3.56(2)	10	6	2	1.467	1.48(2)
6	2	0	0.784	3.28(1)	8	8	4	1.488	1.49(3)
5	3	3	0.813	3.12(1)	12	0	0	1.488	1.49(7)
6	2	2	0.822	3.04(1)	7	7	7	1.503	1.46(6)
4	4	4	0.859	2.91(3)	11	5	1	1.503	1.47(2)
5	5	1	0.885	2.77(2)	12	2	0	1.508	1.43(3)
7	1	1	0.885	2.77(2)	10	6	4	1.529	1.44(2)
6	4	0	0.894	2.72(2)	12	2	2	1.529	1.44(4)
6	4	2	0.928	2.58(1)	9	7	5	1.544	1.45(3)
5	5	3	0.952	2.49(2)	11	5	3	1.544	1.45(3)
7	3	1	0.952	2.49(1)	12	4	0	1.568	1.48(4)
8	0	0	0.992	2.36(4)	9	9	1	1.583	1.46(4)
7	3	3	1.015	2.25(2)	8	8	6	1.588	1.42(4)
6	4	4	1.022	2.22(2)	10	8	0	1.588	1.42(4)
8	2	0	1.022	2.22(2)	12	4	2	1.588	1.42(3)
6	6	0	1.052	2.15(3)	10	8	2	1.607	1.45(3)
8	2	2	1.052	2.15(2)	9	9	3	1.621	1.36(4)
5	5	5	1.074	2.09(3)	11	5	5	1.621	1.36(4)
7	5	1	1.074	2.10(1)	11	7	1	1.621	1.37(3)
6	6	2	1.081	2.05(2)	13	1	1	1.621	1.36(4)
8	4	0	1.109	2.09(2)	10	6	6	1.626	1.41(4)
7	5	3	1.130	1.97(2)	12	4	4	1.645	1.44(4)
9	1	1	1.130	1.97(2)	9	7	7	1.659	1.32(4)
8	4	2	1.136	1.96(2)	11	7	3	1.659	1.33(3)
6	6	4	1.163	1.95(2)	13	3	1	1.659	1.33(3)
9	3	1	1.183	1.89(2)	10	8	4	1.663	1.32(3)
8	4	4	1.215	1.84(2)	12	6	0	1.663	1.32(4)
7	5	5	1.234	1.77(2)	12	6	2	1.682	1.33(3)
7	7	1	1.234	1.76(2)	9	9	5	1.695	1.44(4)
9	3	3	1.234	1.76(2)	13	3	3	1.695	1.44(4)
8	6	0	1.240	1.75(2)	8	8	8	1.718	1.67(8)
10	0	0	1.240	1.75(5)	11	7	5	1.731	1.30(3)
8	6	2	1.264	1.73(2)	13	5	1	1.731	1.30(3)
10	2	0	1.264	1.73(3)	12	6	4	1.736	1.30(3)
7	7	3	1.283	1.70(3)	14	0	0	1.736	1.28(9)
9	5	1	1.283	1.70(2)	10	8	6	1.753	1.28(3)
6	6	6	1.289	1.67(5)	10	10	0	1.753	1.27(7)
10	2	2	1.289	1.68(3)	14	2	0	1.753	1.28(5)
9	5	3	1.330	1.66(2)	11	9	1	1.767	1.25(3)
8	6	4	1.335	1.62(2)	13	5	3	1.767	1.25(3)

10	10	2	1.771	1.29(5)	11	9	9	2.086	1.20(7)
14	2	2	1.771	1.29(5)	15	7	3	2.086	1.21(5)
12	8	0	1.788	1.35(5)	12	12	0	2.104	1.2(1)
9	9	7	1.801	1.25(5)	16	4	4	2.104	1.22(7)
11	9	3	1.801	1.25(3)	11	11	7	2.115	0.95(7)
12	8	2	1.805	1.27(4)	13	11	1	2.115	0.96(5)
14	4	0	1.805	1.27(5)	17	1	1	2.115	0.95(7)
10	10	4	1.822	1.28(5)	12	12	2	2.119	1.02(7)
12	6	6	1.822	1.28(5)	16	6	0	2.119	1.02(7)
14	4	2	1.822	1.28(4)	14	8	6	2.133	1.07(5)
11	7	7	1.835	1.21(5)	16	6	2	2.133	1.07(5)
13	5	5	1.835	1.21(5)	14	10	0	2.133	1.06(7)
13	7	1	1.835	1.22(4)	13	9	7	2.144	1.09(5)
12	8	4	1.856	1.22(4)	13	11	3	2.144	1.09(5)
11	9	5	1.868	1.23(4)	15	7	5	2.144	1.09(5)
13	7	3	1.868	1.23(4)	17	3	1	2.144	1.09(5)
15	1	1	1.868	1.22(5)	10	10	10	2.148	1.2(1)
10	8	8	1.872	1.27(5)	14	10	2	2.148	1.25(5)
14	4	4	1.872	1.27(5)	12	12	4	2.162	1.67(8)
14	6	0	1.889	1.32(5)	15	9	1	2.172	1.14(5)
15	3	1	1.901	1.20(4)	17	3	3	2.172	1.14(8)
10	10	6	1.905	1.26(6)	12	10	8	2.176	1.19(6)
14	6	2	1.905	1.27(4)	16	6	4	2.176	1.19(6)
9	9	9	1.933	1.3(1)	14	10	4	2.190	1.18(6)
13	7	5	1.933	1.28(4)	13	11	5	2.201	1.02(6)
11	11	1	1.933	1.27(6)	15	9	3	2.201	1.02(6)
15	3	3	1.933	1.27(6)	17	5	1	2.201	1.02(6)
12	8	6	1.937	1.31(4)	16	8	0	2.218	1.06(8)
12	10	0	1.937	1.30(6)	11	11	9	2.228	0.96(8)
12	10	2	1.953	1.18(4)	15	7	7	2.228	0.96(8)
14	6	4	1.953	1.18(4)	17	5	3	2.228	0.97(6)
11	9	7	1.964	1.18(4)	12	12	6	2.232	1.06(8)
11	11	3	1.964	1.16(6)	14	8	8	2.232	1.06(8)
13	9	1	1.964	1.18(4)	16	8	2	2.232	1.07(6)
15	5	1	1.964	1.18(4)	18	0	0	2.232	1.1(2)
16	0	0	1.984	1.7(1)	16	6	6	2.245	1.26(8)
13	9	3	1.995	1.11(4)	18	2	0	2.245	1.26(8)
15	5	3	1.995	1.11(4)	13	9	9	2.256	1.13(9)
12	10	4	1.999	1.18(4)	15	9	5	2.256	1.13(6)
14	8	0	1.999	1.17(6)	14	10	6	2.259	1.18(6)
16	2	0	1.999	1.17(6)	18	2	2	2.259	1.18(9)
10	10	8	2.015	1.15(6)	16	8	4	2.273	1.18(6)
14	8	2	2.015	1.16(5)	13	11	7	2.283	0.99(6)
16	2	2	2.015	1.15(6)	17	5	5	2.283	0.99(9)
11	11	5	2.026	1.29(6)	13	13	1	2.283	0.99(9)
13	7	7	2.026	1.29(6)	17	7	1	2.283	0.99(6)
14	6	6	2.030	1.39(7)	14	12	0	2.286	1.16(9)
12	8	8	2.045	1.29(7)	18	4	0	2.286	1.16(9)
16	4	0	2.045	1.29(7)	12	10	10	2.300	1.08(9)
13	9	5	2.056	1.07(5)	14	12	2	2.300	1.08(6)
15	5	5	2.056	1.06(7)	18	4	2	2.300	1.08(6)
15	7	1	2.056	1.07(5)	13	13	3	2.310	0.88(9)
14	8	4	2.060	1.15(5)	17	7	3	2.310	0.88(6)
16	4	2	2.060	1.15(5)	15	11	1	2.310	0.88(6)
12	10	6	2.075	1.23(5)					

## 5.9 Comparison of structure factor sets: Experimental, theoretical, reported sets

Figure 5.7(a) shows plots of the modulations of structure factors  ${}^nF_{hkl}$  for the present experimental data and theoretical values. The modulations in the lowest three reflections  ${}^nF_{111}$ ,  ${}^nF_{200}$ ,  ${}^nF_{220}$  of the experimental data are almost identical to those of the theoretical values. The plot of modulations after the fourth reflection in the theoretical data are almost flat, whereas the experimental data after the fourth reflection still has some fluctuation. Figure 5.7(b) shows the modulations of reported theoretical data in the literatures [42-50]. The modulations of the tight-binding approximation [41] shows similar fluctuations to the experimental data including after the fourth reflection.

Many sets of observed structure factors for aluminum have been reported so far. Figure 5.7(c) shows the plot of their observations [16, 23-29]. The first three reflections of the QCBED data show similar modulation to the present experiment and theoretical calculations. The others cannot recognize the modulations from their  ${}^nF_{111}$ . These can be regarded as unity within experimental errors. Aluminum is one of the ideal metals to determine the accurate experimental charge density owing to a relatively high valence electron ratio. The present study shows the precisions of the QCBED and state of the art SRXRD are required to detect the charge density modulation from the IAM.

Figure 5.8(a) shows plots of the relative ratio of the structure factors to the IAM for the multipole model and experimental data. The deviations of both the first three and after the fourth were clearly expressed by the multipole model. Figure 5.8(b) shows plots of the relative ratio of the structure factors to the IAM for the multipole model and theoretical structure factors. The deviations of the first three were well represented by the multipole model. Small deviations were found after the fourth for the multipole model. The multipole mode is an expansion using atom-centered spherical harmonics. The model can well express the charge density by the combining the atomic wave function such as the tight-binding method. The deviations after the fourth reflection in the experimental data indicate that the charge density of aluminum has a tight-binding like character.

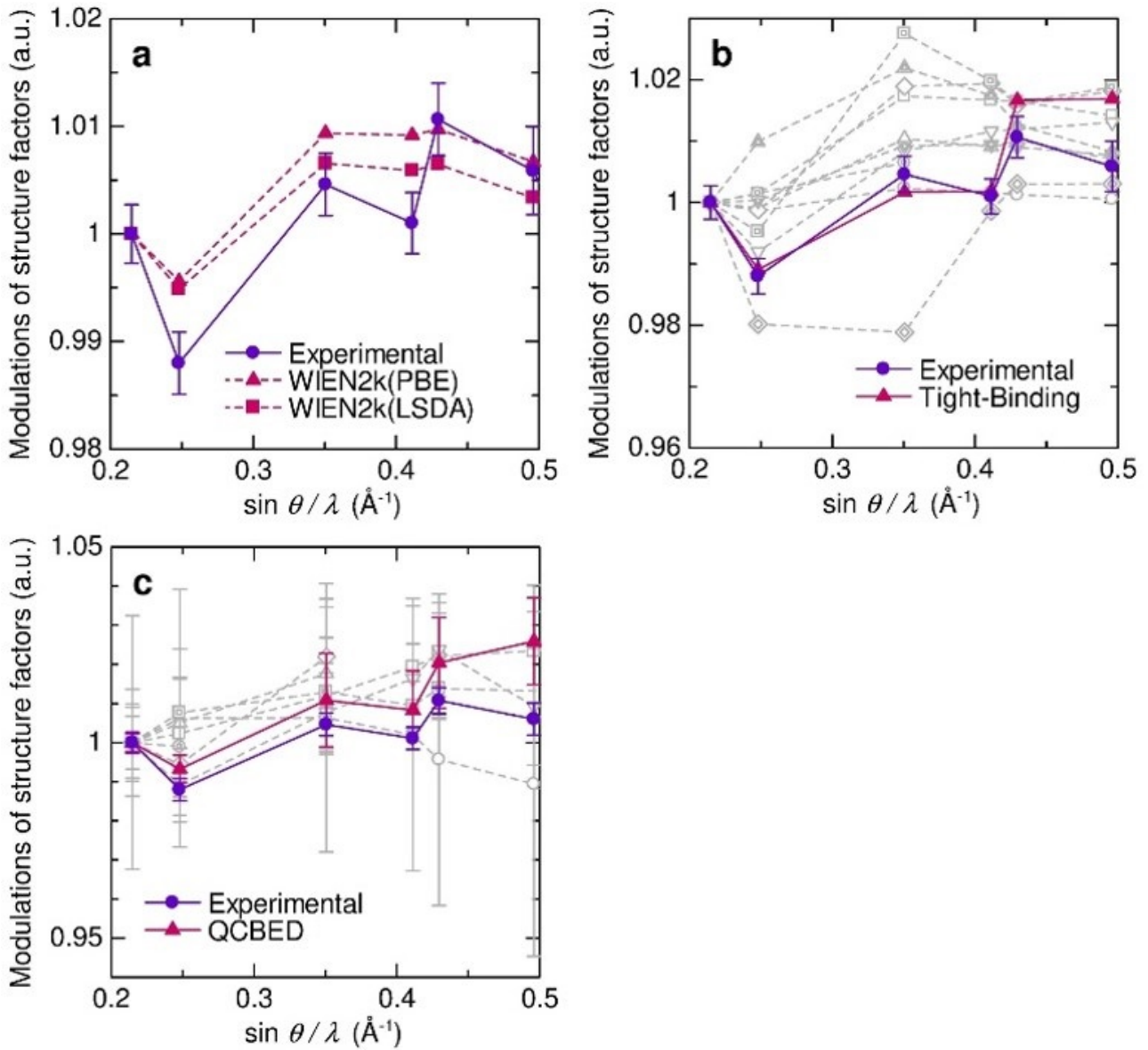


Figure 5.7 Relative ratio of structure factors to IAM normalized by 111 reflection. Horizontal axis is reciprocal resolution  $\sin \theta / \lambda$ . (a) The present experimental and theoretical values. (b) Reported theoretical values and the present experimental values. Gray lines, which represent the reported theoretical values in Ref. [42-50], show no agreement with the present experimental values. (c) Reported experimental values in Ref. [16, 23-29] and the present experimental values. Gray lines have no significant deviation from 111.

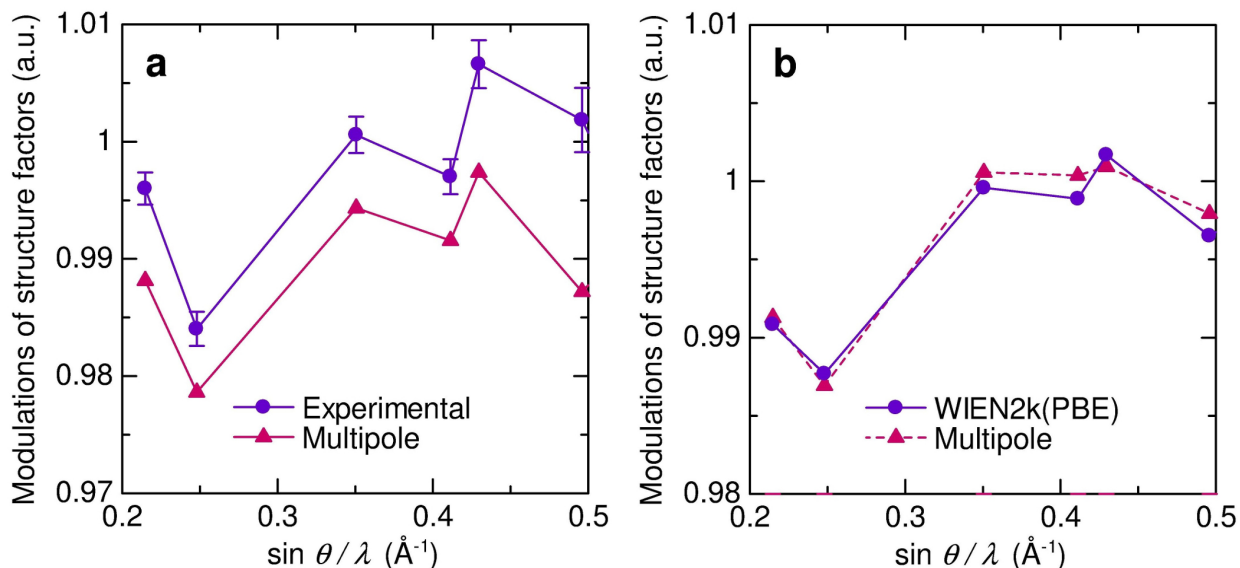


Figure 5.8 Relative ratio of structure factors to IAM. Horizontal axis is reciprocal resolution  $\sin \theta/\lambda$ . (a) The present experimental and multipole model values. (b) The present theoretical and multipole model values.

## 5.10 Static deformation densities

The charge density distribution of aluminum was determined by the multipole refinement of the experimental and theoretical structure factors. A multipole model including core electron deformation terms was used in the analysis. The reliability factors of multiple refinements were 1.97%, 0.08%, and 0.10% for the experimental data, WIEN2k PBE, and WIEN2k LSDA, respectively. We used the results of WIEN2k PBE in the following discussions.

Figure 5.9(a,b) show the experimental and theoretical static deformation density of the (110) plane. The deformation density shows maxima at the center of the tetrahedral site, which is consistent with the previous study [6]. Figure 5.9(c,d) also show the 1-D charge density along lines on the deformation density map. The charge densities at the peak maxima are  $0.04$  and  $0.03$   $e/\text{\AA}^3$  for the experiment and WIEN2k PBE, respectively. The number of electrons in the peaks are  $\sim 0.06$  e and  $\sim 0.03$  e for the experiment and WIEN2k, respectively. Very small amount of accumulation was successfully observed from SRXRD. Wide spread electrons in the left-right direction were found, as shown in Figure 5.9(b). The charge density at the octahedral site of the experiment is  $0.01$   $e/\text{\AA}^3$  smaller than those of WIEN2k.

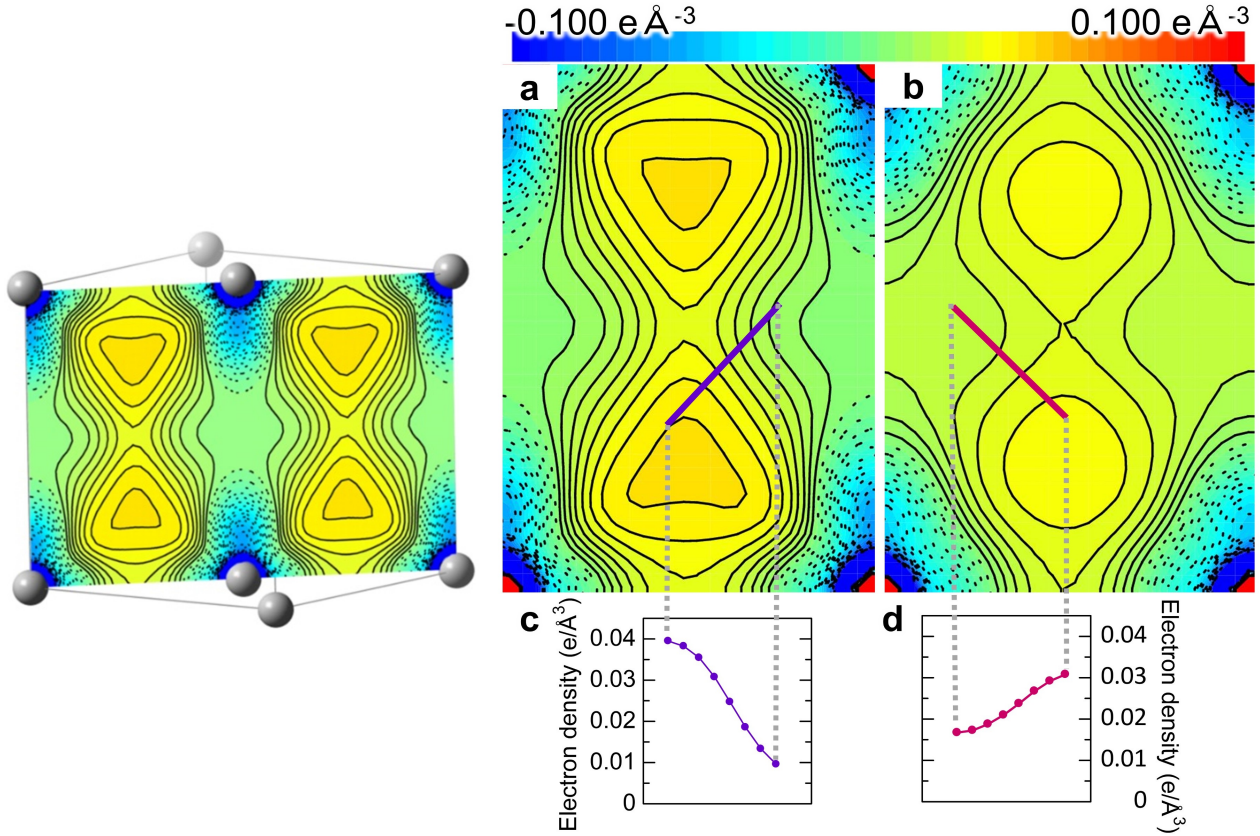


Figure 5.9 Static deformation density of (110) plane. The present experimental (a) and theoretical deformation density (b). The drawing (110) plane is shown in the upper inset. Aluminum atoms are at four corners. The contour interval is  $0.005 \text{ e}/\text{\AA}^3$  in  $-0.1\sim 0.1 \text{ e}/\text{\AA}^3$  region. Solid and dotted lines show positive and negative contours, respectively. (c,d) Electron density values along purple and red solid line in (a) and (b), respectively.

## 5.11 Discussion

Nakashima et al. reported that tetrahedrally centered interatomic bonding could connect Young's coefficients of aluminum [6]. The bonding observed in the present study is also the strongest along [111] and the weakest along [100] among the [100], [110], and [111] directions. Young's modulus,  $E_{uvw}$ , is proportional to  $\Delta\rho$ ,  $E_{100} < E_{110} < E_{111}$ . These facts are also consistent with the present study. The charge density of the experiment is more localized at the center of the tetrahedral than that of the theoretical result. This fact is also consistent with the result of the QCBED.

The previous QCBED study did not describe an origin of the higher charge density than that of theory at tetrahedral site. The present result also shows the higher charge density than the theoretical one. To reveal the origin of the density, we made a charge-density difference between the experiment and theory. Figure 5.10 shows the map of the charge-density difference. Peaks can be seen around atomic sites similar to an atomic orbital. This fact suggests that the deviation of the structure factors after the fourth reflections, as in Figure 5.7(b), indicates the existence of an isolated atomic like orbital. Superposition of the wave functions for the isolated atoms located at each atomic site was used in the tight-binding model. The present result indicates that the charge density of aluminum has a small amount of tight binding-like character supported by Figures 5.7(a), 5.8(a), and 5.10. This fact provides

a new view of the metallic bonding of aluminum, as the nearly free electron model is considered as a good approximation. In addition, the structure factors after the fourth reflection were required to reveal the tight-binding like feature that has not yet been observed with sufficient accuracy so far. The QCBED method can measure extremely accurate low order structure factors. The disadvantage of the method is the presence of a blind region. The advantage of SRXRD is to measure a full resolution dataset.

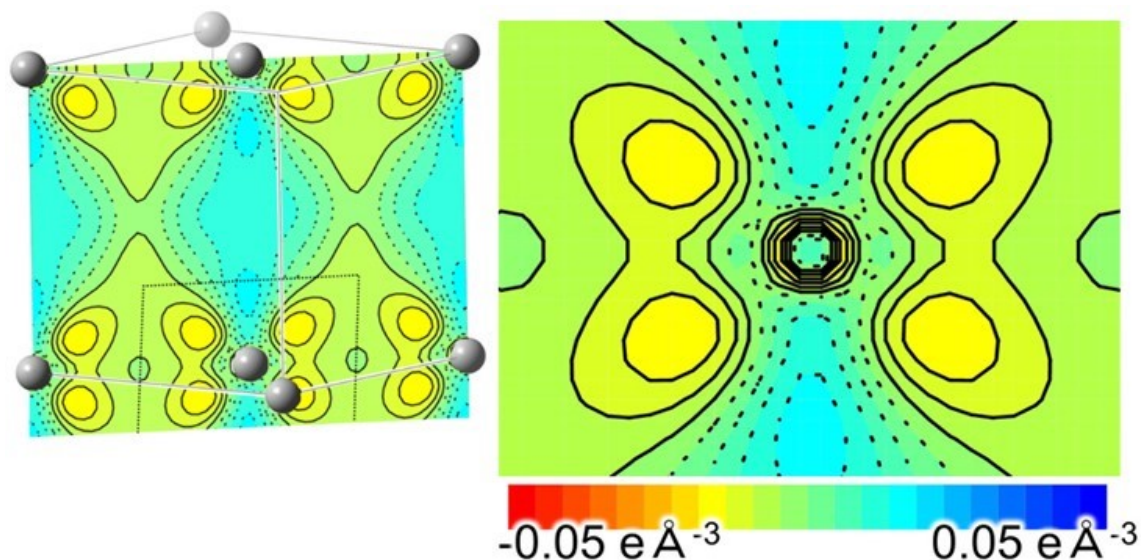


Figure 5.10 Charge-density difference between experiment and theory. The drawing plane is indicating in the left inset inside black dotted line. Aluminum atom is at the center of the plane. The contour interval is  $0.005 \text{ e}/\text{\AA}^3$  in  $-0.05 \sim 0.05 \text{ e}/\text{\AA}^3$  region. Solid and dotted lines show positive and negative contours, respectively.

Aluminum alloys, in which aluminum is the predominant metal, are widely used in the industrial applications of many fields. A quantitatively estimation of the change of chemical bonding for doping will provide the most important knowledge to design, develop, and synthesize a high-performance aluminum alloy. It is difficult to estimate the change from the theoretical calculation as the treatment of dopant is not an easy task for theoretical study. An X-ray charge density study can be applied to the alloys. A high resolution charge density study of aluminum alloy will improve the manufacture process of aluminum alloy.

Currently, third generation SR facilities can be used in almost every advanced country. A similar quality of SRXRD can be measured elsewhere in the world. The charge density distribution in a material is crucial to understand its properties based on quantum mechanics. X-ray charge density is the most information rich observable in natural science. The technique used in the present study can be applied to many types of metals. We will perform charge density studies of metals using the present technique. The correlations between the mechanical properties and the charge density of metals will be revealed in the near future.

## 5.12 Summary

217 structure factors of aluminum were successfully extracted. The lowest-order two structure factors have the same degree of error as that of QCBED which has a high accuracy in the lower order. The error of the structure factors, except for the two mentioned, are one order of magnitude smaller than previous results. Experimental structure factors have modulation from the independent atom model up to the eighth. The modulation in calculation is up to the third. From the comparison with the modulation of past observed structure factors, the mismatch of the reported electron distributions of aluminum is caused by a large error of the structure factors. An accurate observation of the electron distribution of aluminum requires less than 0.4% errors of the structure factors in  $\sin \theta/\lambda < 0.83 \text{ \AA}^{-1}$ . The modulation of experimental structure factors is consistent with the calculated set by the tight-binding approximation.

The static deformation density of aluminum was successfully observed. The positive density peak at the tetrahedral site arose from the modulation of the lowest order two structure factors. The difference in the static deformation density between the experiment and theoretical calculation is due to the difference in modulation after the fourth structure factors. This difference causes an atomic orbital like electron distribution around the atoms in the electron density difference between the experiment and calculation. From the agreement with the modulation calculated by the tight binding approximation, the metallic bonding of aluminum contains tightly binding features.

Accurate and high reciprocal resolution experimental structure factors of aluminum were determined from the synchrotron powder X-ray diffraction data measured at 30 K with  $\sin \theta/\lambda < 2.31 \text{ \AA}^{-1}$ . The structure factors have small deviations from the independent atom model in  $\sin \theta/\lambda < 0.83 \text{ \AA}^{-1}$ . Theoretical structure factors were prepared using density functional theoretical calculations by the full-potential linearized augmented plane wave method. The deviation between experimental and theoretical data was also observed at around  $\sin \theta/\lambda \approx 0.4 \text{ \AA}^{-1}$ . The charge density was determined by an extended Hansen-Coppens multipole model using the experimental and theoretical structure factors. The charge density maxima at the tetrahedral site were observed in both the experimental and theoretical deformation density. The charge-density difference peaks, indicating directional bonding formation, were observed in the difference density between the experiment and theory. The present study reveals the tight binding like character of valence electrons of aluminum. This fact will provide a crucial information for the development of high-performance aluminum alloy.

## Chapter 6 Charge density of molybdenum

### 6.1 Introduction

This section explains the accurate observation of the electron redistribution of  $d$ -electrons in molybdenum. Generally,  $d$ -electrons are localized around atoms even in crystals. The number of  $d$ -electrons contributing to redistribution in the pure molybdenum is an unsolved issue. According to the crystal field theory, in the case of symmetry  $O_h$  in molybdenum with bcc structure, the five  $d$ -electrons are split into three of bonding orbitals and two of antibonding orbitals. The electron redistribution changes this number of electrons. The detection of difference of electron population in the two orbitals from the crystal field theory is a challenging issue to ascertain an achievement of the current accuracy of charge density study by synchrotron powder X-ray diffraction

Electrons in the  $d$ -orbitals of transition metals and their complexes govern their properties and functions. The magnetism of a simple transition metal is caused by the interaction between its  $d$ -electrons. Exotic properties such as superconductivity, multiferroicity, and colossal magnetoresistance were found in transition metal oxides. The properties are closely related to their electronic structure of the  $d$ -electron. The  $d$ -electrons have both an itinerant and localized character in the system. Characterization of the  $d$ -electron in the system is one of the main topics for condensed matter physics and considerable amounts of studies have been carried out to investigate the  $d$ -electron during the past one hundred years [42]. In particular, lots of research has been carried out for  $3d$ -transition metal oxides during the last three decades after the discovery of the high-Tc superconductivity of copper oxide [43]. The heavier  $4d$ - and  $5d$ -elements and their complexes had been ignored until the discovery of the exotic superconductivity of  $\text{Sr}_2\text{RuO}_4$  [44].

The spatial and energetic structures of  $d$ -electrons have been largely investigated both experimentally and theoretically. The distribution of  $d$ -electrons in  $3d$ -transition metals [45, 46, 47, 48, 49, 50] and their complexes [51, 52] have been observed by experimental charge density studies. Spectroscopic studies of  $3d$ -transition metals [53, 54, 55] and their complexes [42, 56, 57] have also been carried out using optical [53, 55, 56, 58], photoemission, [42, 59, 54, 57] and X-ray absorption spectroscopies [60], among others. The spatial and energetic structures of the  $3d$ -electrons have been revealed by the measurements. The energetic structure of the  $4d$ - and  $5d$ -system has also been investigated by the spectroscopies [61]. However, the spatial structure of the  $4d$ - and  $5d$ -system is yet to be revealed experimentally, as the contribution of the  $4d$ - and  $5d$ -electrons to X-ray diffraction is much lower than that of the  $3d$ -system.

We have conducted accurate structure factor measurements for the charge density study from high energy X-ray diffraction (HXRD) of one of the largest third generation synchrotron radiation (SR) facility SPring-8. The highest precision of structure factor using the technique exceeds 0.1%, which is comparable to the extremely accurate Pendellosung fringe method [62] and quantitative convergent beam electron diffraction [6]. The spatial distribution of small amounts of electrons such as the interlayer bonding electron of  $\text{TiS}_2$  [38] and the conductive  $\pi$ -like electron of  $\text{LaB}_6$  [15] have been revealed experimentally by SR-HXRD. It is essential to verify a performance of SR-HXRD for the

visualization of 4*d*- and 5*d*-electrons. Typical materials with 4*d*- and/or 5*d*-electrons are required for this purpose.

Molybdenum is one of the simplest 4*d*-system. The electron configuration of molybdenum is 4*d*<sup>5</sup>5*s*<sup>1</sup>. The electronic structure of molybdenum was investigated by both theoretical and experimental studies [18, 19, 31, 32]. The Fermi surface was investigated using de Haas-van Alphen measurements by several research groups [31, 32]. The band structure was determined by theoretical calculations [18, 19]. The experimental Fermi surface was consistent with that calculated from theory. Zunger et al. [18] demonstrated that the *d*-electrons in the molybdenum comprise bonding orbital  $d_{xy+yz+xz}$  and antibonding orbitals  $d_{z^2}$  and  $d_{x^2-y^2}$ . The electronic structure of molybdenum was investigated by the linear combination of the Gaussian orbitals method (LCGO) [19]. The density of states, Fermi surface, charge form factors, Compton profiles, and optical conductivity were theoretically estimated by this method. The electron density distribution in real space from the experimental results will provide a further understanding of molybdenum. In this study, we completed a charge density study of molybdenum using the SR-HXRD technique [5].

## 6.2 Overview of Experiment

Molybdenum powder with 99.9% purity and 3-5  $\mu\text{m}$  average particle size was used as a sample. The powder was sealed in a 0.2 mm $\phi$  Lindemann glass capillary with argon gas. Synchrotron powder X-ray diffraction data were measured at SPring-8 BL02B2. The Imaging Plate (IP) was used as a detector. The wavelength of the incident X-ray was 37.7 keV calibrated by the lattice constant of the National Institute of Standards and Technology (NIST) CeO<sub>2</sub> standard sample. The temperature of the sample was controlled at 30 K using a He gas flow low-temperature device. Two two-dimensional powder images were measured. One of which was measured by moving detector position to a high scattering angle region in  $2\theta$  to improve the counting statistics and extend the reciprocal resolution.

Molybdenum emits huge amounts of fluorescence and characteristic X-rays when it receives high energy beam. The X-rays increase the background scattering in the powder diffraction data as shown in Figure 6.1(a). Figure 6.1(a) shows the powder profile of the 620 Bragg reflection. The ratio of the standard uncertainty to the Bragg intensity exceeds 1.6%. In this study, the combination of copper and nickel foils attached to the front of the IP was used to reduce the X-ray fluorescence from the molybdenum. Figure 6.1(b) shows the powder profile of the 620 Bragg reflection using metal foils. The ratio of the standard uncertainty to the Bragg intensity improved to 0.92%. The multiple overlaid measurements with the metal foils was effective for improving the precision of the measured structure factors. The ratios of the uncertainties and structure factors of the lowest 16 reflections were better than 0.004.

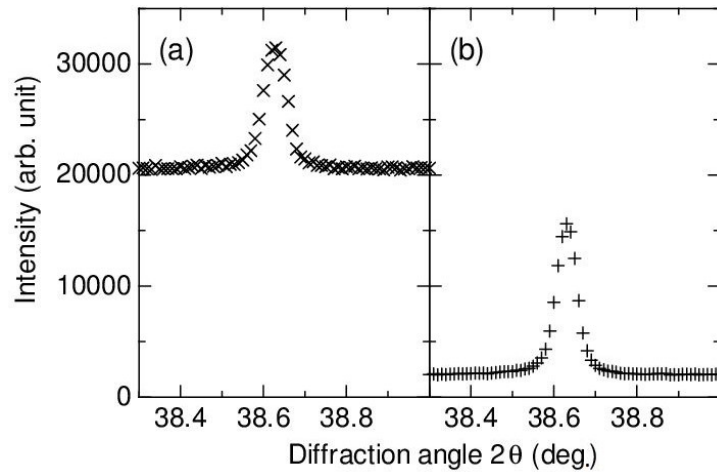


Figure 6.1 Plots of 620 reflection (a) for normal measurement and (b) using copper and nickel foils. The foils reduce fluorescence and characteristic X-ray intensities from molybdenum.

### 6.3 Data analysis by Rietveld refinement

The Rietveld refinements using multiple datasets were carried out using the program Synchrotron Powder (SP) [5]. The reciprocal resolution in the analysis corresponds to  $\sin \theta / \lambda = 2.32 \text{ \AA}^{-1}$ . The observed structure factors were initially extracted from the results of the Rietveld refinements based on the independent atom model (IAM).

### 6.4 Extraction of experimental structure factors with multipole model

The extraction of the observed structure factors was improved by an iterative procedure of multipole refinement and powder diffraction pattern fitting. The electron configuration of molybdenum was  $1s^2 2s^2 2p^6 3s^2 3p^6 3d^{10} 4s^2 4p^6 4d^5 5s^1$ . We set  $4d^5$  valence electron shell. The local axes for the molybdenum atom were parallel to the [100], [010], and [001] directions. The scale factor  $s$ , isotropic thermal displacement,  $u_{\text{iso}}$ , radial expansion / contraction parameters for the spherical valence,  $\kappa$ , aspherical valence,  $\kappa'$ , octapole, O2-, and the hexadecapole parameters, H0, were refined in the analysis. There is a relationship between H0 and H4+, where  $H4+ = 0.74048H0$ . The reliability factors based on the weighted profile  $R_{\text{wp}}$  and the Bragg intensity  $R_i$  of the final pattern fitting were 0.0253 and 0.0133, respectively. The determined lattice constants,  $a$ , and the isotropic atomic displacement parameter,  $u_{\text{iso}}$ , were  $3.142600(1) \text{ \AA}$  and  $0.0661(2) \text{ \AA}^2$ , respectively. The reliability factor based on the observed structure factors of the multipole model  $R_F$  was 0.0056.

### 6.5 Theoretical structure factors

We also prepared theoretical structure factors with the same reciprocal resolution of the observed data using the WIEN2k program [20]. The first principle calculation based on the density functional theory was performed using the full potential-linearized augmented plane wave (FP-LAPW) with the generalized gradient approximation (GGA) in the package. Experimental lattice constants

were used for the calculations. We used 1000 k points with a plane-wave cutoff parameter of  $R^{\text{MT}}K_{\text{max}} = 7.0$ . The theoretical structure factors were calculated by the lapw3 program. The charge density from the theoretical structure factors was also determined by a multipole modelling. The  $R_F$  for the theoretical structure factors was 0.0016.

## 6.6 Comparison of structure factor sets

The present experimental and theoretical structure factors are listed in Table 6.1. The structure factors of the IAM,  $f_{\text{IAM}}$  and LCGO,  $f_{\text{LCGO}}$ , by Jani et al. [19] are also listed in the table. The values are listed as form factors divided by the phase factor. The sixteen lower resolution reflections are also shown in the table. We call the present observed structure factors  $f_{\text{obs}}$ , and the theoretical structure factors by WIEN2k  $f_{\text{WIEN}}$ . The first two reflections of the  $f_{\text{obs}}$ ,  $f_{\text{WIEN}}$ , and  $f_{\text{LCGO}}$  were smaller than that of the  $f_{\text{IAM}}$ .

Figure 6.2 shows plots of the relative ratio of the structure factors to  $f_{\text{IAM}}$  for  $f_{\text{obs}}$ ,  $f_{\text{WIEN}}$ , and  $f_{\text{LCGO}}$ . The deviations from  $f_{\text{IAM}}$  in the lowest two reflections of  $f_{\text{obs}}$ ,  $f_{\text{WIEN}}$  and  $f_{\text{LCGO}}$  are also well recognized in the figure. The two reflections of the  $f_{\text{obs}}$  are numerically identical to those of the  $f_{\text{WIEN}}$  and  $f_{\text{LCGO}}$  from Table 6.1. The reflections with resolutions better than  $0.4 \text{ \AA}^{-1}$  were almost the same as those of  $f_{\text{IAM}}$  within experimental uncertainties. The key features that deviated from the IAM were mainly included in the first two reflections. The maximum deviation of the structure factors from the  $f_{\text{IAM}}$  was less than 2% in the  $f_{\text{obs}}$ ,  $f_{\text{WIEN}}$  and  $f_{\text{LCGO}}$ . The deviations include information on the aspherical distribution of the  $d$ -electrons.

Table 6.1 The lowest 16 structure factors of the present study and LCGO.  $f_{\text{OBS}}$  and  $f_{\text{WIEN}}$  denote the present experimental and theoretical structure factors.  $f_{\text{IAM}}$  was calculated by XD2016.  $f_{\text{LCGO}}$  is the theoretical results [19].

$hkl$	$f_{\text{OBS}}$	$f_{\text{WIEN}}$	$f_{\text{IAM}}$	$f_{\text{LCGO}}$
110	31.31(4)	31.62	31.84	31.59
200	27.11(5)	27.56	27.56	27.49
211	24.71(4)	25.10	24.91	24.98
220	22.73(5)	23.23	23.07	23.11
310	21.19(4)	21.72	21.68	21.62
222	20.24(6)	20.69	20.58	20.58
321	19.20(4)	19.70	19.66	19.60
400	18.35(8)	18.80	18.86	18.70
330	17.55(6)	18.16	18.15	18.05
411	17.56(5)	18.12	18.15	18.01
420	16.92(5)	17.49	17.50	17.37
332	16.35(5)	16.92	16.90	16.81
422	15.84(5)	16.35	16.35	16.23
431	15.24(4)	15.82	15.83	15.70
510	15.24(5)	15.79	15.83	15.67
521	14.12(4)	14.85	14.87	14.73

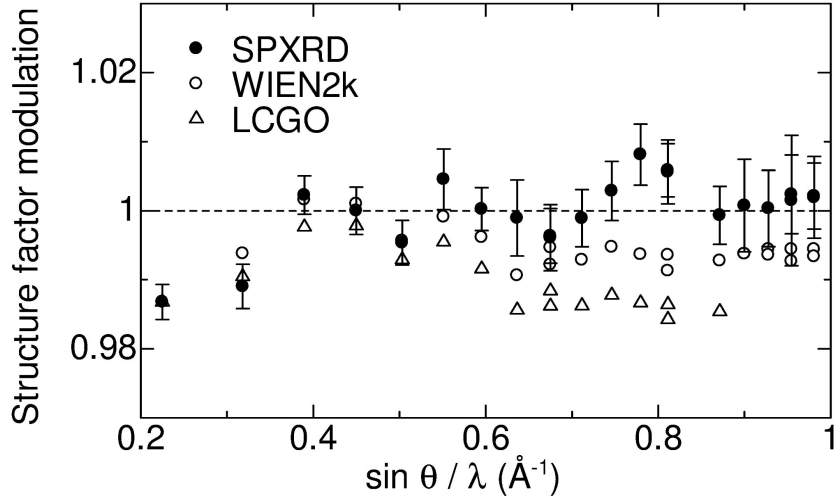


Figure 6.2 Plots of relative ratio of IAM structure factors. Horizontal axis represents reciprocal resolution  $\sin \theta / \lambda$ . Vertical axis represents the relative ratio. Closed circles, open circles, and open triangles are  $f_{\text{OBS}}$ ,  $f_{\text{WIEN}}$ , and  $f_{\text{LCGO}}$ , respectively. Dotted line represents the center of modulations of  $f_{\text{OBS}}$ .

## 6.7 Comparison of valence charge density

Figure 6.3 shows valence charge density maps for the 110 plane from the multipole refinements of the (a) present observed (obs) and (b) theoretical (WIEN2k) structure factors. Contour lines were drawn from 0.0 to 2.0 with a step width of  $0.1 \text{ e}/\text{\AA}^3$ . The centers and corners of the figures present the atomic sites. The map of the same section was reported by [18]. There are four peaks around the atomic sites in Figure 6.3(a) and (b). These peaks were also found in the previous study [18]. The distances between the peaks and the atomic site for obs and WIEN2k were  $0.574$  and  $0.557 \text{ \AA}$ , respectively. The charge densities at the maxima for obs and WIEN2k were  $1.1$  and  $1.3 \text{ e}/\text{\AA}^3$ , respectively. The features of the present observation are well-consistent with the theory. The numerical differences were  $0.017 \text{ \AA}$  in distance and  $0.2 \text{ e}/\text{\AA}^3$  in charge density.

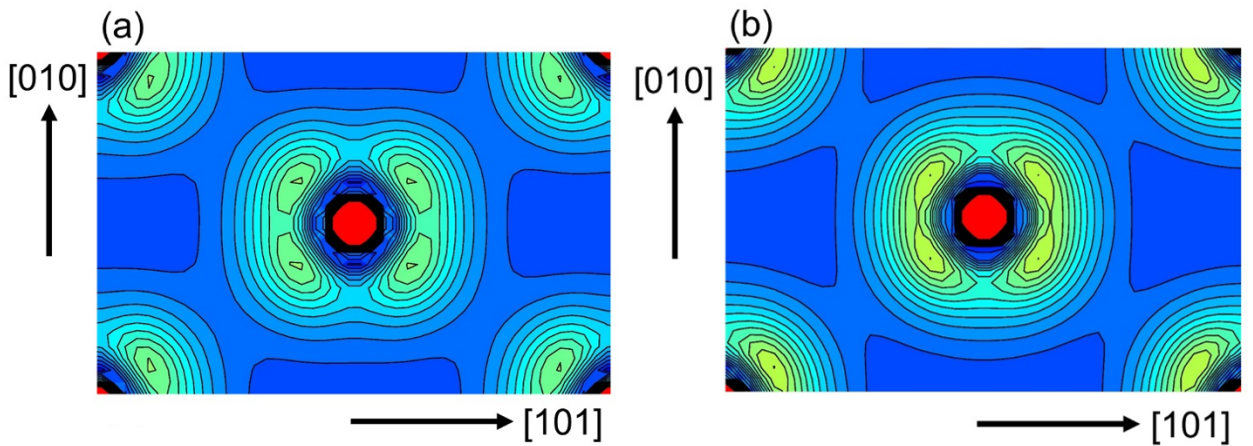


Figure 6.3 Valence charge density maps of (a) obs and (b) WIEN2k for (110) plane. The contour lines were drawn from 0.0 to 2.0 with  $0.1 \text{ e}/\text{\AA}^3$  step width.

## 6.8 Comparison of static deformation densities

Figure 6.4 shows static deformation density maps for 110 plane of (a) obs and (b) WIEN2k. Contour lines were drawn from -0.3 to 0.3 with a step width of  $0.05 \text{ e}/\text{\AA}^3$ . The static deformation density is the difference between the multipole model density and the IAM without effects of thermal smearing. The  $d_{3z^2-r^2}$  shaped negative regions along the up-down direction were found in both figures. In addition, an excess of the charge density was found in the diagonal directions. We have numerically estimated the electron occupancies of the  $4d$ -orbitals of molybdenum. The quantization axes were parallel to the crystal axes as shown in Figure 6.4.

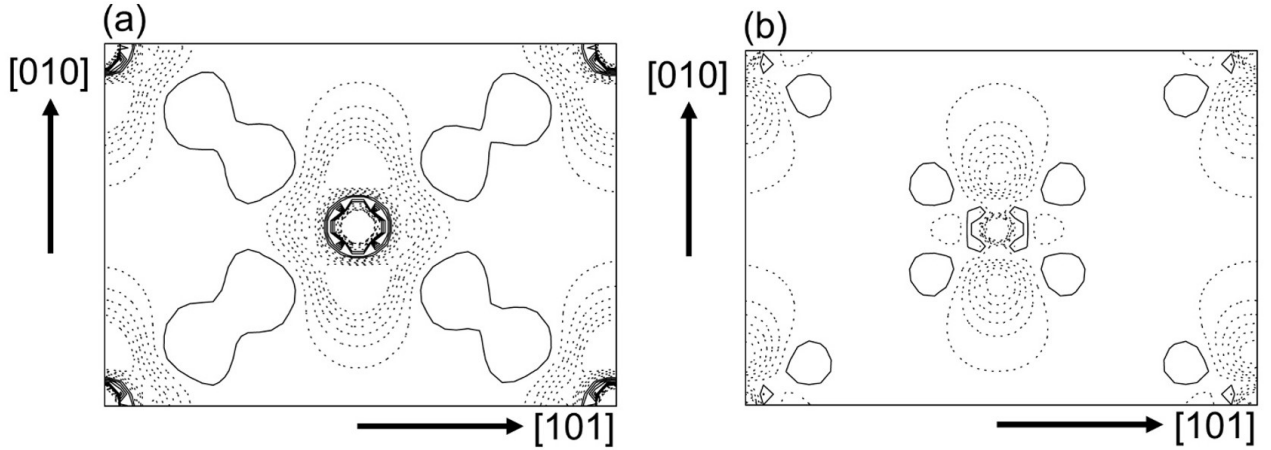


Figure 6.4 Static deformation density maps of (a) obs and (b) WIEN2k for (110) plane. The contour lines were drawn from -0.30 to 0.30 with  $0.05 \text{ e}/\text{\AA}^3$  step width. Solid and dashed lines represented positive and negative density.

## 6.9 Results of $d$ -orbital population analysis

Table 6.2 lists the  $d$ -orbital occupancies of molybdenum of obs and WIEN2k. The  $d$ -electrons of molybdenum can occupy two types of orbitals. One is triply generate  $\Gamma_{25}$ ,  $d_{xy}$  and the other is doubly generate  $\Gamma_{12}$ ,  $d_{xz}$  and  $d_{yz}$ .  $\Gamma_{25}$  is  $d_{xy}$ ,  $d_{yz}$ , and  $d_{zx}$  and  $\Gamma_{12}$  is  $d_{x^2-y^2}$  and  $d_{3z^2-r^2}$ . Occupancies of the two orbitals are also listed in the table. It was found that almost 0.5 electron decreased from the  $\Gamma_{12}$  orbital in the result of the obs. The numbers of deficient and excess electrons of obs was approximately 0.2 electrons different from those of WIEN2k indicating the more aspherical feature of the valence electron of obs.

Table 6.2 The  $d$ -orbital populations for obs and WIEN2k.

orbital	OBS $d_{\text{pop}}$	OBS $d_{\text{occ}}$	WIEN $d_{\text{pop}}$	WIEN $d_{\text{occ}}$
$z^2$	0.76719	15.3%	0.86108	17.2%
$xz$	1.15841	23.1%	1.09582	21.9%
$yz$	1.15841	23.1%	1.09582	21.9%
$x^2-y^2$	0.76634	15.3%	0.85755	17.1%
$xy$	1.15909	23.1%	1.09925	21.9%

## 6.10 Bond characterization by topological analysis of charge density

The topological properties of the charge density for obs and WIEN2k were calculated. The charge densities and Laplacians at the bond critical point (BCP) are listed in Table 6.3. The charge density and Laplacian of obs were  $0.04 \text{ e}/\text{\AA}^3$  higher and  $0.06 \text{ e}/\text{\AA}^5$  lower than those of WIEN2k, respectively. These facts suggest the more covalent bonding character of obs than that of WIEN2k.

Table 6.3 Charge density  $\rho$  and Laplacian  $\nabla^2\rho$  at BCP for obs and WIEN2k.

$\rho_{\text{OBS}}$	$\nabla^2\rho_{\text{OBS}}$	$\rho_{\text{WIEN}}$	$\nabla^2\rho_{\text{WIEN}}$
0.373	3.123	0.326	3.174

## 6.11 Summary

We completed an experimental charge density study of a  $4d$ -transition metal, molybdenum, using state of the art SR-HXRD at SPring-8. Sufficient deviations from the IAM in the structure factors were observed in the first two reflections and the origin of the deviations was revealed by the charge density study by multipole modelling. Solid crystalline molybdenum was formed by the covalent bonding of the  $I'_{25}$   $d$ -orbitals. The bonding contributes to the hardness of the molybdenum solid. The present charge density study supports this picture of solid molybdenum as a hard material. The present study also reveals that molybdenum has more covalent bonding character than the theoretical calculation by WIEN2k with the GGA basis set. We have recently observed a small amount of tight-binding like electron in pure aluminum by SR-HXRD [63]. The chemical bonding was similar to the presently observed covalent bonding character. These studies imply that valence electrons in a pure metal system have a more atomic orbital like character than that expected by the DFT theory.

The less than 0.5 electron deficiency of the orbitals was clearly recognized by the  $d$ -orbital population analysis and the spatial distribution of the  $4d$ -electrons was well recognized in the valence and static deformation density maps in the present study. These facts suggest that the spatial structure of a  $4d$ - and  $5d$ -system can be experimentally revealed by the present SR-HXRD. Recent discovery of novel physical properties of a  $4d$ - and  $5d$ -system such as the superconductivity of  $\text{Sr}_2\text{RuO}_4$  [64] and the metal-insulator transition in  $\text{Cd}_2\text{Os}_2\text{O}_7$  [65]. The present experimental and analytical techniques easily apply to these systems by changing the sample and temperature.

The quality of high-energy quantum beam X-ray and electron beam has been drastically improved throughout the past decade such as with X-ray laser, etc. A state of the art high-energy quantum beam enables us to open a new door in subatomic scale studies. The  $4d$ - and  $5d$ -system with novel physical properties will be a promising target of high-energy quantum beam science.

## Chapter 7 Conclusion

The accurate observation of structure factors of aluminum and molybdenum were successfully observed using synchrotron powder X-ray diffraction. The synchrotron powder X-ray diffraction measurements of aluminum and molybdenum were performed in SPring-8 BL02B2. The resolution  $d$  and reciprocal resolution  $\sin \theta / \lambda$  of the measurement data at 30 K were  $d > 0.22 \text{ \AA}$  and  $\sin \theta / \lambda < 2.31 \text{ \AA}^{-1}$  for aluminum and  $d > 0.22 \text{ \AA}$  and  $\sin \theta / \lambda < 2.32 \text{ \AA}^{-1}$  for molybdenum. The 217 and 193 structure factors were observed for the aluminum and molybdenum, respectively. The errors of less than 0.19% in the diffraction intensity were achieved with the 7 structure factors for aluminum and the 8 for molybdenum. Oxides, internal strain, and stacking fault in the aluminum and molybdenum were not detected in the measurement. The effect to the structure factor of ice generated by the measurement can be neglected. The intensity of the thermal diffuse scattering was negligible at both 30 K data. The effect to the electron density distribution from the electron probability density function of the anharmonic thermal vibration could also be negligible at both 30 K data. The harmonic thermal vibration parameters were accurately determined by the 217 and 193 diffraction peaks for aluminum and molybdenum. The static observed structure factors and its electron density distribution were determined by the estimation of these thermal vibrations.

These observed structure factors by the synchrotron powder X-ray diffraction determined small electron redistributions in aluminum and molybdenum. The modulations of experimental structure factors of aluminum is consistent with the calculated structure factor set using tight-binding approximation. The electron accumulations of the electron redistribution in aluminum were consistent with that of Nakashima et al. [6]. This fact guarantees the validity of the present electron density distribution by the synchrotron powder X-ray diffraction. More detailed electron redistribution than QCBED was successfully observed. The distribution of the charge-density difference between the experimental and theoretical electron redistribution shows residual atomic orbital like electron accumulations. From the results of the structure factor modulations and the residual electron accumulations, the chemical bonding of aluminum contains tightly binding features. The determination of the electron redistribution by the synchrotron powder X-ray diffraction could also be performed in molybdenum. The difference of electron populations in  $d$ -orbitals under  $O_h$  symmetry was successfully observed in the molybdenum. The accurate observed structure factors of molybdenum reproduced the electron redistribution which includes a covalent bonding character than that in the theoretical calculation. The structure factor modulation of molybdenum was observed only in the lowest order two structure factors. The positive electron density from bonding electrons and negative electron density from antibonding electrons were clearly seen in the electron redistribution. The  $d$ -orbital population analysis showed less than 0.5 electron deficiency of the antibonding  $d$ -orbitals.

The observation of accurate structure factor and electron redistribution of metals by the synchrotron powder X-ray diffraction was demonstrated in the aluminum and molybdenum. The accuracy of the low order structure factor in the aluminum and molybdenum was less than 0.3%, exceeding the accuracy of QCBED. The accuracy of the lowest order structure factor was comparable to QCBED. The accuracy of higher order structural factors is one order of magnitude smaller than

QCBED. The synchrotron powder X-ray diffraction technique can be used with a wide range of pure metals and alloys for ease of the sample preparation. Therefore, the demonstration contributes to the increase of results of accurate observed electron density distribution in metals. However, it is necessary to carefully evaluate internal strains and defects of powder samples using 1-D diffraction data. The introductions of the internal strains and defects at the sample preparation can be prevented by the selection of powder samples with the appropriate particle size.

In the state-of-the-art synchrotron powder X-ray diffraction, the perfect crystal with the minimum size of 500 nm in powder is sufficient for the measurement.

The present electron density distribution of aluminum and molybdenum is the most accurate in the world at present. The analysis results of the electron density distribution by Eberhart's method and the improvement of the theoretical wave function in quantum crystallography depend on the accuracy of the experimental electron density distribution. The present electron density distribution pushes these limits due to the accuracy of these electron density distribution. The application of Eberhart's method to the experimental electron density distribution is an important subject in the future. This application contributes to realize an expansion of the electron theory of metals which explains mechanical properties from quantum mechanics. The construction of this new electron theory of metals provides a fundamental understanding of functions of metals and the efficient enhancement of functions of metals. For instance, from an estimation of necessary strength in materials of buildings or vehicles, the combination of elements in an alloy and its composition ratio that satisfies the strength can be determined theoretically.

## References

- [1] N. W. Ashcroft and N. D. Mermin, "Solid State Physics," Saunders College, Philadelphia, 1976.
- [2] S. Ogata, J. Li and S. Yip, "Ideal pure shear strength of aluminum and copper," *Science*, 298, p. 807–811, 2002.
- [3] M. E. Eberhart and T. E. Jones, "Cauchy pressure and the generalized bonding model for nonmagnetic bcc transition metals," *Physical Review B*, 68, p. 184103, 2012.
- [4] M. Eberhart, "A quantum description of the chemical bond," *Philosophical Magazine B*, 81, pp. 721–729, 2001.
- [5] E. Nishibori, E. Sunaoshi, A. Yoshida, S. Aoyagi, K. Kato, M. Takata and M. Sakata, "Accurate structure factors and experimental charge densities from synchrotron X-ray powder diffraction data at SPring-8," *Acta Crystallographica Section A*, 63, pp. 43-52, 2007.
- [6] P. N. H. Nakashima, A. E. Smith, J. Etheridge and B. C. Muddle, "The bonding electron density in aluminum," *Science*, 331, pp. 1583-1586, 2011.
- [7] P. N. H. Nakashima, "Quantitative convergent-beam electron diffraction and quantum crystallography - the metallic bond in aluminium," *Structural Chemistry*, 28, pp. 1319-1332, 2017.
- [8] W. H. Bragg and W. L. Bragg, "The Reflection of X-rays by Crystals," *Proceedings of the Royal Society A*, 88, pp. 428-438, 1913.
- [9] A. W. Hull, "A New Method of X-Ray Crystal Analysis," *Physical Review*, 10, pp. 661-696, 1917.
- [10] A. W. Hull, "X-Ray Crystal Analysis of Thirteen Common Metals," *Physical Review*, 17, pp. 571-588, 1921.
- [11] H. Svendsen, J. Overgaard, R. Busselez, B. Arnaud, P. Rabiller, A. Kurita, E. Nishibori, M. Sakata, M. Takata and B. B. Iversen, "Multipole electron-density modelling of synchrotron powder diffraction data: the case of diamond," *Acta Crystallographica Section A*, 66, pp. 458-469, 2010.
- [12] A. Fischer, D. Tiana, W. Scherer, K. Batke, G. Eickerling, H. Svendsen, N. Binzus and B. B. Iversen, "Experimental and Theoretical Charge Density Studies at Subatomic Resolution," *The Journal of Physical Chemistry A*, 115, p. 13061–13071, 2011.
- [13] H. Kasai and E. Nishibori, "Multiple powder diffraction data for an accurate charge density study using synchrotron radiation x-ray," *Physica Scripta*, 91, p. 043009, 2016.
- [14] N. Wahlberg, N. Bindzus, L. Bjerg, J. Becker, A. -C. Dippel and B. B. Iversen, "Synchrotron powder diffraction of silicon: high-quality structure factors and electron density," *Acta Crystallographica Section A*, 72, pp. 28-35, 2016.
- [15] H. Kasai and E. Nishibori, "Spatial distribution of electrons near the Fermi level in the metallic LaB6 through accurate X-ray charge density study," *Scientific Reports*, 7, p. 41375, 2017.
- [16] N. Wahlberg, N. Bindzus, L. Bjerg, J. Becker, S. Christensen, A. -C. Dippel, M. R. V. Jorgensen and B. B. Iversen, "Powder X-ray Diffraction Electron Density of Cubic Boron Nitride," *The Journal of Physical*

Chemistry C, 119(11), pp. 6164-6173, 2015.

- [17] N. Wahlberg, N. Bindzus, S. Christensen, J. Becker, A. -C. Dippel, M. R. V. Jorgensen and B. B. Iversen, "Low-temperature powder X-ray diffraction measurements in vacuum: analysis of the thermal displacement of copper," *Journal of Applied Crystallography*, 49, pp. 110-119, 2016.
- [18] A. Zunger, G. P. Kerker and M. L. Cohen, "Calculation of the electronic properties of Mo in a first-principles nonlocal-pseudopotential approach," *Physical Review B*, 20, pp. 581-593, 1979.
- [19] A. R. Jani, G. S. Tripathi, N. E. Brener and J. Callaway, "Band structure and related properties of molybdenum," *Physical Review B*, 40, pp. 1593-1602, 1989.
- [20] P. Blaha, K. Schwarz, G. K. H. Madsen, D. Kvasnicka and J. Luitz, "WIEN2k, an Augmented Plane Wave plus Local Orbitals Program for Calculating Crystal Properties," Technische Universitat, Wien, Austria, 2001.
- [21] D. L. McDonald, "Neutron Diffraction Study of the Debye-Waller Factor for Aluminum," *Acta Crystallogr*, 23, p. 185, 1967.
- [22] A. G. Fox and R. M. Fisher, "A summary of low-angle X-ray atomic scattering factors measured by the critical voltage effect in high energy electron diffraction," *Australian Journal of Physics*, 41, pp. 461-468, 1988.
- [23] T. Takama, K. Kobayashi and S. Sato, "Determination of the Atomic Scattering Factors of Aluminium by the Pendellosung-Beat Measurement Using White Radiation," *Transactions of the Japan Institute of Metals*, 23, pp. 153-160, 1982.
- [24] J. J. de Marco, "Single crystal measurement of the atomic scattering factor of aluminum," *Philosophical Magazine*, 15, pp. 483-495, 1967.
- [25] B. W. Batterman, D. R. Chipman and J. J. de Marco, "Absolute measurement of the atomic scattering factors of iron, copper, and aluminum," *Physical Review*, 122, pp. 68-74, 1961.
- [26] P. M. Raccach and V. E. Henrich, "Absolute Experimental X-ray Form Factor of Aluminum," *Physical Review*, 184, pp. 607-613, 1969.
- [27] M. Jarvinen, M. Merisalo and O. Inkinen, "Absolute measurement of the atomic scattering factors of aluminum on powder in transmission," *Physical Review*, 178, pp. 1108-1110, 1969.
- [28] E. Rantavuori and V. -P. Tanninen, "The X-ray atomic scattering factors of aluminum powder at 80 K," *Physica Scripta*, 15, pp. 273-275, 1977.
- [29] H. Bensch, H. Witte and E. Wolfel, "Röntgenographische Bestimmung der Elektronenverteilung in Kristallen IV," *Zeitschrift für Physikalische Chemie*, 4, p. 65, 1955.
- [30] O. Inkinen, A. Pesonen and T. Paakkari, *Annales Academiae Scientiarum Fennicae*, AVI, p. 344, 1970.
- [31] G. B. Brandt and J. A. Rayne, "Low-Field de Haas-van Alphen Studies of Chromium Group Transition Elements," *Physical Review*, 132, pp. 1945-1963, 1963.
- [32] G. Leaver and A. Myers, "De Haas-van Alphen measurements in molybdenum," *Philosophical Magazine*, 19, pp. 465-475, 1969.
- [33] F. C. von der Lage and H. A. Bethe, "A Method for Obtaining Electronic Eigenfunctions and Eigenvalues

- in Solids with An Application to Sodium," *Physical Review*, 71, pp. 612-622, 1947.
- [34] K. Kurki-Suonio, "Symmetry and its implications," *Israel Journal of Chemistry*, 16, pp. 115-123, 1977.
- [35] P. P. Olmer, "Dispersion des Vitesses des Ondes Acoustiques dans l'Aluminium," *Acta Crystallogr*, 1, pp. 57-63, 1948.
- [36] F. H. Herbstein and B. L. Averbach, "Temperature-diffuse scattering for powder pattern from cubic crystals," *Acta Crystallographica*, 8, pp. 843-844, 1955.
- [37] K. Sugimoto, H. Ohsumi, S. Aoyagi, E. Nishibori, C. Moriyoshi, Y. Kuroiwa, H. Sawa and M. Takata, "Extremely high resolution single crystal diffractometry for orbital resolution using high energy synchrotron radiation at SPring-8," *AIP Conference Proceedings*, 1234, pp. 887-890, 2010.
- [38] H. Kasai, K. Tolborg, M. Sist, J. Zhang, V. R. Hathwar, M. O. Filso, S. Cenedese, K. Sugimoto, J. Overgaard, E. Nishibori and B. B. Iversen, "X-ray electron density investigation of chemical bonding in van der Waals materials," *Nature Materials*, 17, pp. 249-252, 2018.
- [39] A. Volkov, P. Macchi, L. J. Farrugia, C. Gatti, P. Mallinson, T. Richter and T. Koritsanszky, "XD2016 - A Computer Program Package for Multipole Refinement, Topological Analysis of Charge Densities and Evaluation of Intermolecular Energies from Experimental and Theoretical Structure Factors," University at Buffalo, State University of New York, University of Milano, University of Glasgow, CNR-ISTM, Middle Tennessee State University, USA, Italy, UK, 2016.
- [40] C. Kittel, "Introduction to Solid State Physics," Wiley Pub., New York, 2004.
- [41] R. A. Tawil, "X-ray form factors and the Compton profile in crystalline aluminum," *Physical Review B*, 11, pp. 4891-4897, 1975.
- [42] M. Imada, A. Fujimori and Y. Tokura, "Metal-insulator transitions," *Review of Modern Physics*, 70, pp. 1039-1263, 1998.
- [43] J. G. Bednorz and K. A. Muller, "Possible highTc superconductivity in the Ba-La-Cu-O system," *Zeitschrift für Physik B Condensed Matter*, 64, pp. 189-193, 1986.
- [44] Y. Maeno, H. Hashimoto, K. Yoshida, S. Nishizaki, T. Fujita, J. G. Bednorz and F. Lichtenberg, "Superconductivity in a layered perovskite without copper," *Nature*, 372, pp. 532-534, 1994.
- [45] W. Jauch and M. Reehuis, "Electron density distribution in paramagnetic chromium: A  $\gamma$ -ray diffraction study," *Physical Review B*, 73, p. 085102, 2006.
- [46] W. Jauch and M. Reehuis, "Electron density distribution in  $\alpha$ -iron: A  $\gamma$ -ray diffraction study," *Physical Review B*, 76, p. 235121, 2007.
- [47] W. Jauch and M. Reehuis, "Electron density distribution in ferromagnetic nickel: A  $\gamma$ -ray diffraction study," *Physical Review B*, 78, p. 235113, 2008.
- [48] W. Jauch and M. Reehuis, "Electron density distribution in hexagonal cobalt: A  $\gamma$ -ray diffraction study," *Physical Review B*, 80, p. 125126, 2009.
- [49] W. Jauch and M. Reehuis, "Electron density distribution in vanadium and niobium from  $\gamma$ -ray diffraction," *Physical Review B*, 83, p. 115102, 2011.
- [50] R. J. Temkin, V. E. Henrich and P. M. Raccach, "Experimental Charge Density of Copper," *Physical*

Review B, 6, pp. 3572-3581, 1972.

- [51] M. S. Schmokel, L. Bjerg, F. K. Larsen, J. Overgaard, S. Cenedese, M. Christensen, G. K. H. Madsen, C. Gatti, E. Nishibori, K. Sugimoto, M. Takata and B. B. Iversen, "Comparative study of X-ray charge-density data on CoSb<sub>3</sub>," *Acta Crystallographica Section A*, 69, pp. 570-582, 2013.
- [52] M. Craven, M. H. Nygaard, J. M. Zadrozny, J. R. Long and J. Overgaard, "Determination of d-Orbital Populations in a Cobalt(II) Single-Molecule Magnet Using Single-Crystal X-ray Diffraction," *Inorganic Chemistry*, 57(12), pp. 6913-6920, 2018.
- [53] H. Ehrenreich and H. R. Philipp, "Optical Properties of Ag and Cu," *Physical Review*, 128, pp. 1622-1629, 1962.
- [54] A. J. Blodgett, Jr. and E. W. Spicer, "Experimental Determination of the Density of States in Nickel," *Physical Review*, 146, pp. 390-402, 1966.
- [55] H. Ehrenreich, H. R. Philipp and D. J. Olechna, "Optical Properties and Fermi Surface of Nickel," *Physical Review*, 131, pp. 2469-2477, 1963.
- [56] M. A. Biondi and J. A. Rayne, "Band Structure of Noble Metal Alloys: Optical Absorption in  $\alpha$ -Brasses at 4.2°K," *Physical Review*, 115, pp. 1522-1530, 1959.
- [57] L. Ley, R. A. Pollak, F. R. McFeely, S. P. Kowalczyk and D. A. Shirley, "Total valence-band densities of states of III-V and II-VI compounds from x-ray photoemission spectroscopy," *Physical Review B*, 9, pp. 600-621, 1974.
- [58] T. Arima, Y. Tokura and J. B. Torrance, "Variation of optical gaps in perovskite-type 3d transition-metal oxides," *Physical Review B*, 48, pp. 17006-17009, 1993.
- [59] T. A. Callcott and A. U. Mac Rae, "Photoemission from Clean and Cesium-Covered Nickel Surfaces," *Physical Review*, 178, pp. 966-978, 1969.
- [60] F. M. F. de Groot, J. C. Fuggle, B. T. Thole and G. A. Sawatzky, "2p x-ray absorption of 3d transition-metal compounds: An atomic multiplet description including the crystal field," *Physical Review B*, 42, pp. 5459-5468, 1990.
- [61] Y. Jeon, J. Chen and M. Croft, "X-ray-absorption studies of the d-orbital occupancies of selected 4d/5d transition metals compounded with group-III/IV ligands," *Physical Review B*, 50, pp. 6555-6563, 1994.
- [62] T. Saka and N. Kato, "Accurate measurement of the Si structure factor by the Pendellösung method," *Acta Crystallographica Section A*, 42, pp. 469-478, 1986.
- [63] T. Sasaki, H. Kasai and E. Nishibori, "Tightly binding valence electron in aluminum observed through X-ray charge density study," *Scientific Reports*, 8, p. 11964, 2018.
- [64] S. Kittaka, H. Taniguchi, S. Yonezawa, H. Yaguchi and Y. Maeno, "Higher-T<sub>c</sub> superconducting phase in Sr<sub>2</sub>RuO<sub>4</sub> induced by uniaxial pressure," *Physical Review B*, 81, p. 180510(R), 2010.
- [65] J. Yamaura, K. Ohgushi, H. Ohsumi, T. Hasegawa, I. Yamauchi, K. Sugimoto, S. Takeshita, A. Tokuda, M. Takata, M. Udagawa, M. Takigawa, H. Harima, T. Arima and Z. Hiroi, "Tetrahedral Magnetic Order and the Metal-Insulator Transition in the Pyrochlore Lattice of Cd<sub>2</sub>Os<sub>2</sub>O<sub>7</sub>," *Physical Review Letters*, 108, p. 247205, 2012.

- [66] F. J. Arlinghaus, "Theoretical X-ray scattering factors based on energy-band structure," *Physical Review*, 153, pp. 743-750, 1967.
- [67] P. Ascarelli and P. M. Raccah, "Simple model potential approach to the X-ray form factor in aluminum," *Physics Letters A*, 31, pp. 549-550, 1970.
- [68] M. Cooper and B. Williams, "Localized orbital wave functions for argon and aluminium - a comparison between theory and experiment," *Philosophical Magazine*, 26, pp. 1441-1446, 1972.
- [69] T. T. Rantana, "Form factors of metallic aluminium from an atom-in-jellium-vacancy model," *Journal of Physics F: Metal Physics*, 17, pp. 877-884, 1987.
- [70] J. P. Walter, C. Y. Fong and M. L. Cohen, "Electronic charge density of aluminum," *Solid State Communications*, 12, pp. 303-307, 1973.
- [71] E. Perrot, "Theoretical form factors of metallic aluminum," *Solid State Communications*, 14, pp. 1041-1045, 1974.
- [72] S. Chakraborty, A. Manna and A. K. Ghosh, "Atomic scattering factors of solid elements," *Physica Status Solidi (b)*, 129, pp. 211-220, 1985.
- [73] P. J. Bunyan and J. A. Nelson, "The valence charge density in aluminum," *Journal of Physics F: Metal Physics*, 7, pp. 2323-2330, 1977.
- [74] J. Hafner, "Electric charge density in simple metals," *Solid State Communications*, 27, pp. 263-268, 1978.
- [75] W. F. Kuhs, "Atomic displacement parameters," *International Tables for Crystallography*, D, pp. 228-242, 2006.

## Acknowledgements

I am deeply grateful to Prof. Nishibori, who is the supervisor of my doctoral course. This research was accomplished by comments and guidance from Prof. Nishibori. My three years of doctoral course consisted of things that can only be experienced under Prof. Nishibori, such as measuring the state-of-the-art powder X-ray diffraction, studying abroad in Denmark, participating in international conferences. Thank you for your guidance for the three years. I also appreciate Dr. Kasai of the assistant professor of the Nishibori laboratory. I got a lot of help at my studying abroad and the attendance at the international conferences. I also got many valuable advice at the unsophisticated scene of my research. I appreciate the precise advices of Professor Moritomo of my chief examiner. Through these advices, the parts I did not understand became clear, and I completed my doctoral thesis. I would like to thank Prof. Kanda who is a sub-chief examiner of my doctoral thesis. Prof. Kanda pointed out numerous points which were insufficient explanation in my doctoral thesis. I also would like to thank Prof. Tokura who is also a sub-chief examiner of my doctoral thesis. Prof. Tokura carefully confirmed the contents of my doctoral thesis and pointed out the necessary description. I would like to offer my special thanks to Prof. Okada who accepted a sudden change of sub-chief examiner at my presentation and got a valuable question. Ozawa-kun, Karatsu-kun, and Nakamura-kun, who completed their master's program last year, were a junior in the grade, but they were a great seniors of Nishihara laboratory. With Ozawa-kun's conversation, I gained a deep knowledge of a new possibilities of McDonald's and the passion to live with cats. The regular research life of Karatsu-kun was my ideal itself, and the comedy duo with Ozawa-kun was a daily tradition of Nishibori laboratory. Nakamura-kun is excellent in balancing things, his tips of the life of Nishibori Laboratory were big help for me. Deguchi-san, who had participated in Nishibori Laboratory at the same time as I, was wonderfully intelligent. She taught me many things which I did not understand in seminars and research. Fujita-kun was a junior with a rare career in the field of physics, and his many experiences were fresh and interesting to me. I am convinced that he will be a great Ph. D student **brightly** illuminating the future of Nishibori Laboratory. Finally, I am grateful to my mother. She has watched over and cheered the irregular path in my life.